Politechnika Wrocławska

FIELD OF SCIENCE: Engineering and technology

DISCIPLINE OF SCIENCE: automation, electronic, electrical engineering, and space technologies

DOCTORAL DISSERTATION

Techniques of generation of the optical frequency comb in the mid-infrared region for laser spectroscopy

Dorota Tomaszewska-Rolla, MSc., Eng.

Supervisor:
dr hab. inż. Grzegorz Soboń, prof. PWr

Assistant supervisor:
dr hab. inż. Karol Krzempek, prof. PWr

Keywords: optical frequency comb, fiber laser amplification, laser spectroscopy, antiresonant hollow-core fiber

WROCŁAW 2024

Acknowledgments

First of all, I would like to thank my supervisor, dr hab. inż. Grzegorz Soboń for guiding me for almost nine years, having unlimited confidence in me, allowing me to make mistakes, and teaching me always to aim high. I also acknowledge dr hab. inż Jarosław Sotor for sharing his ideas and opinions through the years of my research work.

I want to thank people from the Polish optics community that I met along the way, especially those from Laser & Fiber Electronics Group: Olga Szewczyk, Zbigniew Łaszczych, Dorota Stachowiak, Piotr Bojęś, Jakub Bogusławski, Karol Krzempek, and Piotr Jaworski for cooperation during everyday work life, as well as Piotrek Węgrzyn, who is an example of how sometimes you need to travel across the ocean to meet a supportive person from your own country.

I am grateful for meeting Prof. Aleksandra Foltynowicz from the Optical Frequency Comb Spectroscopy Group and for our cooperation during my two short stays in Umeå, Sweden. I also want to thank for many exchanged emails, conversations, and collaborative research, which included sharing knowledge and expertise on spectroscopy.

Chciałabym podziękować również mojej rodzinie, w szczególności Rodzicom, Dziadkom, Siostrom i Szwagrom za całe okazane wsparcie przez lata mojej edukacji i pracy naukowej oraz za niewyczerpane pokłady wiary w moje możliwości.

I thank my close friends, including those I met at my engineering degree, for their support during both good and bad times. Lastly, I express my gratitude to my husband, Jacek, for his patience, understanding, and ongoing encouragement during these intense years.

This work was supported by:

- "Nieliniowa konwersja optycznego grzebienia częstotliwości w zakres spektralny średniej podczerwieni dla zastosowań w spektroskopii", Diamentowy Grant, MEiN, 0066/DIA/2019/48,
- Foundation for Polish Science within the First TEAM program co-financed by the European Union under the European Regional Development Fund (contract no. POIR.04.04.00-00-434D/17-00).

List of acronyms

AC autocorrelator
ARHCF antiresonant hollow-core fiber
ARROW antiresonant reflecting optical waveguiding
ASE amplified spontaneous emission
BS beamsplitter
CPA chirped pulse amplification
CW continuous wave
DAS direct absorption spectroscopy
DFG difference frequency generation
DW dispersive wave
FFT fast Fourier transform
FROG frequency-resolved optical gating
FSR free spectral range
FTS Fourier transform spectrometer
FWHM full width at half maximum
FWM four-wave mixing
GMN gain-managed nonlinear
HCF hollow-core fiber
HNLF highly nonlinear fiber
HWP half-wave plate
ICL intraband cascade laser
IDFG intra-pulse difference frequency generation
ILS instrumental line shape
LMA large mode area
mid-IR mid-infrared
MPC multipass cell
NEA noise equivalent absorption
near-IR near-infrared
OFC optical frequency comb
OPD optical path difference
OPO optical parametric oscillator
OSA optical spectrum analyzer
PAS photoacoustic spectroscopy
PBS polarization beamsplitter
PID proportional-integral-derivative

PPLN periodically poled lithium niobate
PSD power spectral density
QCL quantum cascade laser
QPM quasi-phase matching
RIN relative intensity noise
RMS root-mean-square
SEM scanning electron microscope
SESAM semiconductor saturable absorber mirror
SHG second-harmonic generation
SMF single-mode fiber
SNR signal-to-noise
SSFS soliton self-frequency shift
TL transform-limited
VIPA virtually imaged phased array

Chapter 1.

Introduction

Atoms and molecules are the building blocks of the world. They are everywhere: in the soil, the oceans, all around us, and the air we breathe. However, their very small size makes it challenging to study their properties without sensitive tools. One of the well-established tools is spectroscopy. Spectroscopy studies how matter interacts with an electromagnetic field and provides an effective method for studying molecules in the gas phase. Absorption spectroscopy studies the attenuation of light transmitted through a molecular sample as a function of the light wavelength. Spectroscopy has developed significantly in recent decades, as it allows the detection of trace amounts of gases, such as many greenhouse gases, toxic substances, explosives, or other air pollutants.

Lasers are well-suited sources for spectroscopy and allow highly sensitive and selective absorption measurements due to their high temporal coherence and spectral brightness. It has been exploited in various spectroscopic techniques, with the most developed and well-known based on continuous-wave lasers. Examples are wavelength modulation spectroscopy [1], quartz-enhanced photoacoustic spectroscopy [2], and noise-immune cavity-enhanced optical heterodyne molecular spectroscopy [3]. They mainly use semiconductor lasers: quantum cascade lasers or interband cascade lasers, which provide high-power, coherent, continuous-wave radiation, also in the mid-infrared range (2-20 μm). Continuous-wave lasers provide many advantages for highly sensitive and selective measurements. Unfortunately, a downside of using these sources is that the spectral bandwidth is limited to the tuning range of the laser, which in most cases limits detection to a few absorption lines.

A vast amount of spectroscopic information can be obtained by using broadband sources for absorption spectroscopy, which allows the detection of entire molecular absorption bands simultaneously. The development of the optical frequency comb at the beginning of the 21st century revolutionized the field of laser spectroscopy. It enabled the development of gas detection methods with unprecedented resolution and sensitivity. An optical frequency comb is a laser with an optical spectrum spanning hundreds of nanometres and consisting of equidistant narrow laser modes with known and controllable optical frequencies [4,5]. Mid-infrared is a spectral range that is the most interesting for spectroscopy due to the presence of strong absorption lines of the most noxious molecules and gases [6]. During the last decade, sources in the mid-infrared have been intensively developed. As there is a lack of direct radiation sources that are optical frequency combs in the range between 3 and 10 μm, indirect generation methods are necessary. A standard technique is a nonlinear conversion of near-infrared light to the mid-infrared range through difference frequency or parametric generation.

For nonlinear conversion to be possible, laser pulses with short duration and high power are required. The most common technique for amplifying laser pulses is chirped pulse amplification [7]. While these systems offer a simple design and convenient power scalability, the pulse durations obtained in typical amplifiers are limited due to gain narrowing [8]. The novel method for amplification uses the interaction between gain and nonlinear effects [9]. The gain-managed nonlinear regime offers broad spectra spanning beyond the conventional gain spectra of the active medium, and pulses can be compressed to clean, sub-100-fs pulses. It makes the gain-managed nonlinear amplifier an ideal source of pulses for applications requiring ultrashort pulses and high power [10].

One approach to increasing the signal in absorption spectroscopy measurements is to increase the interaction length between the light and the sample. It can be achieved by placing the sample in a multipass cell, an enhancement cavity, or an antiresonant hollow-core fiber. The first two gas cells are characterized by low robustness, sensitivity to temperature drifts, and a need for a gas sample of large volume. Antiresonant hollow-core fibers [11] with their empty core, which can potentially be filled with the target gas, are an alternative solution. They have not yet been used for broadband spectroscopy with an optical frequency comb in the mid-infrared range. However, their characteristics, like broad transmission windows, low losses, and small volume of gas needed to fill them, position them as notable substitutes for multipass cells.

The dissertation is devoted to the analysis of optical frequency comb sources for laser spectroscopy. The research that was conducted included the investigation of laser pulse amplification in the gain-managed nonlinear regime, a description of difference frequency generation setups and their parameters, an example of multispecies gas detection, and using an antiresonant hollow-core fiber for broadband laser spectroscopy.

The aim of the research was:

- Development of a high-power pump source for nonlinear conversion based on gain-managed nonlinear amplification of a near-infrared optical frequency comb.
- Multispecies detection of methane and ethane using Fourier transform spectroscopy with a difference-frequency-generation-based mid-infrared optical frequency comb.
- Performance comparison between antiresonant-hollow-core-fiber- and multipass-cell-based absorption cells in laser spectroscopy of gases with narrow- and broadband absorption spectra.

The thesis statement was:

- It is possible to generate short laser pulses with high power, whose spectral bandwidth reaches beyond the gain profile of the active medium by using amplification in the gain-managed nonlinear regime.

- Optical frequency combs converted to the mid-infrared region by nonlinear effects enable absorption spectroscopy of narrow- and broadband absorption lines using antiresonant-hollow-core-fiber-based absorption cell, with parameters comparable to the ones obtained with a multipass cell of similar length.

The dissertation consists of 6 Chapters, including an Introduction and Conclusions. Chapters 2 and 3 give the theoretical background, while Chapters 4 and 5 describe the experimental work carried out by the Author.

Chapter 2 is a theoretical introduction to optical frequency combs. First, it includes the principle of operation for the mode-locking in lasers. Then, it explains various methods of obtaining optical frequency combs, from basic pulse operation and stabilization through self-mode-locking in semiconductor lasers to microresonators and electro-optic combs. Also, the amplification of laser pulses is described, focusing on the new regime called gain-managed nonlinear amplification. It can provide high-peak-power pulses with broad optical spectra and nearly transform-limited pulses after compression. In the end, the generation of optical frequency comb in the mid-infrared spectral region is addressed, emphasizing the advantages of nonlinear conversion, like difference frequency generation.

Chapter 3 overviews direct laser absorption spectroscopy with optical frequency combs. It starts with a theoretical background of absorption spectroscopy and points out the advantages of using frequency combs as light sources. Next, the methods for enhancing the absorption signal are presented, concentrating on techniques for increasing the light-gas interaction length. The methods described comprise multipass cells, optical cavities, and antiresonant hollow-core fibers with their principles of operation, features, strengths, and weaknesses. At last, different spectrometers are described, particularly the Fourier transform spectrometer, as it is suitable for spectroscopy measurements with an optical frequency comb. The Chapter also presents the design of the Fourier transform spectrometer used for experiments presented in this dissertation.

Chapter 4 presents the analysis of gain-managed nonlinear amplification in an ytterbium-doped fiber laser. The experimental results show the influence of different wavelengths of the pump laser and repetition rates of the seed source on the parameters of amplified pulses. The research was conducted in collaboration with a group from the Royal Institute of Technology in Sweden, which was responsible for theoretical and numerical analysis. The conclusions of this study are presented in this Chapter, together with the measured parameters of the pulses like spectra, autocorrelation functions, pulse duration, noise properties, and output powers. The constructed gain-managed nonlinear amplifier was used to investigate the conversion of the optical frequency comb via difference frequency generation to the mid-infrared spectral region.

Chapter 5 concentrates on the examples of laser spectroscopy using optical frequency combs converted to the mid-infrared range. Initially, the design of the difference frequency generation source based on an erbium-doped fiber laser is described. Then, two experiments are presented, showing the advantages of using an optical frequency comb, which is multispecies detection, and the possibility of measuring both broad- and narrowband absorption lines. Both experiments consist of spectroscopic measurements and fits based on databases, which were conducted in collaboration with prof. Aleksandra Foltynowicz from

Umeå University in Sweden. The second experiment involved a comparison between the usage of antiresonant hollow-core fiber and multipass cell to increase the interaction length of light and gas. It was carried out with Piotr Jaworski and Karol Krzempek from Wrocław University of Science and Technology. The results shown in this Chapter confirm that antiresonant hollow-core fibers are reliable substitutes for multipass cells.

Chapter 2.

Optical frequency combs in the mid-infrared region

2.1. Introduction

The history of optical frequency combs (OFCs) starts with the first pulsed laser, which dates back to 1964 [12,13]. Nevertheless, it was not until the 1990s that several techniques were suggested to detect and stabilize the frequency domain parameters of a pulsed laser [4,14,15]. It led to the connection between the microwave and the optical domain of the frequency comb. Since then, frequency combs have revolutionized not only precision time and frequency metrology but also numerous research fields. They serve as a way to directly count the optical cycles [16,17], compare different optical standards [16,18], and transfer the frequency through a fiber network [19,20]. Other examples of applications can be found in precision spectroscopy [21], optical signal processing [22], generating attosecond laser pulses [23], and calibration of astronomical spectrographs [24]. John L. Hall [25] and Theodor W. Hänsch [26], the pioneers in the development of OFCs, were awarded a Nobel Prize in Physics in 2005 "*for their contributions to the development of laser-based precision spectroscopy, including the optical frequency comb technique.*"

The first realizations of the OFC were carried out with the titanium-sapphire laser, which was built using free-space optics. Despite the use of free-space components and low durability, these comb sources are still in use in a multitude of applications. As time passed, Ti:sapphire lasers have started to be replaced by fiber-based frequency combs due to their technical simplicity and robustness. Most commonly used active fibers in mode-locked lasers are doped with rare-earth ions like ytterbium, erbium, holmium, or thulium, which emit laser radiation in the near-infrared (near-IR) spectral range.

The spectrum of the OFC consists of a series of narrow, equidistant laser modes, which provide broad spectral bandwidth and high spectral resolution. Those parameters led to using OFCs as light sources in spectroscopy. The strongest absorption lines, due to the rovibrational transitions of most of the molecules, reside in the mid-infrared (mid-IR) range [6]. As the frequency combs generated by the mode-locked lasers are limited to the visible and near-IR ranges, to fully exploit the benefits of OFC, there is a need to transfer the laser radiation towards longer wavelengths. The most common approach is to use nonlinear conversion methods like optical parametric oscillator [27] or difference frequency generation [28].

In this Chapter, OFCs are discussed. First, the operational principles and equations behind the mode-locked laser are presented. Then, different methods of generating OFCs and their

properties and stabilization techniques are reviewed. After that, the new amplification method is introduced, allowing us to obtain spectra broader than the gain profile of the active medium. Finally, various approaches to generating frequency combs in mid-IR are addressed, especially difference frequency generation.

2.2. Mode-locked lasers

Mode-locking is a crucial technique for generating pico- and femtosecond pulses and obtaining OFCs. The term resulted from an interpretation in the frequency domain: in the mode-locked state, a large number of longitudinal modes oscillate with a fixed relative phase. In the laser cavity, every longitudinal mode has to meet the conditions required to generate a standing wave. The free spectral range (FSR) of such cavity, or in other words, the axial mode spacing for a linear type resonator, is described as [29]:

$$FSR = \frac{c}{2L}\,, \tag{2.1}$$

where c = 299 792 458 m/s is the speed of light in a vacuum, and L is the resonator's length. The refractive index will affect the latter in the case of a resonator filled with a dispersive medium. Factor 2 is removed for a ring resonator since there is no double pass through it. The following expression describes the electric field in the cavity:

$$E(t) = \sum_{m=-M}^{M} E_m e^{(i\phi_m - i\omega_m t)}\,, \tag{2.2}$$

where E_m, Φ_m, and ω_m denote the amplitude, phase, and frequency of an m^{th} cavity mode, while the total number of resonator modes is $2M+1$. Constructive interference between longitudinal modes that are phased-synchronized leads to the formation of a train of laser pulses at the output of the resonator, as illustrated in Fig. 2.1. The random phase relations between the individual modes result in continuous-mode laser operation with time-fluctuating average power. The mode-locking is formed by fixing the relationship of the phase difference between the individual modes to a constant Φ, whose value is $\Phi = \Phi_m - \Phi_{m-1}$. The frequency of the m^{th} longitudinal mode of the laser is $\omega_m = \omega_0 + 2m\pi \cdot \Delta\nu$. The total light intensity in the laser cavity with a structured phase relation between the longitudinal modes (with the same amplitude equal E_0) is then described by the relation [29]:

$$|E(t)|^2 = \frac{sin^2\left[(2M+1)\pi \cdot \mathrm{FSR} \cdot t + \frac{\phi}{2}\right]}{sin^2\left[\pi \cdot \Delta\nu \cdot t + \frac{\phi}{2}\right]} \cdot E_0^2\,, \tag{2.3}$$

which is periodic with a period $\tau = (\Delta\nu)^{-1}$, corresponding to the pulse propagation time through the resonator. The repetition rate f_{rep} of the generated pulses corresponds to the mode spacing $\Delta\nu$ (meaning the inverse of τ). The shortest duration τ_{min} of a single pulse depends on the number of synchronized longitudinal modes spaced by the frequency $\Delta\nu$ and is determined from:

$$\tau_{min} = \frac{K}{(2M+1)\cdot \mathrm{FSR}}, \tag{2.4}$$

where K is called the pulse shape factor and depends on the dispersion regime of the generated pulses. For the Gaussian profile pulse, the factor equals 0.441, and for the squared hyperbolic secant, it is 0.315. From Eq. (2.3), it can also be noted that the peak intensity, defined as the square value of the maximal electric field, depends quadratically on the number of longitudinal modes N excited in the cavity.

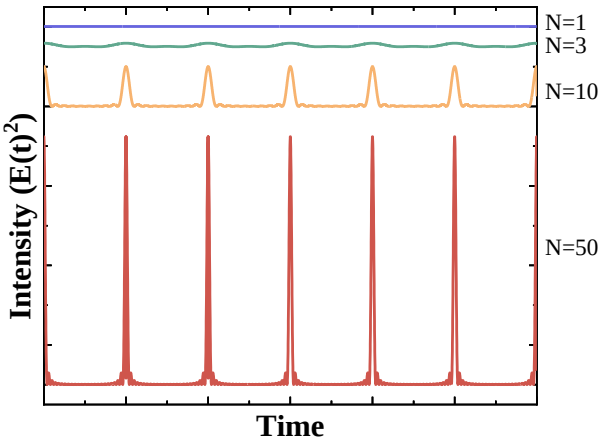

Fig. 2.1. Effect of the number of synchronized longitudinal modes N of the cavity on laser output characteristics. The more modes are mode-locked, the higher the intensity and the shorter the pulse duration.

Therefore, as the number of synchronized modes increases, the minimum duration of propagating pulses in the cavity decreases. Theoretically, synchronizing an infinite number of longitudinal modes leads to generating a sequence of Dirac deltas $\delta(t)$. From the relationship between the signal in the time domain and its counterpart in the frequency domain of the Fourier transform, it follows that the pulse duration and its spectral width are inversely proportional to each other. It makes it necessary for the source of the ultrashort pulses to have a sufficiently broad optical spectrum. In a real system, the limitation is primarily due to the gain bandwidth of the active medium. From a practical point of view, this means that either nonlinear spectral broadening is required or an active medium with a broad emission bandwidth must be used, for example, optical fibers doped with rare earth ions (such as ytterbium, erbium, thulium, or holmium).

In order to force the pulsed operation of the laser, an amplitude modulator must be introduced into its cavity to modify the losses periodically. Such an element should favor high intensity, repeatedly increasing the transmission as the intensity builds up in the cavity. The methods can be divided into active and passive depending on the technique in which the longitudinal modes are forced into synchronization. In the case of active mode-locking, an externally driven element, such as an acousto-optic, electro-optic, or another type of modulator, is used to modulate the losses in the laser cavity. The frequency of the modulating signal is usually equal to or an integer multiple of the pulse circulation time in the laser cavity. This way, pulses of tens of picoseconds in duration can be generated. The advantage of active mode-locking is that the repetition rate of the pulses can be electrically controlled using harmonic mode-locking. It allows the repetition rate to be increased up to several tens

of gigahertzs [30,31]. A variation is a rational harmonic mode-locking where the modulation frequency is a round-trip frequency multiplied by the ratio of two integers [32,33].

Much shorter pulses, with durations as short as single femtoseconds, can be obtained using passive mode-locking, where a passive element called a saturable absorber is introduced in place of the active amplitude modulator. In saturable absorbers, the incident light changes the transmittance of the absorber, whereas, in active methods, the modulator changes the transmittance due to an external electrical field. Saturable absorbers can be subdivided into elements that are constructed from a material that exhibits saturable absorption and that use nonlinear optics that mimic saturable absorption, so-called artificial saturable absorbers. The phenomenon of saturable absorption can be observed in nanomaterials (one- and two-dimensional) such as graphene [34,35] and carbon nanotubes [36], semiconductor structures based on quantum wells (SESAM – semiconductor saturable absorber mirror) [37], or topological insulators (e.g., bismuth telluride, antimony telluride) [38,39].

2.3. Optical frequency comb

The output of a mode-locked laser can be considered in two domains: time and frequency, as shown in Fig. 2.2. In the time domain, the electric field consists of a series of repetitive coherent pulses. The repetition period of the pulses, τ_{rep}, is determined by the optical path length of the laser cavity. For fiber lasers, it is usually in the few nanoseconds range (corresponding to a resonator length of a few meters), while the duration of the pulse, τ, is generally of the order of tens to hundreds of femtoseconds.

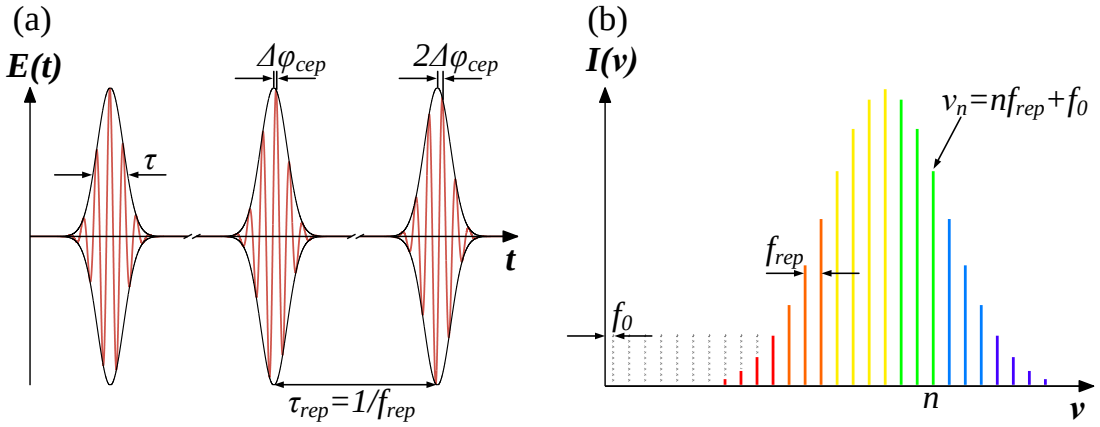

Fig. 2.2. (a) Time and (b) frequency representation of an optical frequency comb. In the time domain, OFC produces pulses with the duration of τ, which are τ_{rep} apart from each other. In the frequency domain, OFC generates comb lines, which are f_{rep} apart from each other. Each comb line has an optical frequency ν_n described by the multiple of f_{rep} and f_0.

During pulse propagation in any dispersive medium, the relative position of the envelope and the carrier wave are shifted, caused by the difference between phase and group velocity. Between every consecutive pulse, the carrier wave is phase-shifted relative to the pulse envelope by the constant value $\Delta\varphi_{cep}$. In the frequency domain, a mode-locked laser produces a broad spectrum consisting of thousands of narrow comb lines, evenly spaced by the repetition rate $f_{rep} = 1 / \tau_{rep}$. Each optical frequency ν_n of the mode-locked laser can be written as:

$$\nu_n = nf_{rep} + f_0 \ , \tag{2.5}$$

where n is an integer mode number, which in general is in the range of 10^5-10^6 for a femtosecond mode-locked laser, and f_0 (also labeled as f_{ceo}) is the so-called carrier-envelope offset frequency. The offset originates from the carrier-envelope phase shift $\Delta\varphi_{cep}$ and moves the entire comb grid from an exact multiple of the repetition rate by the f_0. It can be defined by:

$$f_0 = \frac{\Delta\varphi_{cep}}{2\pi} f_{rep} \ . \tag{2.6}$$

Therefore, the frequencies of the optical frequency comb are correlated with each other through the relation: $0 \leq f_0 \leq f_{rep}$.

OFCs, as we know them today, are considered to be just mode-locked lasers with two known and stabilized frequencies: f_{rep} and f_0. The width of each comb mode (also known as comb line or comb tooth) depends on the stability of these two radio frequencies. The noise at low frequency induces a slow drift of the comb lines, while at high frequency, it influences the width of the modes. To achieve precise control of the repetition rate and offset frequency of the comb, they should be continuously measured in the system. Measuring the f_{rep} is relatively uncomplicated and can be performed using a single high-bandwidth photodiode with hundreds of megahertz to a few gigahertz electrical bandwidth.

The measurement of the f_0 is more complex since there is no direct way to acquire it. The method widely used to this day for measuring the offset frequency is the so-called *f-2f* beating [15] shown in Fig. 2.3. In this technique, a frequency comb spectrum must span an octave in the frequency domain, which is usually implemented by broadening the spectrum in a highly nonlinear medium. Then, the frequency of the n^{th} comb mode in the low-frequency side is doubled, usually by the second-harmonic generation (SHG) process, which leads to generating the frequency around the $2n^{th}$ comb mode. The beating of these two groups of modes can be detected in the electrical field and will fulfill the equation:

$$2\nu_n - \nu_{2n} = 2\left(nf_{rep} + f_0\right) - \left(2nf_{rep} + f_0\right) = f_0 \ . \tag{2.7}$$

This method is often called "self-referencing" as it does not need any additional laser to measure carrier-envelope offset frequency, but it is based on the beating between two different parts of the same comb.

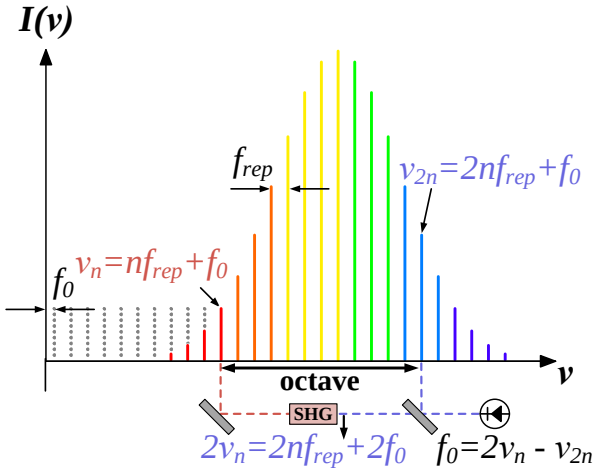

Fig. 2.3. Detection of the offset frequency by *f-2f* beating. The optical frequency ν_n is doubled in a second-harmonic generation (SHG) to obtain $2\nu_n$. It is then mixed with ν_{2n} to get the beatnote between them, which is f_0.

Methods of controlling the repetition rate of the fiber laser are based on changing the length of the laser cavity, for example, using a piezoelectric transducer [40] to stretch the fiber, delay-line to extend the optical path or free-space electro-optic modulator to change the refraction index of a part of the laser, which influences the optical path [41]. An important parameter influencing the repetition rate of the fiber laser is also the temperature. Stabilization of the temperature provides the opportunity to roughly fix the repetition rate at the desired value, which is later complemented by previously mentioned methods with less impact on the effective optical length of the laser cavity.

One of the most commonly used methods to control the carrier-envelope offset frequency is to modulate the pump laser current [42]. Changing the current alters the excitation level in the active fiber, affecting the gain level and, thus, the refractive index and, consequently, the dispersion. Another technique is based on directly changing the dispersion of the laser cavity using a dispersive component (e.g., prisms [4] or wedge plates [43]).

The OFC can be stabilized in the radio-frequency or optical domain. In the radio-frequency locking scheme, both frequencies f_{rep} and f_0 are locked to a stabilized radio frequency, originating from, for example, a rubidium-based clock. The repetition rate is measured with a photodetector and band-pass filtered. The offset frequency is measured using the *f-2f* interferometer. Then, both frequencies are mixed with reference signals generated by the direct digital synthesizers (DDSs) from the reference frequency. The generated beat notes are low-pass filtered to produce error signals, which are then sent to proportional-integral-derivative (PID) controllers to produce correction signals for corresponding actuators. For example, one loop affects the cavity length, and the other affects the pump laser current. In this method, f_0 and f_{rep} are as stable as the reference frequency, but the comb lines still have quite a large linewidth. The schematic of radio-frequency locking is presented in Fig. 2.4.

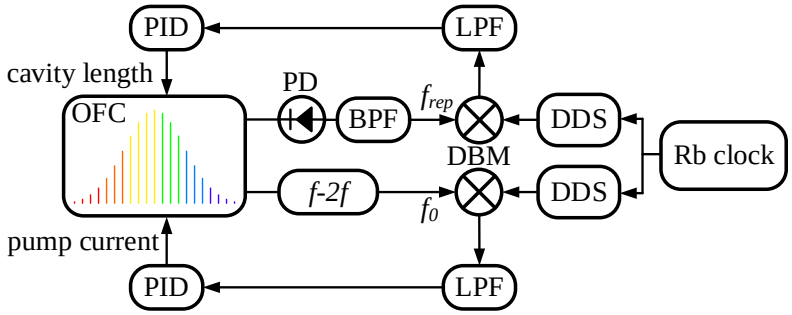

Fig. 2.4. Setup for stabilizing an optical frequency comb (OFC) to a radio-frequency source. f_{rep} is controlled by the cavity length and f_0 by the pump laser current. *f-2f*, *f-2f* interferometer; PD, photodetector; BPF, band-pass filter; DBM, double balanced mixer; DDS, direct digital synthesizer; LPF, low-pass filter; PID, proportional-integral-derivative controller.

Narrower comb modes can be achieved when locking to a stable continuous-wave (CW) laser in the optical domain. Fig. 2.5 shows a schematic for locking the f_{rep} to a CW laser. First, the comb spectrum is coupled out into free space to be dispersed using a grating and then interfered with a CW laser. A photodetector is used to measure the frequency difference, and the band-passed signal is mixed with a stable frequency generated by a DDS reference to the Rb-based clock. The beat note is low-pass filtered and used as an error signal for the PID controller. The correction signal is then sent to the f_{rep} actuator, for example, affecting cavity length, and f_0 is stabilized in the radio-frequency domain (not shown in a figure).

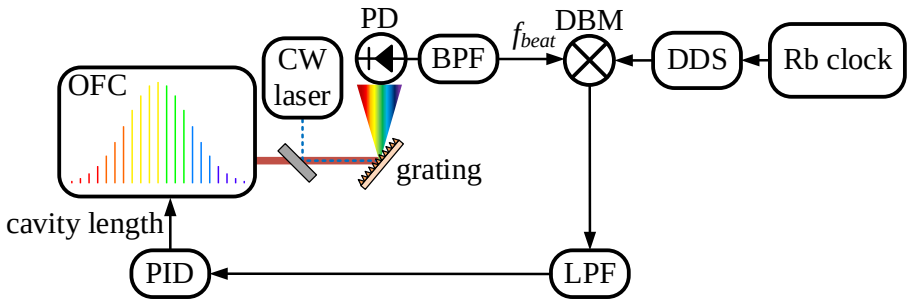

Fig. 2.5. Setup for stabilizing the repetition rate of an OFC to a CW laser. f_{rep} is controlled by the cavity length. PD, photodetector; BPF, band-pass filter; DBM, double balanced mixer; DDS, direct digital synthesizer; LPF, low-pass filter; PID, proportional-integral-derivative controller.

2.3.1. Different methods of generating an optical frequency comb

OFC generation depends on the specific needs of the application. Most work centers around the mode-locked solid-state- [44] and fiber-based laser [45]. Solid-state mode-locked lasers offer lower phase noise. However, they have large size and weight, which, together with high susceptibility to environmental variations, makes them suitable mainly for laboratory use. On the other hand, diode-pumped fiber lasers, built with off-the-shelf all-fiber components and emitting light in the telecommunication band around 1550 nm, provide compact, robust, and energy-efficient systems with easier heat dissipation and cooling. It makes them the most commonly used and the only commercialized OFCs to date. The development of high-pulse energy OFCs enabled the use of nonlinear processes to broaden and convert the spectrum. High-brightness short-pulsed laser sources are the only means for broad spectroscopic coverage at some wavelengths, particularly in the mid-IR to the terahertz region [46], as well as from the ultraviolet (UV) to the extreme UV [47].

Another type of frequency comb based on mode-locked technology is semiconductor lasers. They offer compact size, compatibility with chip-scale systems, mass-production capability, and, most importantly, high repetition frequency (> 1 GHz). Both passive and active methods can be used to generate a train of pulses in the semiconductor material, although a saturable absorber in a passive mode-locking scheme increases the intracavity losses, significantly reducing power and efficiency for semiconductor lasers. Therefore, the phenomenon of self-mode-locking is used, mainly in quantum cascade lasers (QCLs) and intraband cascade lasers (ICLs), where the ultrashort excited-state lifetime [48] makes passive mode-locking impossible. ICLs and QCLs are based on sandwiched quantum-well heterostructures that resemble an engineered bandgap material and emit light throughout the mid-IR and THz region. The difference between them is that in ICLs, photons are generated with interband transitions, and in QCLs, it happens in intersubband transitions. As a result of photon generation, a strong effect of four-wave mixing (FWM) within the active medium phase locks the modes of the lasers [49]. It is important to note that they do not produce optical pulses. The laser modes maintain a stable phase relationship but might not share a uniform phase throughout the spectrum. It could lead to difficulties in nonlinear broadening, stability, and regularity in mode spacing. Despite this, QCL and ICL combs can exhibit superior temporal coherence over comb lines [50] and are the only OFCs with direct electrical pumping.

In recent years, with the development of chip-scale systems, other types of combs have been researched with principles of operation different from mode-locking. The first example is supercontinuum generation in waveguides, where the pump used is usually a train of ultrashort pulses from a mode-locked laser source that propagates through a nonlinear waveguide and undergoes spectral broadening [51]. The obtained spectra depend on the input pulse time duration, dispersive properties of the waveguide, and its refractive index [52]. To obtain high coherence of the generated spectrum, it is crucial to work in weak normal dispersion [53], while anomalous dispersion offers a broader OFC span [54]. As supercontinuum generation is already a well-known effect in optical fibers, waveguides offer more versatility in terms of optical shaping, as they are produced by lithographic methods, but they experience considerably higher insertion and propagation losses.

Different examples of chip-scale OFCs are so-called microcombs, microresonators, or Kerr combs. They come in different shapes and geometries (like spherical, cylindrical, toroidal, and ring) and can be composed of varied materials, but they all possess high-quality factor (high-Q). An essential property of Kerr combs is large mode spacing, typically in the range of 10 GHz to 1 THz. Microcombs work as built-up cavities that can efficiently store and enhance the optical field in the FWM process. The process is depicted in Fig. 2.6. When the microresonator parameters: nonlinearity, dispersion, loss, and gain are balanced, and the external CW pump is used by appropriately tuning the frequency and/or the amplitude of the pump field, it is possible to excite dissipative Kerr solitons [55]. The formation of the self-sustaining wave packets, in which all frequency comb lines are phase-locked with each other, is described by the Lugiato-Lefever equation [56,57]. Microcombs allow for the generation of frequency combs on a chip scale, but they do not always produce optical pulses.

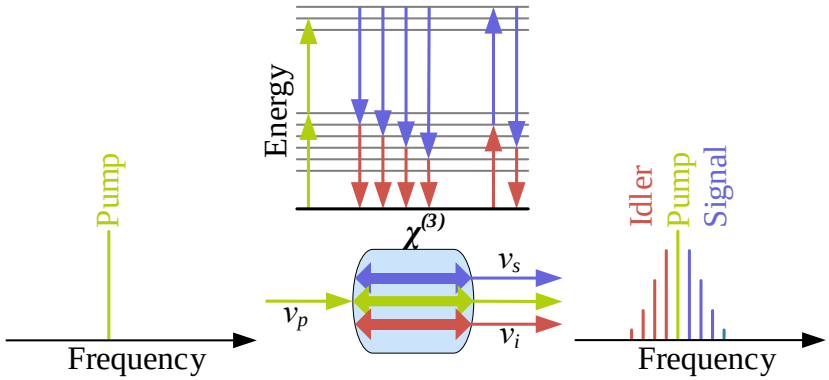

Fig. 2.6. The scheme for generations of a Kerr comb. A resonator made of a material with $\chi^{(3)}$ nonlinearity is pumped by a CW laser. Signal and idler sidebands are generated in the resonator modes next to the pump mode through a degenerate four-wave mixing process.

One more method of generating a frequency comb is via electro-optic modulation. In this process, a CW pump laser is modulated by a single-frequency sinusoidal microwave signal, which generates sidebands on both sides of the pump frequency. Then, a cascade of sum and difference frequency generation happens, resulting in a frequency comb centered around the CW laser frequency and repetition rate given by the microwave modulation frequency. This type of OFC is called an electro-optic (E-O) frequency comb. They can work for pump wavelengths from 780 nm to 2 μm and offer wide-band and agile tuning of the mode spacing.

E-O combs used to be utilized in precision optical metrology, but there was a small improvement in their field. Over the past few years, these sources have been revisited in the context of arbitrary optical waveform generation [22] and microwave photonics [58]. A recent breakthrough presented an octave-spanning E-O comb, which led to the locking of f_{rep} and f_0 for full stabilization [59]. This has overcome the long-standing problem of electro-optic combs, namely high phase noise and low stability compared to mode-locked fiber lasers.

The diversity of requirements for OFCs in various types of applications, from fundamental science, medicine, and metrology to industry, leaves room for different types of combs. The parameters, such as the size of the setup and its complexity, pump type, repetition rate, comb bandwidth and linewidth, operation wavelength, stability, noise properties, output power, and many more, will determine the corresponding type of OFC. In the longer term, for systems of high complexity, multiple types of comb sources will co-exist and serve different purposes.

2.4. Amplification of laser pulses

Fiber lasers with passive mode-locking generate pulses with durations in the order of femtoseconds, however, with relatively low average output power, usually not exceeding a few or several milliwatts. This power level is clearly insufficient for many practical applications, such as nonlinear conversion. It is, therefore, necessary to appropriately amplify the radiation from such lasers. Amplification of femtosecond pulses poses a significant scientific problem as well as a design challenge. A method widely used in the industry is a master oscillator power amplifier (MOPA) configuration. However, it is only capable of amplifying CW lasers or pulsed ones but with a pulse duration in the order of single nanoseconds or hundreds of picoseconds.

When amplifying ultra-short pulses, the peak power of such a short pulse very quickly exceeds the threshold for the occurrence of nonlinear phenomena in the amplifying medium, which are a consequence of the optical Kerr effect, for example, self-phase modulation (SPM). These phenomena lead to deformations of the pulse shape, unwanted broadening, distortion of the optical spectrum, and sometimes even damage to the optical fiber as a result of the self-focusing effect of the beam. The solution to avoid nonlinear phenomena in the active fiber is to reduce the intensity of the pulse propagating through the amplifier by stretching the pulses in time, then amplifying it and recompressing at the end. It forms the basis of the chirped pulse amplification (CPA) technique, illustrated in Fig. 2.7.

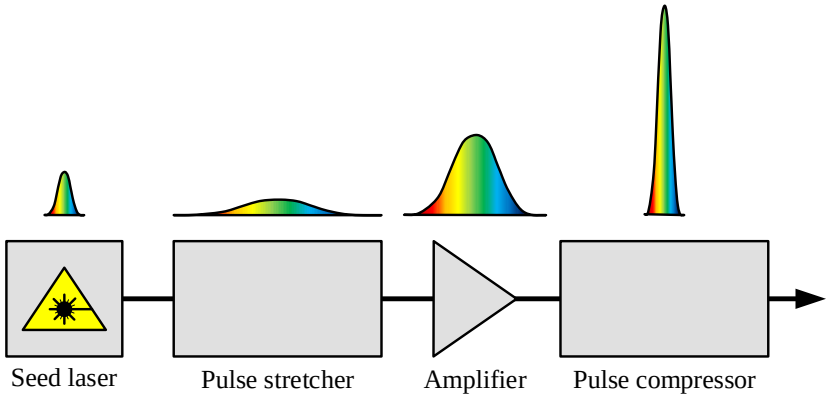

Fig. 2.7. The idea of the chirped pulse amplification technique. The pulses from the seed laser are first stretched, then amplified and compressed at the end.

All techniques that are used for pulse stretching and compressing in CPA systems are based on optical setups with dispersion. There are three main types of dispersion in optics: material dispersion, dispersion from interference, and geometric (angular) dispersion. Material dispersion results from the properties of specific optical materials in which the refractive index varies with the wavelength of light. The second is based on the use of periodic interference structures to delay some components of light relative to others. The angular dispersion results from the phenomenon of diffraction, which allows for achieving different effective optical paths for different spectral components.

The inventors of the CPA technique are Donna Strickland and Gérard Mourou, who, in 1985, demonstrated the world's first setup that allowed pulse amplification from an Nd:YAG laser and its compression to 1.5 ps [7]. The development of the CPA technique certainly revolutionized laser technology, as it has allowed the construction of pulsed systems with gigantic output powers. Since 1985, there has been a vast number of scientific publications whose authors have been trying to obtain increasingly shorter pulses with the highest possible energy. Today, almost all commercially available high-power femtosecond lasers are built according to the concept of CPA, and it is also used in the world's most powerful laser systems to generate subpicosecond pulses with peak powers of the order of petawatts and energies of hundreds of joules.

Although CPA systems have simple layouts and offer favorable power scalability, they conventionally require negligible nonlinear effects, which limits the achievable pulse energies in standard fibers with a small mode area [60]. Furthermore, because of the normal dispersion of standard single-mode fibers (SMFs) at the 1 μm range, two different methods are implemented for the stretching and compressing part of CPA systems. It leads to a dispersion mismatch between the fiber stretcher and the grating compressor, further limiting the compressibility of the pulse after the amplification [61]. Another limiting factor is the effect of gain narrowing [8], which is the effect where the center region of the optical spectrum experiences a higher gain than the spectral wings. It leads to a reduction in the optical bandwidth of the amplified pulses, which then, in the case of amplifiers, limits the compressed pulse duration. Consequently, the pulse duration in a typical CPA system at 1 μm cannot be shorter than ~150 fs [62]. All these drawbacks can be addressed with a nonlinear pulse compression stage. However, this would increase the system's complexity.

Another group of amplification methods applies nonlinear pulse propagation to obtain sub-100-fs pulse duration. These methods include direct amplification [63], pre-chirp management [64–66], and using parabolic pulses [67–69]. Nonlinear amplifiers that use pre-chirp management can surpass this limit and achieve energies as high as the microjoule level while maintaining durations as short as 24 fs [66]. However, achieving optimal results requires careful consideration of the seed pulse, which prevents straightforward energy scaling and increases the complexity of the setup. Not only is the difficulty of the system a disadvantage of these methods, but also, in some cases, the use of nonlinear techniques can lead to pulse degradation [70].

2.4.1. Gain-managed nonlinear amplification

Recently, a new method of amplifying laser pulses called gain-managed nonlinear (GMN) amplification was developed [9]. Unlike other methods, GMN amplification uses a nonlinear attractor, allowing a wide range of input pulses to be used. It is achieved through the interaction between self-phase modulation and a gain profile that changes gradually over the length of the amplifier, causing the spectrum to shift towards longer wavelengths during the amplification process in normal dispersion. This method addresses two significant challenges: managing the high nonlinear phase shifts encountered in systems without the stretcher and generating bandwidths much broader than the gain spectrum. Pulses with such a broadband spectrum can be compressed to clean, sub-100-fs pulses.

The simulations conducted by the group of prof. Frank Wise [9] presented the behavior of the pulse inside the GMN amplifier. The numerical model used in this study included second- and third-order dispersive effects, Raman scattering, SPM, self-steepening, and the gain calculated by solving the population inversion rate equations. The evolution of the pulse can be observed in Fig. 2.8. At the beginning, the pulse evolution follows a well-known path, as shown in various publications. Both dispersive and nonlinear effects are predominant, and the pulse quickly evolves towards a self-similar pulse or similariton [67,68]. With increasing energy of the pulse and broadening spectrum, the gain-shaping seems to block the similariton's growth, which leads to the loss of self-similar propagation. Typically, this point was considered to be the limit of self-similar amplification, and systems based on it hardly ever reach useful energies for high-performance applications. However, if the pulse evolution is continued, a GMN regime rises. The spectrum of the pulse shifts towards longer wavelengths while still broadening in both the spectral and temporal domains. Also, the energy of the pulse increases, and the pulse evolves into an asymmetric temporal shape. The chirp of the amplified pulse is monotonic, which allows it to be compensated with a grating pair.

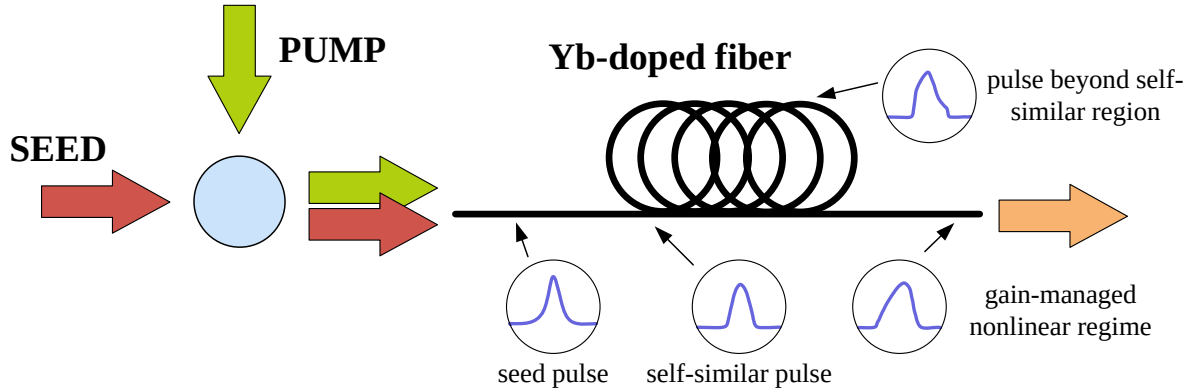

Fig. 2.8. The evolution of the pulse in the GMN regime of amplification. The seed and pump beams are combined and propagate through the active fiber. The pulses go through a self-similar regime to get to the gain-managed nonlinear regime. Based on Ref. [9].

The GMN amplification regime offers simplicity in the setup design, as it only consists of the seed laser and pump, which are combined and go through the active fiber of proper length. The output pulses need to be compressed, but the research showed that it is only adequate to use a simple two-grating compressor [9,71]. Compared to the CPA setup, the stretcher is not needed in the GMN amplifier, and it reduces the size of the system. Additionally, the amplification is easily scalable using the double-clad large mode area (LMA) fibers, as shown in Ref. [72].

The nonlinear attractor for the GMN amplification enables the use of different seed sources and the obtaining of the GMN effect [9], which can reduce or compensate for noise or drift in seed pulses. Most importantly, the spectra obtained for GMN amplification exceed the gain bandwidth of conventional ytterbium-doped fibers, which, in combination with the ability of clean compression of the pulse, makes them an ideal source of amplified pulses for applications requiring ultrashort pulses and high power [10]. So far, the GMN regime was presented experimentally only at the spectral wavelength of 1 μm, but it should be achievable in other spectral regions as long as normal dispersion can be obtained.

2.5. Methods of generating laser light in the mid-infrared

To take full advantage of OFC spectroscopy, it is necessary to have access to mid-IR comb sources. These sources make it possible to address strong fundamental molecular transitions [6] and lead to higher sensitivity in detecting low concentrations. However, it is challenging to access ultrashort mid-IR pulses due to the lack of appropriate gain media and the availability of saturable absorbers. Until the early 2000s, passively mode-locked lasers in the mid-IR were rarely available.

Typical doping of the active fibers allows spectral coverage of frequency combs around 1000-1100 nm for ytterbium (Yb), 1530-1610 nm for erbium (Er), 1750-2100 nm for thulium (Tm), and 2000-2200 nm for holmium (Ho). These OFCs are widely used but only provide light in the near-IR region. The spectral coverage of fiber lasers is presented in Fig. 2.9.

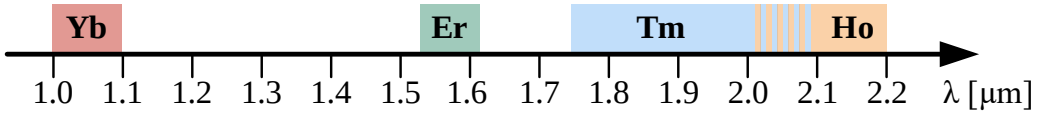

Fig. 2.9. Spectral coverage of fiber lasers in the near-infrared.

In the last several years, an increase in the availability of mid-IR sources has been noticed, mainly attributed to the development of novel materials and the improvement of the quality of the already existing ones. Fig. 2.10 shows an overview of the spectral regions accessible with different laser sources, which include fiber, solid-state, and semiconductor lasers, as well as sources based on nonlinear phenomena. Commonly used sources operating in the mid-IR range are ICLs and QCLs. Due to their narrow bandwidth tunability, they usually allow the measurement of one or a few selected absorption lines [73,74]. ICLs and QCLs emitting light in some particular wavelength regions may require large and bulky cooling systems. However, there are examples of very compact frequency combs built based on QCL and ICL lasers [75,76], but they generate a narrow optical bandwidth (e.g., 50 nm at ~ 3.6 μm [77]). Still, for high-sensitivity spectroscopy measurements in extended averaging times, QCLs require complex computational averaging algorithms to retrieve information from a noisy and unstable spectrum [76]. Additionally, there are no straightforward methods of controlling the f_{rep} and f_0 of QCLs.

For broadband measurement, OFCs emitting light in the mid-IR range are ideal. Sources like this can be based on supercontinuum generation [78,79] and FWM (microresonators) [80]. Nevertheless, for high-precision spectroscopy, there is a need to stabilize a light source to a reference source to have an accurate frequency axis. With absolute frequency stability,

measurements can be conducted to precisely determine the parameters of absorption lines, like their position, intensity, and width. For this type of spectroscopy, stabilized OFCs in mid-IR are required.

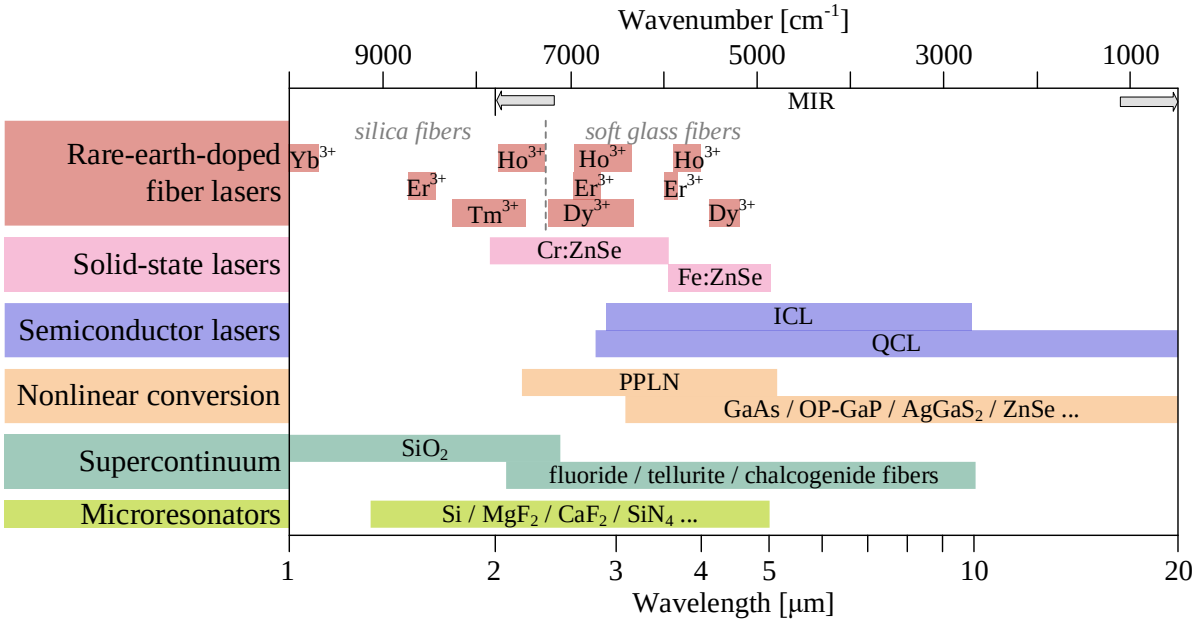

Fig. 2.10. Overview of spectra regions accessible with different laser sources in the mid-IR [6,81–87]. The grey dashed line shows the limit wavelength for using silica fibers. Grey arrows indicate the mid-IR region.

However, regardless of progress made during the last decades in the developments of QCLs, ICLs, mid-IR fiber and solid-state lasers, and supercontinuum sources, their performance in terms of bandwidth, spectral tunability, beam quality, and output power is still worse than compared to the ones generated by nonlinear phenomena as optical parametric amplifier (OPA) or oscillator (OPO) and difference frequency generation (DFG). Various nonlinear crystals make it possible to construct laser sources for multiple spectral ranges, from 3 to 20 μm [88–93].

2.5.1. Nonlinear optical conversion

Nonlinear effects appear when strong radiation fields change the optical properties of materials [94], so lasers with appropriate intensities are needed for these effects to occur. As a result, a part of the input light is converted to a different frequency. The fundamental and well-known example is the SHG, where a light with twice the input optical frequency is generated. For conversion to longer wavelengths, DFG or OPOs are used. In the process of DFG, there is an interaction of two input waves in a nonlinear crystal, one called the pump with the frequency ν_p, and the second called signal with the frequency ν_s. They are overlapped in a nonlinear material, which leads to the generation of a third wave, idler, with a frequency defined by the relation:

$$\nu_i = \nu_p - \nu_s \,. \tag{2.8}$$

The approach to generating an OFC via the DFG process is depicted in Fig. 2.11. Both signal and pump are OFC, alternatively, either the signal or pump can be a single CW laser. For this process to work, phases of the fields in the nonlinear material must match. These phases

change over propagation distances because the refractive index is frequency-dependent. To achieve phase matching over longer distances, the birefringence of the material can be utilized, or quasi-phase matching (QPM) can be used. In the latter, the crystal geometry is inverted to create regular intervals where the dephasing of the light wave is compensated [94]. Respective periods of the geometry inversion establish the phase-matched wavelengths.

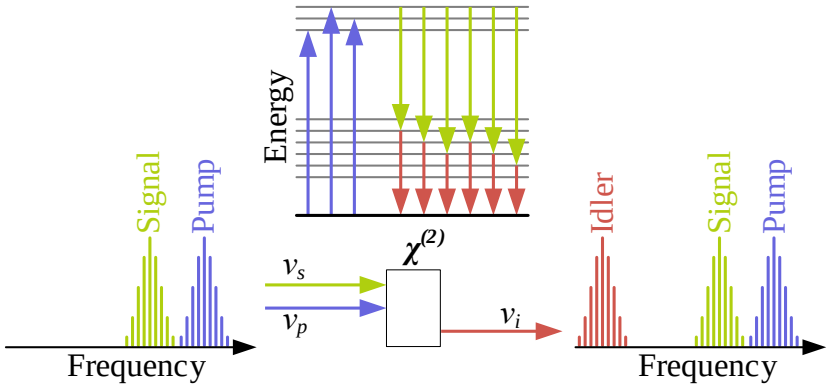

Fig. 2.11. The scheme of difference frequency generation by two combs. In a medium with a second-order nonlinearity $\chi^{(2)}$, nonlinear frequency mixing of the multitude of modes of signal and pump combs occurs. It leads to the generation of various difference frequencies, forming an idler comb in the mid-infrared.

To increase the efficiency of the conversion process, a nonlinear material can be placed in an optical cavity that amplifies the light intensity inside it. This process is known as OPO. In a doubly resonant OPO, both the signal and idler fields are amplified by the cavity, while in a singly resonant OPO, only one of these fields is amplified. Due to the cavity's amplification, only the pump beam is required as input. Other fields emerge through quantum fluctuations and are further amplified at the resonant frequencies. Singly resonant OPOs offer continuous frequency tuning but require higher pump powers in opposition to doubly resonant OPOs. However, for the latter, continuous frequency tuning is not possible because both the idler and signal frequencies must coincide with one of the resonant modes of the cavity [94]. Two approaches to obtaining frequency comb via OPO are presented in Fig. 2.12.

OPOs offer high power and broad bandwidth [95,96] with wide tunability [97,98]. However, in doing so, they require a complex design using optical cavity and free-space optics components. In addition, their free-space cavity needs to be phase-locked to the cavity of the pumping laser, which makes them very impractical in field applications. Considering the characteristics of OPO-based systems, the DFG-based OFCs do not suffer from these problems. They do not require a cavity and can be implemented almost fully from optical fibers, which makes them alignment-free. The details of DFG sources are summarized below.

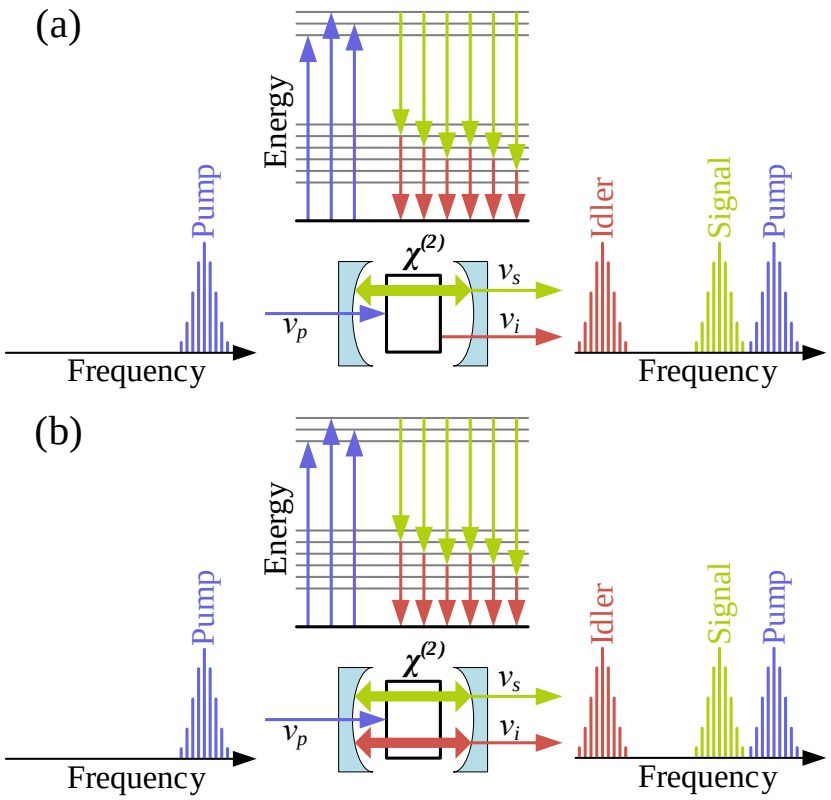

Fig. 2.12. The scheme for optical parametric oscillators based on an optical frequency comb. A $\chi^{(2)}$ nonlinear medium is placed in an optical cavity, which, with a strong pump beam, provides gain to the: (a) signal modes in singly resonant OPO, (b) signal and idler modes in doubly resonant OPO. The idler modes are generated due to energy conservation.

2.5.2. Difference frequency generation

In the process of DFG, the whole spectrum of the OFC described by Eq. (2.5) is downconverted. One method is generating the difference between a CW pump with a frequency ν_p and an OFC [99], where the idler spectrum would be given by:

$$\nu_{i,n} = \nu_p - f_0 - nf_{rep}\,. \tag{2.9}$$

Another example is just using two frequency combs, in particular, the same OFC can generate the signal and the pump, and then only one source needs to be stabilized. If the OFC spectrum is extremely broad, DFG conversion can happen between two edges of the same spectrum, the low- and the high-frequency end. It is then called an intra-pulse difference frequency generation (IDFG), and the spectrum of the obtained idler can also be broad [100–102]. Alternatively, a signal of the OFC can be generated by shifting the pump spectrum towards longer wavelengths, or inversely, the pump can be obtained as a signal shifted towards shorter wavelengths. These effects happen in highly nonlinear fibers (HNLFs) and are called soliton self-frequency shift (SSFS) [103] and dispersive wave (DW) [104] (also referred to as Cherenkov radiation), respectively. Examples of such DFG-based OFC can be found in the literature [105,106]. The approach of blueshifting part of the spectrum benefits from the high coherence of the DW, but the power stored in it is usually low [107]. Then, an extra fiber amplifier in the pump arm is needed to increase the power before the DFG process [105,106]. Without amplification, the resulting mid-IR beam could be limited to single milliwatts [108].

For both signal and pump originating from one OFC source, the f_{rep} and f_0 remain the same, but the light shifts to lower mode indices n. Then, both pump and signal have the same f_0, which leads to the cancellation of the carrier-envelope frequency in the idler wave. The spectrum of the idler in the case of pump and signal originating from the same OFC is given by:

$$\nu_{i,n} = (n_p f_{rep} + f_0) - (n_s f_{rep} + f_0) = n f_{rep}\,, \tag{2.10}$$

where n_p and n_s refer to the pump and signal indices of the OFC. The lack of f_0 can work as an advantage, as only the f_{rep} of the pump needs stabilization to get a fully stabilized idler of the OFC. However, it can also be an issue if both fundamental frequencies of the comb are needed, for example, to lock the OFC to an optical cavity.

For any scheme of DFG, the signal and pump arm pulses must overlap temporally and spatially in the nonlinear crystal. To compensate for any temperature drifts and wavelength tuning due to dispersion, an adjustable delay line is added to one of the paths to reach and conserve temporal overlap. For some systems, the timing of the pulses can be crucial for the overall performance of the setup [109], so automatic stabilization schemes are thus valuable.

When building the OFC in the mid-IR based on the DFG, one must consider the wavelengths needed for the conversion to obtain the requested idler frequency and the right nonlinear crystal. The selection of the crystal for the process is related to the input parameters like wavelengths of the pump and signal beam or their polarization, but foremost, the desired output wavelength. The most popular crystal, periodically poled lithium niobate (PPLN), has a transmission window of up to 5 μm, just like other oxide crystals [110]. Nevertheless, the very dynamic development of modern materials technology has recently resulted in the creation of numerous new crystals that are commercially available. These include, for example, gallium selenide (GaSe) [111], silver selenogallate ($AgGaSe_2$ – AGS) [90], cadmium silicon phosphide ($CdSiP_2$ – CSP) [112], orientation-patterned gallium arsenide (OP-GaAs) [89], or gallium phosphide (OP-GaP) [113]. They are usually characterized by an extensive operating bandwidth, reaching up to several micrometers. Still, they struggle with the simultaneous need for high nonlinearity at high damage resistivity, in addition to higher production costs resulting from continuous development.

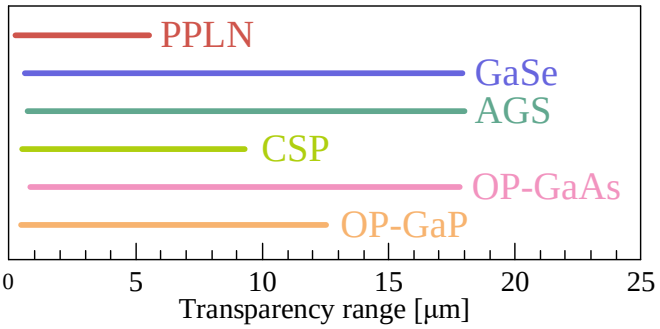

Fig. 2.13. Transparency range for various mid-infrared nonlinear crystals, especially the most popular one (PPLN), non-oxide (GaSe, AGS, CSP), and orientation-patterned (OP-GaAs, OP-GaP). Based on Ref. [110,114].

As presented by Eq. (2.8), the pairs of frequencies meeting the conditions of the equation are infinite. However, most often, they are selected because of their availability. Initial DFG usually starts from a fiber-based laser, which is limited to the gain bandwidth of active material,

in this case, doping of an active fiber. The second wavelength can be arbitrary, but sometimes, due to the need to amplify it, it is also chosen to coincide with the wavelength of a dopant. Different examples are depicted in Fig. 2.14. For the DFG source starting at 1 µm with the Yb-doped fiber laser, the signal can be a wave redshifted towards 1.5 µm vicinity (or somewhere between 1 and 1.5 µm), which would generate the idler in the range of 3-10 µm [93,115–118] (Fig. 2.14(a)). There are two possibilities when using an Er-doped fiber laser at 1.55 µm. For the light blueshifted towards 1 µm, the generated third wave would be in the range of 3-5 µm [105,106,108,119,120] (Fig. 2.14(b)). The wave redshifted in the Tm-doped range (1.7-1.9 µm) would produce the idler at 6-17 µm [111,112,121–124] (Fig. 2.14(c)). Tm-doped fiber laser can also be an initial source to obtain light with wavelengths from 6-12 µm. However, the redshifted wave would have to be near 2.5 µm (Fig. 2.14(d)), which firstly is not a range for any active fibers. Secondly, the redshift would need to happen in a fluoride fiber, as silica fibers have high attenuation at this wavelength. Nevertheless, such examples can be found in the literature [89].

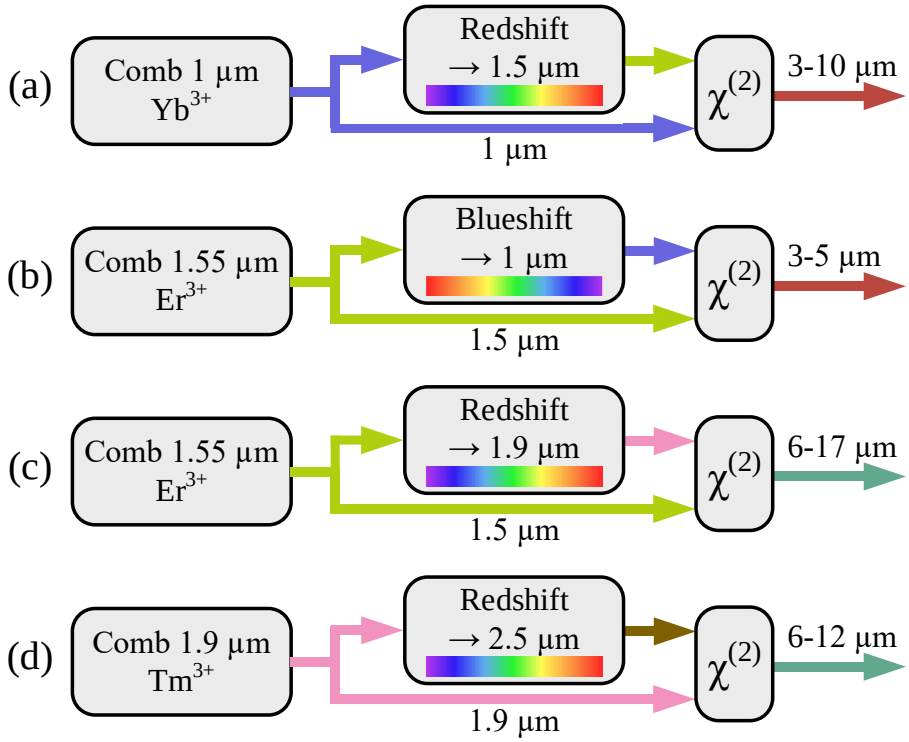

Fig. 2.14. Examples of utilizing the fiber-based OFC and wavelengths in the range of doped fibers to obtain the frequency combs in the mid-IR from the DFG process.

Chapter 3.

Optical frequency comb spectroscopy

3.1. Introduction

Spectroscopy concentrates on the interaction between light (electromagnetic wave) and molecules in any state. The sample absorbs the radiation when the energy of the photons corresponds to the energy difference between two energy levels of a molecule. The absorption strength depends on the concentration of the absorber and the length of interaction between light and absorber. These discrete absorption features are referred to as absorption lines. Their width, shape, and central frequency also depend on a number of environmental parameters. These include the pressure, temperature, and intensity of the interacting light. The absorption spectrum is the variation in the absorption strength as a function of the light's frequency. In addition, light propagating through the sample is not only absorbed but can also experience a phase shift due to molecular dispersion or change its polarization. The gas concentration or parameters of molecular lines can be determined by fitting models to the measured spectra of transmitted light.

Most spectroscopy setups consist of three main parts: a light source, a cell for the gas sample, and a detector for acquiring the transmission spectrum. Proper selection and matching of these three parts has a crucial impact on the parameters of the system for spectroscopy. OFCs provide broadband spectrum, which results in measuring whole absorption bands at once. Regarding suitable gas cells, the absorption sensitivity can be efficiently enhanced by increasing the interaction length between the light and the gas sample. Conventional methods include multipass cells and optical cavities. Nowadays, antiresonant hollow-core fibers are also used, as their empty core can be filled with a gas sample, and the fiber can be coiled to miniaturize the setup. As for the detection part, a Fourier transform spectrometer can measure spectra with high resolution while having a straightforward design of the instrument and fairly easy data processing, and therefore, it is suitable for frequency combs.

This Chapter describes absorption spectroscopy with OFCs. It begins with the presentation of the basics of spectroscopy, together with the advantages of using OFCs as laser sources. Then, different methods of elongating the light-gas interaction distance are discussed, especially multipass cells, optical cavities, and antiresonant hollow-core fibers. Finally, various types of spectrometers are reviewed, emphasizing the Fourier transform spectrometer and its design.

3.2. Laser absorption spectroscopy

The most straightforward example of a direct absorption spectroscopy (DAS) setup includes a laser source that emits light passing through a gas sample and a photodetector that detects transmitted light. The setup is depicted in Fig. 3.1.

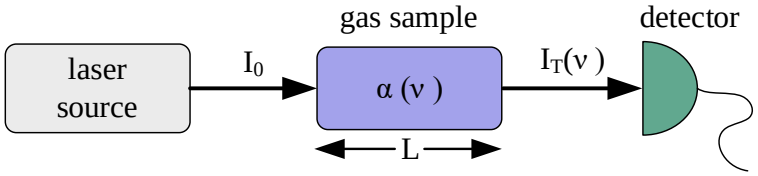

Fig. 3.1. A direct laser absorption spectroscopy setup. The light emitted by the laser source is partially absorbed by the gas sample, and the intensity of the transmitted light is recorded by a photodetector.

The Lambert-Beer law states that the intensity of the light transmitted I_T through the sample, also dependent on the frequency of the light ν, is [125]:

$$I_T(\nu) = I_0 e^{-\alpha(\nu)L}\,, \tag{3.1}$$

where I_0 represents the intensity of the incident beam on the sample, $\alpha(\nu)$ is the frequency-dependent absorption coefficient of the sample, and L is the length of the light-sample interaction. The absorption coefficient is proportional to the absorption strength and the entire interaction length, and is defined as:

$$\alpha(\nu) = \hat{S} N \chi^{abs}(\nu)\,, \tag{3.2}$$

where $\hat{S}$ is the integrated molecular line intensity, N corresponds to the population density of the absorber, and $\chi^{abs}(\nu)$ is the frequency-dependent area-normalized absorption line shape function.

In molecular absorption spectroscopy, when measuring samples in the gas phase, it is more suitable to relate the absorption coefficient to the sample pressure and temperature, assuming the ideal gas [126] in the form:

$$p_A V_A = n_\upsilon k_B \mathrm{T}\,, \tag{3.3}$$

where p_A and V_A are the pressure and volume of the absorber gas, n_υ is defined as the number of molecules in the V_A volume, $k_B \approx 1.381\times10^{-23}$ JK^{-1} is the Boltzmann constant, and T is the gas absolute temperature. Then, the population density N can be expressed as:

$$N = \frac{n_\upsilon}{V_A} = \frac{p_A}{k_B \mathrm{T}} = \frac{p_0}{k_B \mathrm{T}} \times \frac{p_A}{p_0} \times \frac{T_0}{\mathrm{T}}\,, \tag{3.4}$$

where T_0 and p_0 are the standard temperature and pressure (STP), $T_0 = 273.15$ K = 0 °C and $p_0 = 1$ atm = 101.325 kPa = 760 Torr. The first part of Eq. (3.4) can be replaced by the Loschmidt number $n_0 = \frac{p_0}{k_B \mathrm{T}} = 2.686 \times 10^{-29}$ molecules/cm^{-3}, what leads to:

$$\hat{S} N = \hat{S} n_0 \frac{p_A}{p_0} \times \frac{T_0}{\mathrm{T}} = S p c_{rel}\,, \tag{3.5}$$

where c_{rel} is the relative concentration of the absorber, and p corresponds to the total pressure of the sample. S is the integrated gas line strength, defined as:

$$S = \frac{\hat{S}n_0}{p_0} \times \frac{T_0}{\mathrm{T}} \,. \tag{3.6}$$

Then, the product $p_A = pc_{rel}$ is the partial pressure of the absorber in the gas sample. Knowing the variables introduced above, the absorption coefficient can be written as:

$$\alpha(\nu) = Spc_{rel}\chi^{abs}(\nu)\,, \tag{3.7}$$

using the relative pressure of the absorber, integrated gas line intensity, and total pressure of the sample. From Eq. (3.1), the absorption coefficient can be calculated from the incident and transmitted light intensities and the length of the interaction:

$$\alpha(\nu) = \frac{1}{L}\ln\frac{I_T(\nu)}{I_0}\,, \tag{3.8}$$

therefore, if the integrated absorber gas line strength and the sample total pressure are known, the relative absorber concentration can be determined.

When measuring the absorption spectrum of a sample, one needs to be aware of the line-broadening processes, which may come from several mechanisms and ultimately will limit the precision of determining the line frequency. When a light beam probes a gas sample, the thermal motion of the molecules gives rise to Doppler broadening, which produces Gaussian line shapes and is often the dominant broadening mechanism at low gas pressures, known as the Doppler limit [125]. Apart from Doppler broadening, another limitation is the natural linewidth of the transition, which comes from the finite lifetime of the energy states of the absorbing molecules [127]. It causes a Lorentzian line shape of the absorption lines. These absorption profiles cannot always be sufficient in every case. When a Doppler-broadened transition is also affected by non-negligible natural and collisional broadening (especially in the case of a gas at high pressure), then the line takes a form that is a convolution of the Lorentzian and Gaussian profiles. It is known as the Voigt profile [128]. There are also higher-order effects, which require more sophisticated line-shape models [129]. Such effects become relevant in measurements of high sensitivity, but for the purposes of this dissertation, the Voigt profile is satisfactory. The line shapes discussed here are presented in Fig. 3.2.

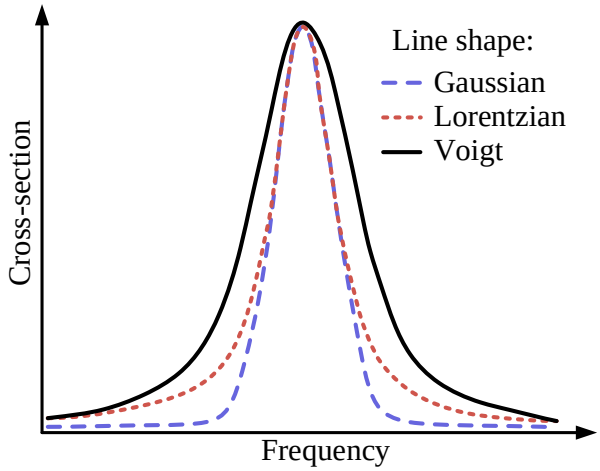

Fig. 3.2. A comparison of Gaussian, Lorentzian, and Voigt line shapes. The Voigt profile is a convolution of Gaussian and Lorentzian profiles. All profiles are normalized to peak absorption.

The main advantages of DAS are the simplicity of the experiment and the fact that it allows the absorption assessment without additional calibration. However, the signal is detected at low frequency, where the *1/f* noise tends to be high, thus limiting the detection sensitivity. In addition, the DAS technique provides only molecular absorption, while dispersion information is lost, which may be necessary for some applications. This sensitivity problem can be mitigated by techniques requiring modulation of the laser wavelength, which shifts the signal detection to higher frequencies [130], where the effect of the *1/f* noise is less pronounced. More sophisticated methods use high modulation frequencies and thus allow probing of both absorption and dispersion of the gas sample simultaneously [131]. However, the most common and efficient method of increasing the absorption sensitivity is elongating the light-sample length, as the absorption signal scales with the interaction length between the light and the gas. This topic will be discussed in detail in Section 3.3.

3.2.1. Direct frequency comb spectroscopy

Gas sensors built based on single-frequency sources allow the measurement of a single, selected absorption line [132,133] or several within a narrow spectral region covered by laser tunability [73,74]. Although external cavity lasers have been used for multispecies detection, their complexity poses a significant drawback [134]. By increasing the spectral width of the laser, multiple absorption lines can be detected simultaneously. The use of OFCs is one of the techniques enabling broadband detection. In 2004, the term direct frequency comb spectroscopy appeared for the first time [135]. In recent years, numerous novel techniques have been developed [136–140], where a vast number of absorption lines of the absorbing sample is probed by the frequency comb. Direct absorption frequency comb spectroscopy offers short measurement times, high accuracy, and high sensitivity over a broadband spectra range. The comparison of transmission spectra through a gas sample with a broad absorption line for tuned CW laser and OFC is presented in Fig. 3.3.

The only obstacle is that, unlike single-frequency laser, the usage of OFC forces the measurement of the output optical spectrum to recover absorption information, and therefore, a spectrometer is needed. Different methods of acquiring the spectra of a frequency comb in DAS are discussed in Section 3.4. If the resolution of the spectrometer is high enough, one can resolve individual comb lines, which allows for self-calibration of the frequency scale. Then, the repetition rate of the OFC determines the spectral resolution of the measurements. When the spectrometer resolution is equal to or better than the comb line spacing, the width of individual comb lines is convoluted with the spectrometer's instrumental line shape (ILS). When the atomic and molecular resonances have a width similar to or broader than the f_{rep} of the comb and the comb has narrow lines, the contribution of the ILS can be neglected. If the sample does not change in time, the resolution of the measurement can be further scaled up by interleaving several spectra recorded with a tuned f_{rep} or f_0. Then, the resolution can be reduced to the intrinsic comb linewidth [141].

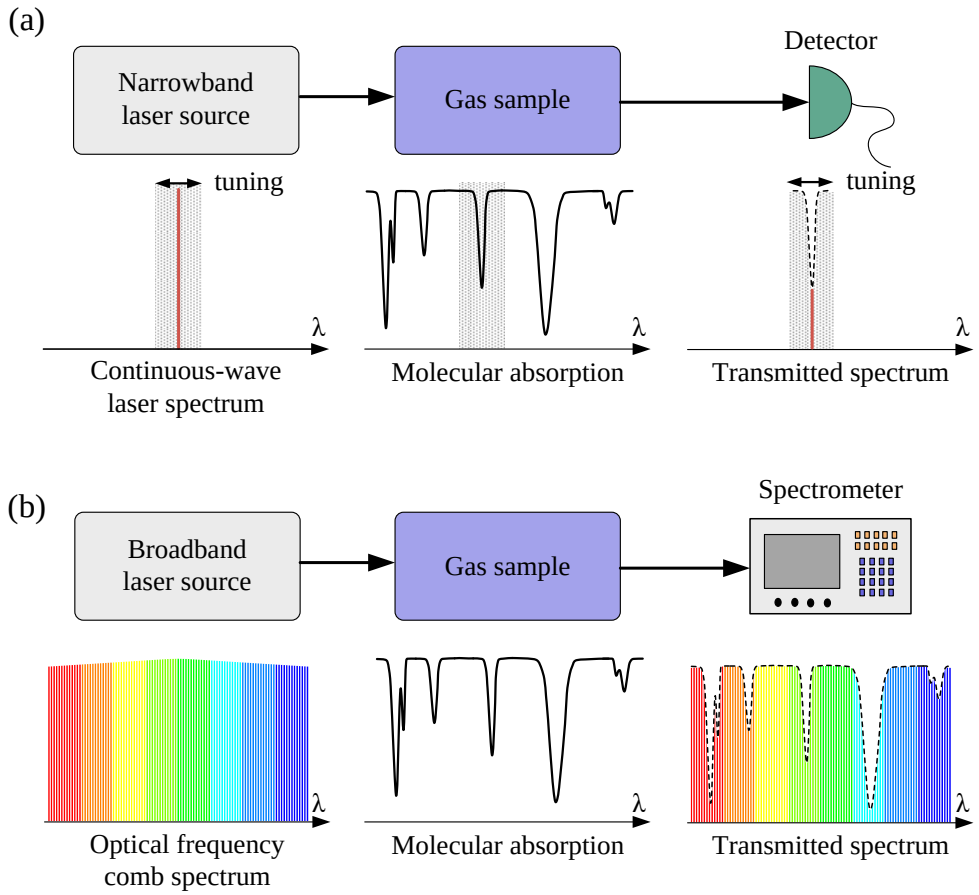

Fig. 3.3. Comparison of the direct absorption spectroscopy for (a) a tuned continuous-wave laser and (b) an optical frequency comb. Only part of a molecular absorption can be detected for a tuned CW laser, usually one or a few lines. For OFC, whole bands of molecular absorptions are detected at the same time.

Spectroscopy using broadband sources enables multiline fitting [142] as well as multispectral fitting [143]. Despite having similar names, these two concepts differ from each other significantly. In multiline fitting, a multitude of molecular transitions are measured at the same time, which comes down to a quantitative assessment of the gas concentration. The precision of the fitting is improved in comparison to single-line fits, as the fitting precision is scalable with the area under the spectrum [142]. In the multispectral fitting, the same spectra are measured at different conditions, and then the line fit is used globally to retrieve one parameter. It helps to decouple correlated parameters and, as a result, increases their fitting accuracy [143]. In this dissertation, only the multiline fitting is presented, as the research utilizes only quantitative fitting of gas concentrations.

3.3. Enhancing the absorption signal

From Eq. (3.1), one can notice that direct measurement of the sample's absorbance is essentially the detection of a decrease in the transmitted light intensity at specific frequencies. The detected light intensity inherently contains a certain amount of noise, which can originate from the light source itself (intensity noise) or the detector circuit (detector noise) but is also basically limited by statistical variations in the number of photons reaching the detector in a given time (shot noise). Therefore, the absorption signal must be as strong as possible compared to the noise

level. A parameter used when describing and comparing spectroscopic setups is the sensitivity, often reported as the noise equivalent absorption (NEA) coefficient. Although tunable CW lasers can achieve high sensitivity, it is only for individual spectral features. Using broadband sources enables achieving good sensitivity over an extended range. To account for the multiplex character of OFC, the NEA per spectral element is usually calculated. It is given by:

$$\alpha_{min} = \frac{\sigma}{L_{eff}} \sqrt{\frac{T}{M}} \,, \tag{3.9}$$

where σ is the noise on the baseline, L_{eff} represents the effective interaction length, T is the total acquisition time, and M introduces the number of spectral elements (calculated as measurement span divided by its resolution). To determine the noise floor level, two background spectra are divided by each other, and the standard deviation of their ratio is calculated. From the given formula, it can be noticed that the sensitivity can be enhanced either by reducing the noise level or increasing the interaction length.

In this dissertation, two methods are used to reduce the impact of noise fluctuations. One is universally applied, and it is averaging the detected signal over time. The second one uses balanced detection, where two signals carrying noise from the same sources are subtracted to detect differences between them while canceling the common noise. Elongating the distance that light interacts with the gas sample is another method of enhancing the absorption signal and, therefore, the sensitivity. The most straightforward type of gas sample container is a single-pass cell through which the light beam passes once. Unfortunately, the length of such a container is limited for practical reasons. The two most popular ways of increasing light-gas interaction length while maintaining the cell compact are multipass cells (MPCs) and enhancement cavities. Another recently introduced technique is based on using antiresonant hollow-core fibers (ARHCF), as their empty core can be used to store a gas sample. All three of these methods are briefly described in the following Sections. However, it should be pointed out that the absorption signal cannot be enhanced indefinitely in this way because if the path length is long enough, all the light will be absorbed at the transitions. Longer path lengths will eventually result in saturation, which leads to the broadening of absorption lines [125].

3.3.1. Multipass cell

In MPCs, the laser beam is reflected between mirrors, achieving an effective optical path length many times larger than the cell size itself. Historically, the first solution of this type was presented by A.H. Pfund in 1939 [144]. The proposed optical system consisted of two spherical mirrors and allowed for three reflections. Nowadays, the MPCs can provide tens of meters of additional path length, although longer path lengths tend to result in greater power losses due to a higher number of reflections. There are two main types of commonly used MPCs, and their laser beam paths are depicted in Fig. 3.4. The White cell [145], shown in Fig. 3.4(a), is built from three mirrors with the same focal lengths but different shapes. The number of reflections can be adjusted by changing the angles of the mirrors. Presented in Fig. 3.4(b), the Herriot cell [146] is composed of only two fixed mirrors placed in one optical axis at a certain distance. The design is simpler and more robust than the White cell. A less popular type of MPC is based on a circular configuration [147].

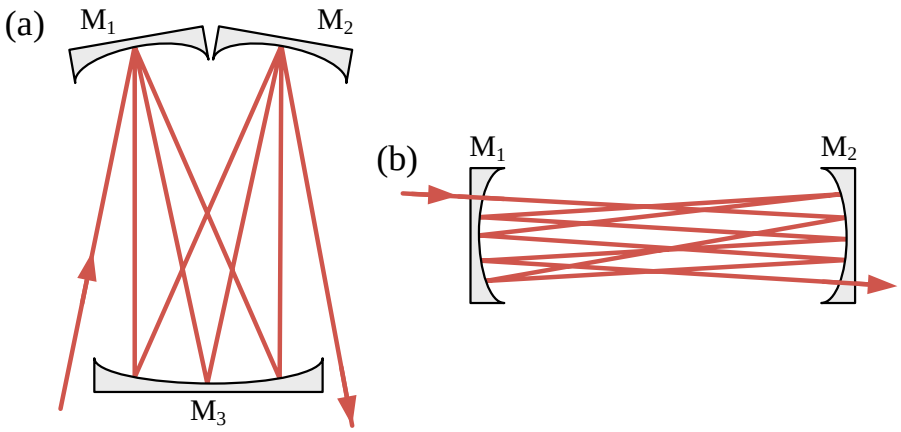

Fig. 3.4. Diagram of the laser beam path between mirrors (M) for (a) White cell and (b) Herriot cell.

An MPC requires careful alignment of the input beam to obtain the output beam after the correct maximum number of passes defined by the cell design. It usually involves pre-alignment using a visible laser beam to produce a specific beam reflection pattern on the mirrors of the cell, as the actual source used for spectroscopy may not be in the visible range. A convex lens is usually recommended in front of the cell to obtain a beam waist in the center of the cell and avoid convergence of the output beam. The volumes of the MPCs are usually larger than those of the optical cavities, as they use larger mirrors and dissimilar geometries.

3.3.2. Enhancement cavity

The other configuration for increasing the interaction length is an external optical resonant cavity (or a resonator), also called an enhancement cavity. In general, resonant cavities are an integral part of lasers but can also be found in nonlinear conversion processes like OPOs. They can have diverse configurations (for example, V-shape and bow-tie) or be different types, like linear or ring. The Fabry-Pérot cavity is comprised of two parallel, partially transmitting mirrors, shown in Fig. 3.5(a). Only specific wavelengths satisfying the appropriate condition [148] can resonate in the cavity, which leads to an enhancement of the intensity. For each reflection at the mirrors, a small fraction of the intensity is coupled out. The M_1 mirror reflects light with wavelengths that do not fulfill the resonant requirement, and they do not enter the cavity. As a result, only specific optical frequencies equivalent to the cavity modes can resonate. The *FSR* of the cavity for vacuum and separation of the mirrors *L* was already given by Eq. (2.1), as the laser cavity and enhancement cavity are similar. The mode structure of the cavity is shown in Fig. 3.5(b).

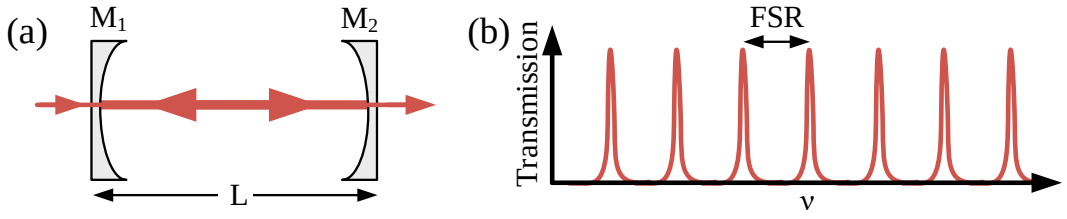

Fig. 3.5. (a) Diagram of the laser beam path between two mirrors (M) separated by the distance *L* in the Fabry-Pérot cavity. (b) Representation of the resonant cavity modes in the frequency domain separated by the *FSR*.

Characteristic parameters of optical cavities are the reflection coefficient of the mirrors r and the finesse F. The finesse is the ratio of the FSR to the full width at half maximum (FWHM) of the cavity modes Γ_c:

$$F = \frac{FSR}{\Gamma_c} = \pi \frac{\sqrt{r}}{1-r} \ . \tag{3.10}$$

If the cavity was empty, and the mirrors were perfect ($r \approx 1$), the light passing through the cavity would be unaffected by scattering, and the maximum transmission would reach 1. The average effective optical path L_{eff} of a photon in the cavity is equal [149]:

$$L_{eff} = \frac{2F}{\pi} L \ . \tag{3.11}$$

From Eq. (3.11), it can be noticed that the absorption in the optical cavity is enhanced by a factor of $2F/\pi$, where F can reach even up to several thousand. Hence, optical cavities are highly effective in increasing the effective light-gas interaction path length, translating into the detector sensitivity. However, most cavity-enhanced techniques require tight stabilization of the laser frequency to the cavity (or vice-versa). One spectroscopy scheme does not necessarily require this, and it is called cavity ringdown spectroscopy (CRDS). It uses high Finesse cavities and the characteristic decay time of the pulsed light intensity trapped in the gas-filled cavity [150,151]. It is sufficient for CRDS to couple in just part of the light and measure its decay time.

Another downside of the enhancement cavities is meeting the mode-matching conditions while coupling the light into a cavity. It means that the collimation parameters of the input light need to be matched with the fundamental transverse mode of the cavity, which is defined by the curvature of the mirrors [152]. Finally, the light spectrum transmitted through a cavity cannot simply be converted to the absorption coefficient using the Lambert-Beer law. Instead, the transmission function needs to be modeled with all its parameters, which makes the analysis much more complicated than when using MPCs.

3.3.3. Antiresonant hollow-core fiber

At the end of the 20th century, a breakthrough in optical fiber technology known as hollow-core fiber (HCF) occurred. The HCF, distinguished by its unique structure and capacity to guide light through the air via the photonic bandgap effect rather than conventional total internal reflection, initiated a revolution in the field [153]. In the following years, HCFs enabled light propagation in the mid-IR spectral range, where traditional solid-core fibers encountered significant attenuation issues due to material properties. Presently, three primary types of HCFs have been proposed, manufactured, and successfully deployed across various applications, including laser spectroscopy. These fiber types include the hollow-core photonic bandgap fiber (HC-PBGF) [153], Kagome HCF [154], and antiresonant hollow-core fiber [155]. As a part of this dissertation, the ARHCF is successfully used in broadband laser spectroscopy, and the results are discussed in detail in Section 5.4. Choosing this fiber type is related to the better performance and versatility of ARHCF in comparison to different kinds of HCFs [156].

The ARHCFs are commonly designed with non-touching capillaries inside and an air core where the light propagates. The scheme of the ARHCF is shown in Fig. 3.6. The production of ARHCFs relies on the widely employed stack-and-draw method [157]. Typically, these fibers are drawn from high-purity fused silica glass, such as Suprasil F300 [158]. Nonetheless, because of the substantial material absorption of silica glass at wavelengths exceeding 5 μm, several successful efforts have demonstrated the fabrication of ARHCFs using borosilicate and telluride glass for longer wavelengths [159,160]. A considerable advantage of using HCFs for laser spectroscopy is their small size, which corresponds to the low volume of the gas sample needed to fill the fiber.

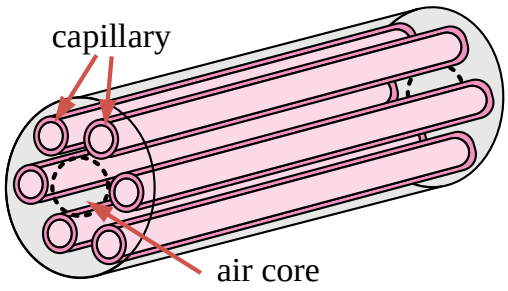

Fig. 3.6. Scheme of an antiresonant hollow-core fiber. The air core is surrounded by non-touching capillaries.

The light guidance mechanism can be described by the antiresonant reflecting optical waveguiding (ARROW) principle [161] and inhibited coupling to a low density of states cladding modes [162]. The model is depicted in Fig. 3.7(a). In the ARROW effect, the walls of capillaries are regarded as a Fabry-Pérot resonator formed by low and high refractive index regions (n_1 and n_2). The resonant optical frequencies with the formed resonator will not propagate in the core but leak into the cladding, where they will experience high material attenuation. So, only the optical frequencies matching the antiresonance of the core boundary layer can be propagated through the fiber with low losses. The antiresonant wavelength range supported by the ARHCF can be computed according to the following equation [161]:

$$\lambda_{antires} = \frac{4y}{(2m+1)}\sqrt{n_2^2 - n_1^2}\ , \tag{3.12}$$

where y corresponds to the capillary wall thickness, m = 0, 1, 2, …, and n_1 and n_2 are the refractive indices of the air and material forming the glass capillaries. The scanning electron microscope (SEM) image of a typical ARHCF fiber is presented in Fig. 3.7(b).

According to the provided equation, it can be concluded that the low-loss transmission window relies primarily on the thickness of the capillary walls rather than the core size. However, in Ref. [163], researchers indicated that the hollow-core diameter of the ARHCF and the diameter of the cladding capillaries significantly influence the bending characteristics and the ability to guide single-mode beams. It has been demonstrated that both dimensions must be carefully chosen to achieve an optimal core/capillary diameter ratio of approximately 0.65. This ratio enables single-mode transmission within the low-loss window of the fiber by increasing the loss ratio between the fundamental mode and the higher-order modes supported by the fiber [163].

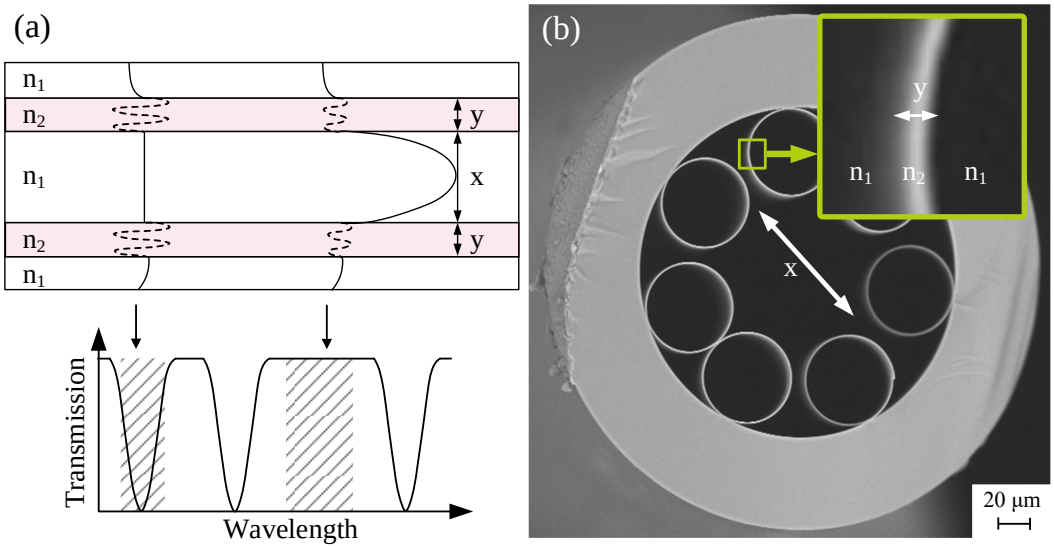

Fig. 3.7. Light guidance mechanism in ARHCF. (a) 2D representation of ARHCF with a light transmission in the core. (b) SEM image of the ARHCF [164]. x, core diameter; y, capillary wall thickness; n_1, refractive index of air; n_2, refractive index of the capillary walls.

ARHCFs have found successful application in gas spectroscopy employing various laser-based sensing methods, like tunable diode laser absorption spectroscopy (TDLAS) [165,166], wavelength modulation spectroscopy (WMS) [167,168], photothermal spectroscopy (PTS) [169,170] and photoacoustic spectroscopy (PAS) [171]. Studies have demonstrated that laser spectroscopy with ARHCFs can target molecules with transitions occurring within the wavelength range extending up to 10 µm, a capability not achievable with other types of HCFs [172,173]. Moreover, ARHCF-based detectors can analyze gas mixtures containing molecules with transitions occurring in both the near- and mid-IR regions thanks to their two distinct spectral bands [158].

3.4. Spectrometers for broadband sources

Spectroscopy methods using the full spectral bandwidth of an OFC require a spectrometer with a broadband detection system. Two groups of techniques, based on interferometry or dispersion, are usually combined with an OFC. Example schemes of the methods described in this Section are depicted in Fig. 3.8. In the interferometric method implemented through the Fourier transform spectrometer (FTS) [106,138,174,175], a Michelson interferometer with a mechanical stage is used (Fig. 3.8(a)). The interferograms in the time domain using a single diode are detected, while the optical path difference (OPD) between the two arms of the interferometer is scanned.

This approach can also be performed using two frequency combs with slightly different repetition rates, which resembles the effect of a fast-scanning delay line. This concept is called the dual-comb technique [140,176,177] and is based on measuring a copy of the comb signal at low frequencies with a fast photodetector (Fig. 3.8(b)). The interferogram produced by two combs with slightly shifted repetition rates maps the fast modulation of the OFC electric field into the intensity of the interferogram. In comparison to comb-based FTS, dual-comb spectroscopy is free of geometrical arrangement and provides much faster time resolution, as it is given by the reciprocal difference between the two repetition rates of the combs.

However, the operation of dual-comb spectroscopy requires strict mutual coherence between two combs, which limits the number of applicable dual-comb sources, especially in the mid-IR.

The dispersion-based spectrometers using gratings are usually simpler, faster, and more compact than the FTS, but they provide lower spectral resolution. In order to improve their resolution, an additional dispersive and/or filtering method is implemented. A second dispersive element can be a virtually imaged phased array (VIPA) [178], which disperses the OFC in a perpendicular direction to the dispersion of a grating (Fig. 3.8(b)). The implementations of a VIPA etalon with a camera have demonstrated high sensitivity [179,180] and offer compact and fast detection systems. Unfortunately, these techniques rarely resolve comb mode spacing, and the detector size limits the simultaneous spectral coverage, so broadband measurements need sequential recording.

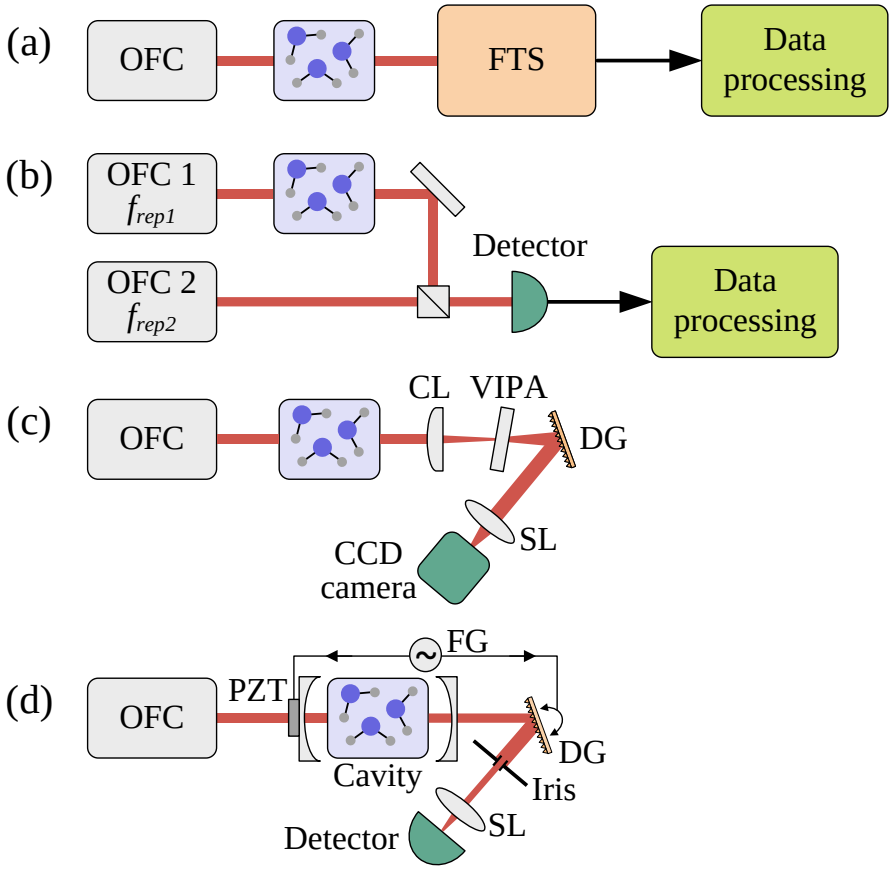

Fig. 3.8. Possible detection schemes for OFC spectroscopy. (a) Beam after a gas sample is analyzed with mechanical FTS. (b) Dual-comb technique, where the beating between two OFCs is detected on a single detector. (c) After the absorption, the light is dispersed with a VIPA and a grating and detected on a camera. (d) Vernier spectrometer uses a cavity for mode filtering. OFC, optical frequency comb; FFT, fast Fourier transform; CL, cylindrical lens; VIPA, virtually imaged phased array; DG, diffraction grating; SL, spherical lens; PZT, piezoelectric transducer; FG, function generator;

A different approach is Vernier spectroscopy (Fig. 3.8(d)), where comb modes are filtered with a cavity before being dispersed and imaged onto a camera [181]. Due to the heavy filtering of the comb, most of the transmitted OFC power is lost, and the high-power comb is needed to achieve an acceptable SNR. Additionally, the OFC and the filter cavity need stabilization, or else any residual frequency jitter will be converted into amplitude noise, which leads to the degradation of the system's sensitivity. The issue of low power is addressed in a technique

called continuous-filtering Vernier spectroscopy [182,183], where a group of several comb modes (Vernier orders) are transmitted through the cavity. There is no need for stabilization of the comb and cavity due to the inherent noise immunity of the technique. To resolve comb modes, a comb-resolved Vernier spectroscopy can be used [181,184]. However, unlike comb-based FTS, Vernier spectroscopy loses the absolutely calibrated frequency scale.

An advantage of mechanical FTS over dispersion-based spectrometers is the broad simultaneous wavelength detection with a single detector, which is not limited by the coatings of the optical dispersive elements. In addition, with appropriate sampling, the resolution of comb-based FTS is given by the linewidth of the comb modes, allowing the measurement of undistorted high-resolution spectra [141]. These characteristics resulted in the mechanical FTS being chosen as a method of obtaining the spectra for the measurements performed as a part of this dissertation.

3.4.1. The Michelson interferometer

FTSs [185] were first invented in the 1950s and since then have been broadly used for infrared spectroscopy with incoherent light sources, known as Fourier transform infrared (FTIR) spectroscopy [186]. Substituting the thermal sources with OFCs provides substantial improvements, like higher SNR, shorter acquisition time, and easier coupling of the light. The standard FTS is based on the Michelson interferometer and is shown in Fig. 3.9. It consists of a beamsplitter (BS) and two plane mirrors that are perpendicular to each other. One of the mirrors (M_2) moves linearly in the direction indicated by the arrow. The monochromatic light beam with a wavelength λ, entering the interferometer, is split into two beams with amplitudes equal to half of the input beam. Both of these beams are then reflected from the mirrors and recombined at the BS again, then directed to the photodetector, where they interfere with each other.

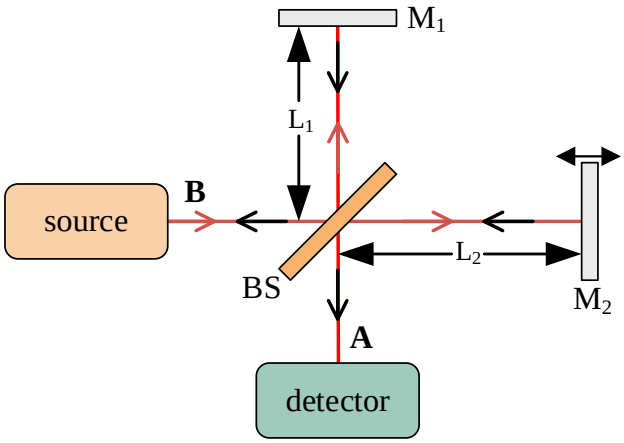

Fig. 3.9. Diagram of Fourier transform spectrometer based on Michelson interferometer with a light source, two mirrors (M_1 and M_2), a beamsplitter (BS), and a detector (placed at point A). The incoming beam is indicated by red arrows, and the reflected beam by black arrows.

Assuming that the light beams are parallel after the recombination at the BS, two parameters, L_1 and L_2, can be determined, which represent the paths of the light beams from the BS to mirrors (M_1 and M_2). This way, the *OPD* parameter can be determined, which can be represented by the formula [187]:

$$OPD = n \cdot (L_1 - L_2) = n \cdot \Delta L\,, \tag{3.13}$$

where ΔL is the difference between the L_1 and L_2 paths, and n is the refractive index of the FTS medium. Usually, the FTS is surrounded by the air, therefore, for further consideration, let us assume $n = 1$. When L_2 is equal to L_1, the OPD is zero, thus, both beams are in phase and interfering constructively, and the maximum intensity is recorded on the detector. As the M_2 moves away, the intensity on the detector decreases with the introduction of the phase difference. When the OPD is equal $\lambda/2$, destructive interference occurs, and the light beams are in opposite phases. Thus, when the mirror moves at a constant speed, the detector records an intensity with a sinusoidal modulation as a function of the mirror displacement with a period of $\lambda/2$. The intensity at the detector (point A) is then given by [125]:

$$I_A = \frac{1}{2} I_0 \left(1 + \cos\left(\frac{2\pi\nu_0 \Delta L}{c}\right)\right), \tag{3.14}$$

where I_0 is the intensity of a light source beam with the frequency ν_0. The plot of this intensity as a function of the OPD is called an interferogram, which then represents the spectrum of the input signal after a fast Fourier transform (FFT). Fig. 3.10 shows the interferogram of a monochromatic light source and its spectrum after the FFT.

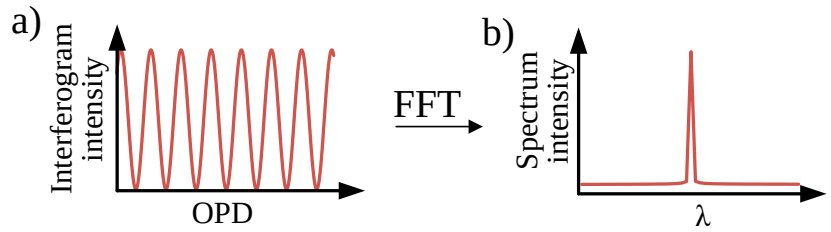

Fig. 3.10. (a) An interferogram of a monochromatic light acquired by the FTS. (b) The spectrum of monochromatic light after the FFT of the interferogram.

The reflected beam reaching point B is shifted in phase by 180° compared to the beam in point A due to a different number of reflections. The light intensity at point B is given by:

$$I_B = \frac{1}{2} I_0 \left(1 - \cos\left(\frac{2\pi\nu_0 \Delta L}{c}\right)\right). \tag{3.15}$$

The idea for balanced detection is to subtract the intensities from points A and B to obtain the signal:

$$I = I_A - I_B = I_0 \cos\left(\frac{2\pi\nu_0 \Delta L}{c}\right), \tag{3.16}$$

where the amplitude of the interferogram is doubled, and the intensity noise is canceled. It is important to note that the powers at points A and B must be equal for optimum noise performance. It is generally not achievable in real interferometers due to unequal splitting ratios of the BS and losses along the beam pathways. The above description also assumes that the contrast of the interferogram is 100%, which is not the case in practice.

When using the FFT algorithm on the interferogram to get the spectrum, the sampling points are spaced by the $\delta\nu$ obtained as:

$$\delta\nu = \frac{c}{\mathrm{OPD}_{max}}\ , \tag{3.17}$$

where OPD_{max} is the maximum OPD of the interferometer. $\delta\nu$ is known as the interferometer's nominal resolution. Therefore, the higher spectral resolution calls for a longer scanning distance of the mirror, and this limits the resolution of FTS, as the instrument cannot be made indefinitely large.

A further consequence of the interferogram's clipping is an ILS of the peak that appears in the spectrum at ν_0. If the interferogram is simply clipped without any additional apodization function being applied, the spectrum will be convolved with an ILS function given by the following equation [188]:

$$g_{ILS} = \frac{OPD_{max}}{c}\frac{\sin(\pi\nu OPD_{max}/c)}{\pi\nu OPD_{max}/c}\ . \tag{3.18}$$

The g_{ILS} is a sinc function, depicted in Fig. 3.11. Its shape is carried over to the detected frequency peak at ν_0, which is broadened by the ringing that occurs on the wings. It should be noted that the ILS function has a zero value if the detuning is an integer value of the nominal resolution $\delta\nu$.

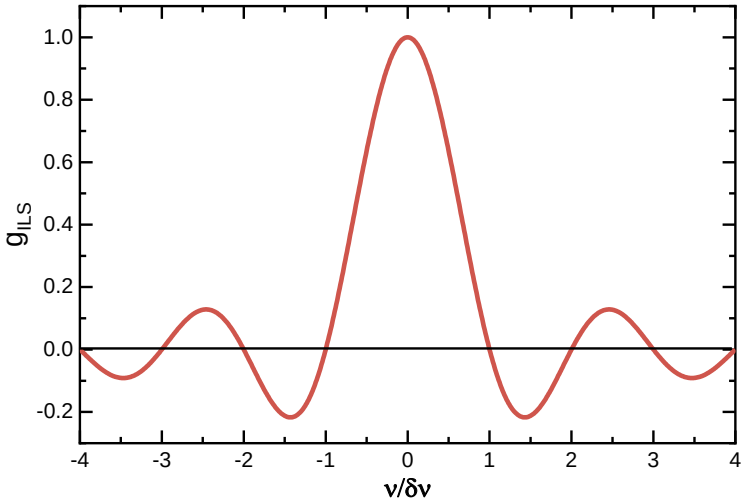

Fig. 3.11. The ILS function due to the truncation of the interferogram. Zero crossings occur when ν is an integer times $\delta\nu$.

3.4.2. Fourier transform spectrometer with optical frequency combs

When it comes to polychromatic light sources measured by the FTS, the interferogram becomes a sum over all frequency components:

$$I = \sum_n I_n \cos\left(\frac{2\pi\nu_n \Delta L}{c}\right). \tag{3.19}$$

The superposition of all the sine waves results in an interferogram consisting of a burst with maximum intensity when the OPD equals zero. Fig. 3.12 presents the interferogram of a polychromatic light source and its spectrum after the FFT.

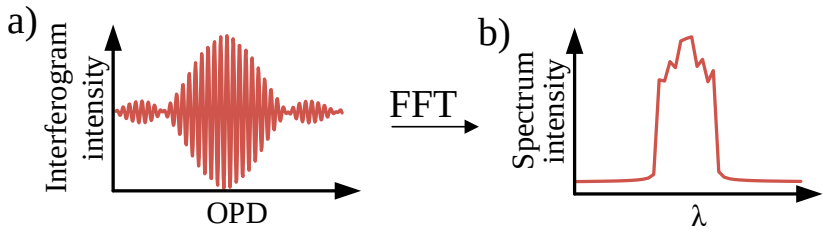

Fig. 3.12. (a) An interferogram of a polychromatic light acquired by the FTS. (b) The spectrum of polychromatic light after the FFT of the interferogram.

As the OFC produces a series of coherent pulses in the time domain, its interferogram consists of a series of bursts appearing at *OPD* equal to integer multiples of c/f_{rep}. An example of such an interferogram is depicted in Fig. 3.13. To resolve individual comb modes, the nominal resolution needs to be smaller than the comb spacing, $\delta\nu < f_{rep}$, which is equivalent to $OPD_{max} < c/f_{rep}$. Nevertheless, the gaps between the comb lines contain no spectral information, and it is adequate to obtain an interferogram of length equal $OPD_{max} = c/f_{rep}$, which results in matching the spectral point spacing to the comb mode spacing. For example, to match the comb mode spacing of an OFC with a repetition rate of 125 MHz, one should have an interferometer with an *OPD* of 1.2 m.

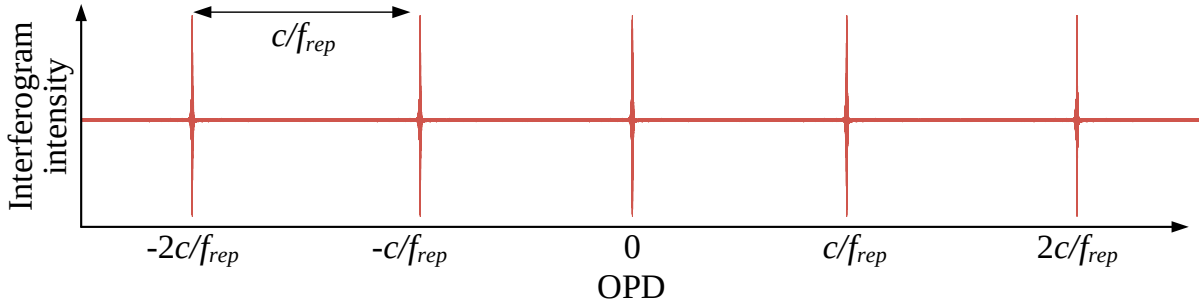

Fig. 3.13. Interferogram of an optical frequency comb in the *OPD* domain. At every integer multiple of c/f_{rep}, there is a burst.

For narrowband sources like CW lasers, the convoluted spectral shape measure in the FTS is identical to the ILS function. For the OFC composed of thousands of narrow modes, the convolution of each mode occurs as a sinc function with the same periodic zero crossing at integers of $\delta\nu$. Thus, it is possible to avoid the ILS distortions if the *OPD* is precisely matched to c/f_{rep}, the f_0 of the comb is fixed, and the sampling points are precisely at the multiple integers of c/f_{rep}. This technique is called the sub-nominal resolution method [141].

If the measured molecular absorption lines are narrower than the repetition rate of the OFC, only individual comb lines are absorbed, which results in one sample point per absorption line. To map the full absorption line profile, one needs to interleave single burst spectra taken at different OFC scales. It can be achieved by either stepping the f_{rep} or f_0. The preferred method is stepping the f_0 because the resulting linear shift can be easily corrected in post-processing.

3.4.3. Design of the FTS

A general schematic of the implemented FTS used for the experiments presented in this dissertation is shown in Fig. 3.14. The FTS is based on the Michelson interferometer, but instead

of one arm, both arms are movable, providing a doubling of the *OPD* (as one arm lengthens, the other shortens).

The mirrors used in the FTS are gold-coated, and their reflectance remains above 96% in the spectral range from 800 nm to 20 µm. The mirrors at the end of the two moving arms of the interferometer are gold-coated retroreflectors (Edmund Optics, 49-675). This type of mirror consists of three mutually perpendicular, intersecting, and planar surfaces, which provide the reflected beam to be parallel to the incident beam, regardless of the angle of incidence. The retroreflectors were mounted back-to-back and placed on a high-accuracy linear sliding table with a stepper motor with 1000 mm of travel (Aerotech, ACT115DL). This configuration allows the *OPD* to be doubled, compared to the setup where only one of the arms is moved by the same distance. The maximum *OPD* of the FTS equals 4 m, which corresponds to the nominal resolution of 75 MHz. For the OFC with a repetition rate of 125 MHz, to match the comb spacing, the linear stage should move by only 0.6 m. Both reflected beams are detected by a pair of HgCdTe detectors (VIGO Photonics, PVI-4TE-10.6-1×1) in a balanced configuration. In addition to a focusing lens, an adjustable pinhole is placed in front of each detector in order to balance the powers, thus optimizing noise canceling and improving the interference contrast. The detectors have high detectivity in the 3.2-11.8 µm range, but by replacing the detectors, the working range of the FTS can be extended either to shorter (2 µm) or longer (15 µm) wavelengths.

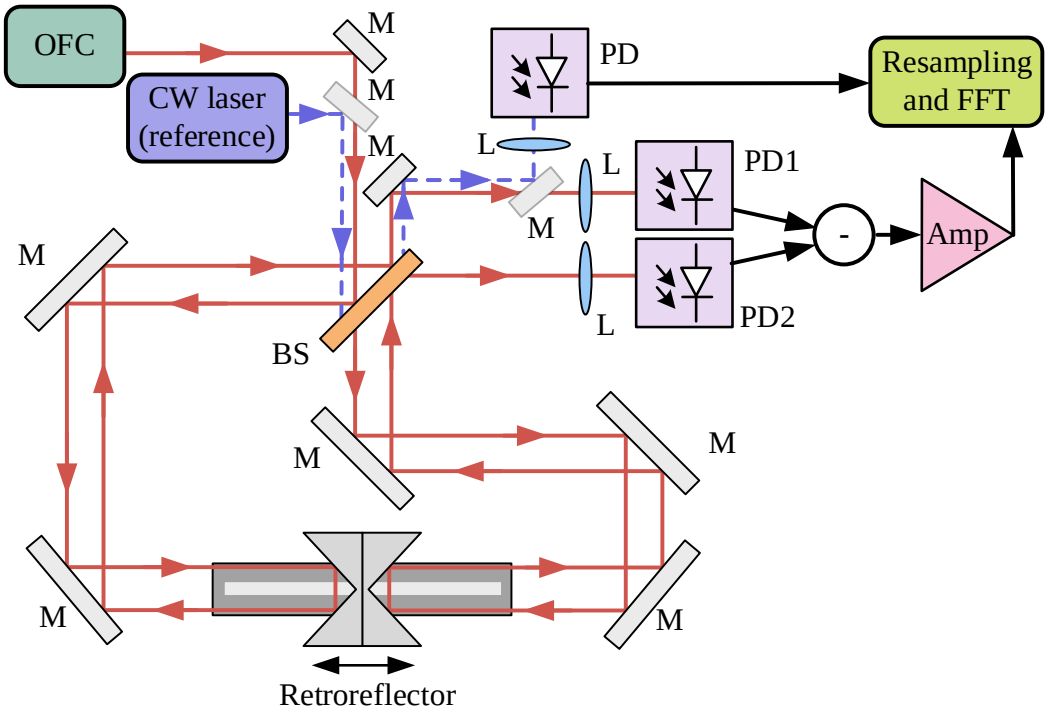

Fig. 3.14. Fourier transform spectrometer. OFC, optical frequency comb; M, mirror; BS, beamsplitter; L, lens; PD, photodetector; Amp, amplifier; FFT, fast Fourier transform. The propagation of the OFC beam is shown in a solid red line. The propagation of the reference beam is shown in a dashed blue line. After the BS, it travels the same path as the OFC beam, but it is not presented for better visibility.

A reference laser beam with a wavelength λ = 1551 nm (Alcatel, 1905 LMI) propagates parallel, but with diagonal offset, to the OFC to calculate the correct frequency scale of the Fourier spectrum. The sinusoidal interferogram from the CW laser with a known and stable

wavelength serves as a calibration signal to determine OPD_{max}, and it also can be used to resample the OFC interferogram at equal *OPD* steps, which is required for the FFT. That is why the beamsplitter used is a custom-made one, with a check pattern to transmit and reflect both near-IR and mid-IR beams. Two parts of the BS were optimized for the reference beam at 1.55 μm, and the remaining two for the OFC beam from the 2-5.5 μm range. Only one of the reference output beams is measured with an InGaAs detector (Thorlabs, PDA10CS2).

Both the reference and the OFC interferograms are acquired with a digital oscilloscope (Digilent, Analog Discovery 2) and a home-written Python program. The *OPD* is adjusted according to the measurements. Additional data processing is conducted in the MATLAB environment and is presented in Section 5.3.1, which describes the experiment.

Chapter 4.

Gain-managed nonlinear amplification

4.1. Introduction

This Chapter presents an analysis of GMN amplification of Yb-doped fiber laser. The study emphasized the relation between the repetition rate of the seed source and output characteristics, as reducing the repetition rate is a universal strategy for increasing the pulse energy. In this approach, there is a higher risk of accumulating amplified spontaneous emission between consecutive pulses, and it adds thermal load on the fiber upon reabsorption. Hence, this work aimed to investigate the impact of two different lasers with low and high repetition rates to seed the GMN amplifier. Parameters like output spectra and pulse duration after the amplifier and after the compressor were compared, together with spectral and temporal phases, average power, and relative intensity noise measurements. The effect of fiber temperature change on the output spectra at different pump power levels was studied, proving that its effect on the gain profile of the active fiber cannot be excluded. In collaboration with the group from the Royal Institute of Technology in Sweden, numerical simulations of the amplification process were conducted, which confirmed GMN pulse evolutions and showed an excellent agreement for the high-repetition-rate laser and low pump powers with the low-repetition-rate laser. To the best of my knowledge, the study presented the shortest pulse duration reported to date for a GMN amplifier. The results of this work were published in [71]. Moreover, the compressed pulses obtained from the high-repetition-rate source are highly suitable for seeding nonlinear processes like an OPO or DFG to obtain a mid-IR OFC.

4.2. GMN amplifier scheme

The GMN technique uses three main parts: the seed source, the amplifier with a relatively long section of an active fiber, and the compressor. The experimental setup used for the research is depicted in Fig. 4.1. It was composed of polarization-maintaining fibers and components. At the beginning of the amplifier, there was a 90/10% tap coupler (Advanced Fiber Resources) for power monitoring. Then, the pump light out of a laser diode was delivered to the amplifier by a pump-signal combiner (Advanced Fiber Resources). An active fiber used in the GMN amplifier was a double-clad Yb-doped fiber with a 10-μm core diameter (Nufern, PLMA-YDF-10/125-VIII). The length of the active fiber was selected according to the wavelength of the pump diode, which is explained further in Section 4.3. During the first attempt, it was 8 m for the 918-nm diode (II-VI Incorporated, BMU30_915_01_R), and during

the second, it was 3.4 m for the 976-nm diode (BWT, K976A02RN-9.000 W). The final compressor, with 75% of transmission overall, consisted of two transmission gratings with 1000 lines/mm and was built in the Treacy scheme [189]. In this structure, two gratings are placed parallel to each other, and the distance between them translates into the magnitude of the induced dispersion. Treacy compressors are used to introduce a negative chirp (anomalous dispersion) or to shorten the stretched pulses.

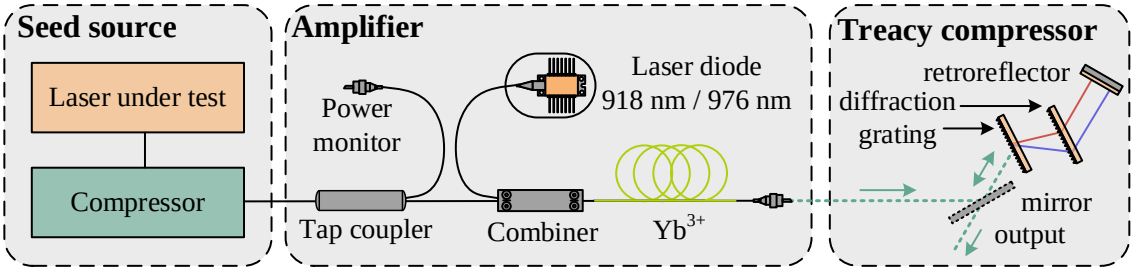

Fig. 4.1. Schematic of the gain-managed nonlinear amplifier. It consists of three parts: the seed source, the amplifier, and the compressor.

The characterization of the output pulses was performed with the following equipment: an optical spectrum analyzer (OSA, Yokogawa, AQ6370B), an interferometric autocorrelator (AC, APE, pulseCheck), a second-harmonic frequency-resolved optical gating system (FROG, Mesa Photonics, FSUltra2), and an optical power meter (Thorlabs, PM400 with an S405C thermal head). Additional noise properties measurements were realized with a low-noise photodetector (Thorlabs, PDA10D2) and an oscilloscope (Rohde-Schwarz, RTA4000). The procedure for relative intensity noise (RIN) measurements was similar to the one presented in the literature [190] and is described in Section 4.4.3.

As mentioned before, the research aimed to study the impact of different repetition rates of the seed sources on output pulses. Two different lasers were used to investigate this topic. Both sources emitted chirped pulses, which were first compressed before the amplification. The dispersion of the source compressor was adjusted to achieve the shortest pulse duration for the highest pump power after the second compressor in the setup.

The first seed source was a commercially available femtosecond laser (Menlo Systems, Orange) based on an Yb-doped fiber laser, where the nonlinear amplifying loop mirror (NALM) was used as a saturable absorber. The laser delivered chirped pulses with a pulse duration of 10 ps, central wavelength of 1038 nm, and 20 nm FWHM. The average power out of the laser was 140 mW, and the repetition rate was 125 MHz. The pulse duration after the compressor for the high-repetition-rate source equaled 226 fs with an average power of 55 mW. Optical spectrum and FROG-retrieved temporal intensity and phase recorded after the compressor are presented in Fig. 4.2.

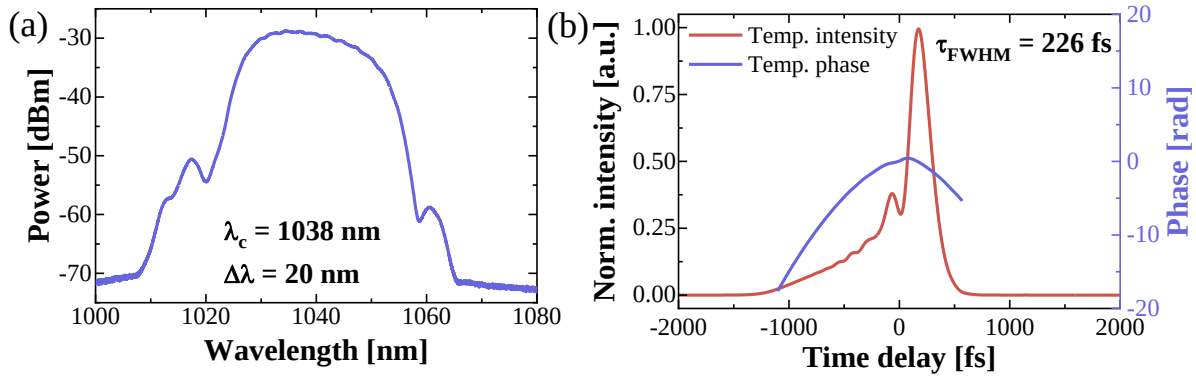

Fig. 4.2. Characterization of high-repetition-rate seed source: (a) optical spectrum with a central wavelength (λ_c) and an FWHM ($\Delta\lambda$) and (b) FROG-retrieved temporal intensity (solid red line), temporal phase (solid blue line) and a pulse duration (τ_{FWHM}).

The second seed laser had a repetition rate of 30.44 MHz and was a home-built Yb-doped fiber laser. The mode-locking mechanism was a SESAM, and a similar realization can be found in the literature [191,192]. The laser was followed by an Yb-doped fiber pre-amplifier, which boosted the average power to 125 mW. The 12-ps-long pulses were centered at 1031 nm with an optical FWHM of 11 nm. The compressed pulses had a duration of 268 fs with 40 mW of average power. The characterization of the low-repetition-rate source is depicted in Fig. 4.3.

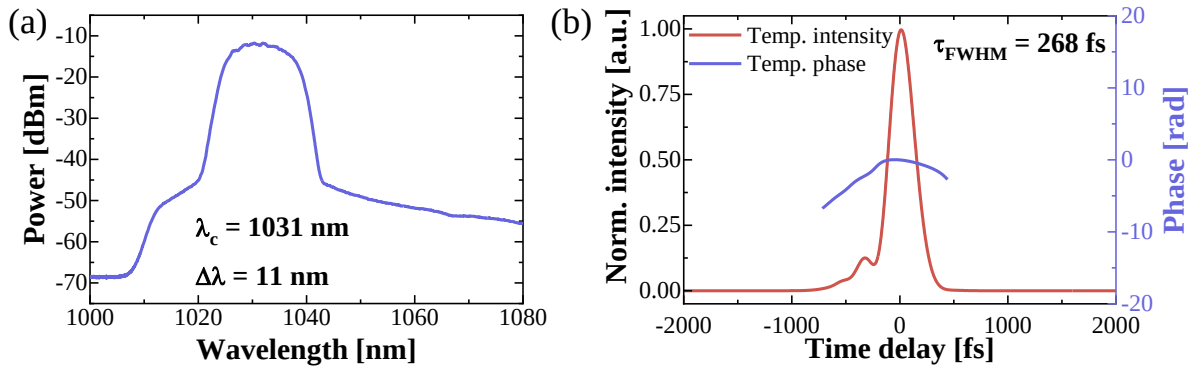

Fig. 4.3. Characterization of low-repetition-rate seed source: (a) optical spectrum with a central wavelength (λ_c) and an FWHM ($\Delta\lambda$) and (b) FROG-retrieved temporal intensity (solid red line), temporal phase (solid blue line) and a pulse duration (τ_{FWHM}).

4.3. Pumping the GMN amplifier with a 918-nm diode laser

Yb-doped fiber amplifiers offer a broad gain bandwidth and a wide range of possible pump wavelengths. The cross-sections for absorption and emission for Yb-doped germanium silicate glass fiber are presented in Fig. 4.4, but it should be noted that the host glass composition influences, to some extent, the details of absorption and emission spectra [193,194].

There are different choices for pump wavelengths, but two of them are obvious: the narrow absorption peak at 975 nm and the broader and weaker peak at 910 nm. Still, longer wavelengths, such as 1047 or 1064 nm, where a Neodymium laser can be considered as a pump, or even shorter wavelengths, like 860 nm or less, can be used if the deciding factor is the availability of the diode laser. It is possible to achieve gain either on the 975-nm emission peak or across a range of wavelengths on the broader peak centered at 1030 nm. However, it is crucial to remember that gain is solely available at wavelengths longer than the pump wavelength.

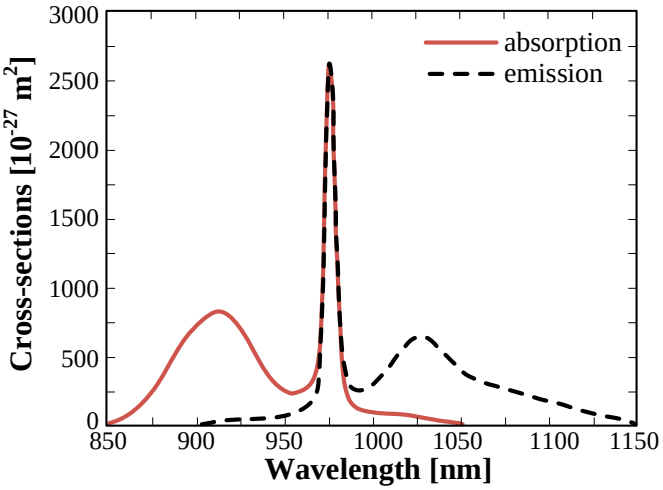

Fig. 4.4. Absorption and emission cross-sections for Yb in germanosilicate glass. [195]

A strong 910-nm pump results in 97% upper-state population [195], producing almost maximum gain per unit length. However, this leads to a very strong gain at 975 nm, which results in amplified spontaneous emission (ASE) around 975 nm, which limits the gain at longer wavelengths. In principle, if the ASE is reabsorbed, it can contribute to the signal gain in sections with lower population inversion. For ASE propagating in the direction of the pump, it can be achieved by using a sufficiently long fiber. Nevertheless, using a 975-nm pump is the most direct solution to avoid the problem with 975-nm-related ASE. At this wavelength, the absorption and emission cross-sections are equal, resulting in a maximum of 50% upper-state population for strong pumping [195]. The amplification process is now limited only by ASE around 1030 nm, which could be a severe limitation of the gain achievable at longer wavelengths like 1080 nm. ASE filtering is necessary for achieving higher gains at longer wavelengths [195].

As shown in Fig. 4.4, absorption is much stronger at around 975 nm than around 910 nm, so selecting the active fiber's appropriate length is essential when choosing a pump wavelength. Thus, the fiber length was more than twice as short for the 976-nm pump than for the 918-nm pump. Also, for numerical simulations of the amplification process, it was crucial to measure all the accurate lengths of the fiber before and after the amplifier, as the pulse after the first compressor is still influenced by the propagation through the pump-signal combiner before it reaches the active fiber. The exact fiber lengths for the first amplifier pumped by a 918-nm diode laser are presented in Fig. 4.5.

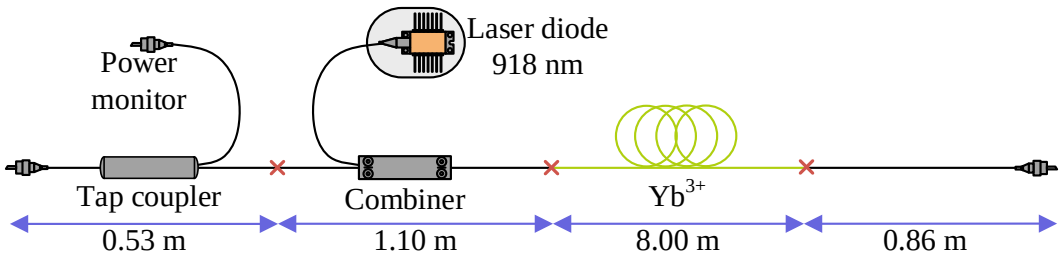

Fig. 4.5. Exact fiber lengths of the GMN amplifier pumped by 918-nm diode laser. Red crosses illustrate the location of the splices.

In this amplifier setup, the GMN regime can already be observed for small pumping powers. The spectra obtained for the high-repetition-rate oscillator are presented in Fig. 4.6(a),

alongside pump power and average output power. Fig. 4.6(b) shows FROG-retrieved temporal intensities with transform-limited (TL) pulses and temporal phase. All the results were acquired after the final compressor. With increasing pump power, the spectrum is shifted towards longer wavelengths and gets broader, leading to a shorter pulse duration following the transform limit. The grating separation in the final compressor was fine-tuned for each pump power to achieve the shortest pulse duration. The simulations at this point did not match the experimental results as not all the parameters used for numerical analysis were known at that time. This is due to the confidentiality of some fiber specifications, and a part of the data is not measurable in the laboratory. Despite this, initial experimental results that were obtained were promising and pushed for further analysis of the GMN amplification.

For the maximum launched pump power, equaled 7.23 W, the pulse duration was the shortest. The spectrum obtained for a high-repetition-rate laser had a central wavelength of 1069 nm and an FWHM of 39 nm. The pulse duration was 80 fs (according to the FROG-retrieved measurement), while the calculated TL duration was 63 fs. The average output power was equal to 2.30 W, which corresponds to the pulse energy of 18.4 nJ and a peak power of 230 kW.

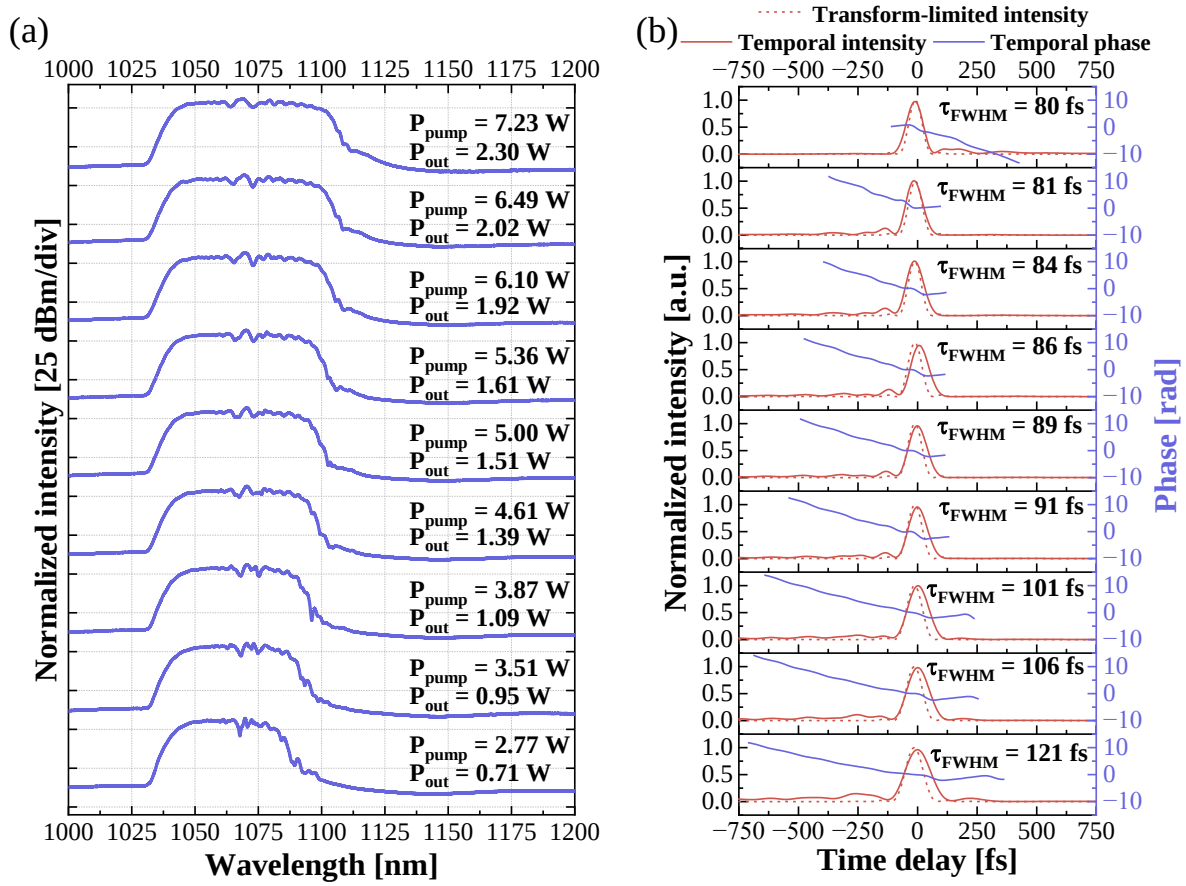

Fig. 4.6. Characterization of the amplified pulses in the GMN regime while pumping with a 918-nm diode laser for the high-repetition-rate seed source: (a) spectra measured with the OSA (solid blue line) at the output of the compressor with corresponding pump power (P_{pump}) and average output power (P_{out}); (b) FROG-retrieved temporal intensity (solid red line) of the compressed pulses with the temporal phase (solid blue line), TL intensity (dashed red line) and corresponding pulse duration (τ_{FWHM}).

The spectra and FROG-retrieved intensities of the pulses obtained for the amplification of the low-repetition-rate laser source are depicted in Fig. 4.7. In this case, optical spectra are

much broader than for the high-repetition-rate source, which is then reflected in the shorter pulse duration. The spectra in Fig. 4.7(a) are also characterized by extensive Raman contribution. For the low-repetition-rate source, the shortest pulse duration was not observed for the highest pump power but for the launched pump power of 5.00 W. The duration of this pulse was 47 fs (based on FROG-retrieved measurement), while the calculated TL pulse was 41 fs. The central wavelength for the spectrum of this pulse was 1089 nm, with an FWHM of 75 nm. The average output power was equal to 1.56 W, corresponding to the pulse energy of 51.2 nJ and a peak power of 1.09 MW. The longer pulse duration (62 fs) for the highest pump might correlate with the thermal effects occurring in the active fiber, further discussed in Section 4.4.2, or the growing contribution of the Raman effect. For higher pump powers (above 5.36 W), acquired optical spectra and pulses were deformed and did not compress properly, which may also be related to the same cause.

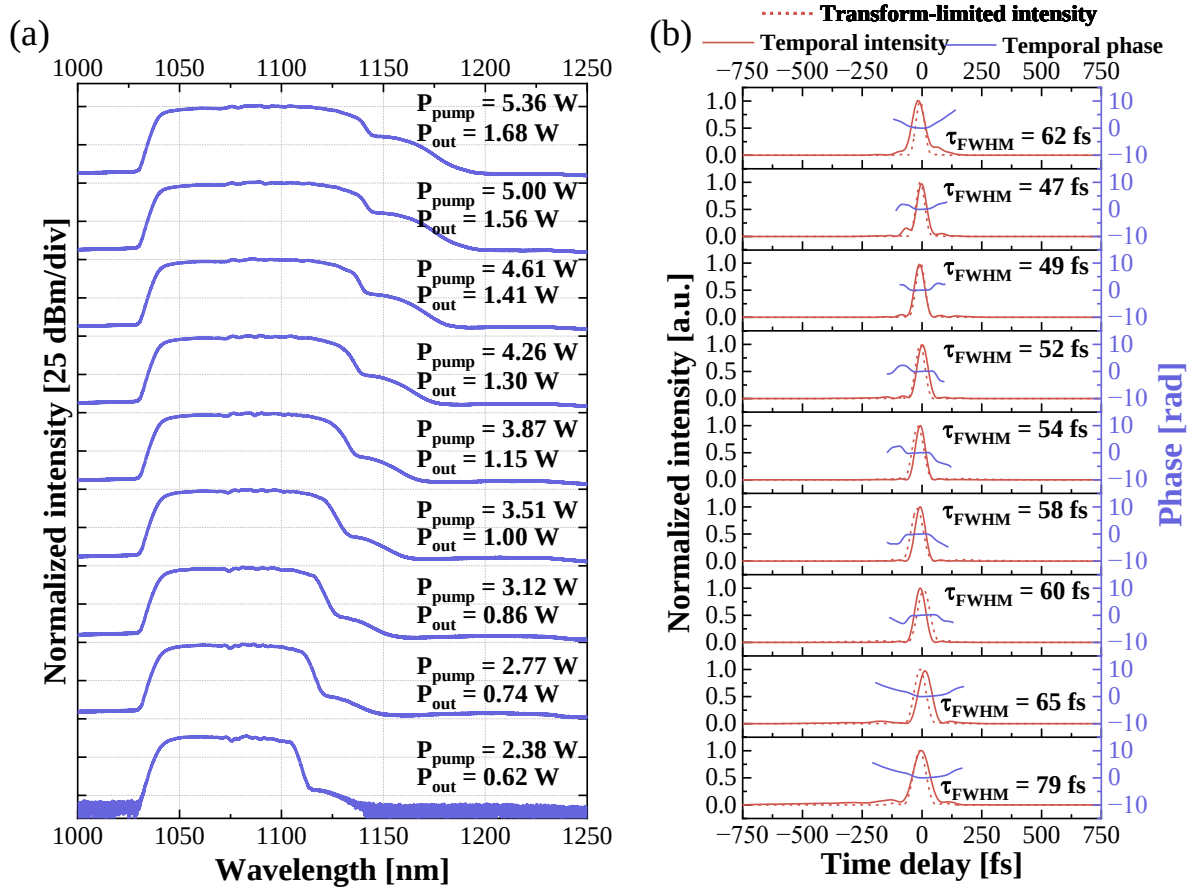

Fig. 4.7. Characterization of the amplified pulses in the GMN regime while pumping with a 918-nm diode laser for the low-repetition-rate seed source: (a) spectra measured with the OSA (solid blue line) at the output of the compressor with corresponding pump power (P_{pump}) and average output power (P_{out}); (b) FROG-retrieved temporal intensity (solid red line) of the compressed pulses with the temporal phase (solid blue line), TL intensity (dashed red line) and corresponding pulse duration (τ_{FWHM}).

4.4. Pumping the GMN amplifier with a 976-nm diode laser

In the second configuration of the GMN amplifier, the 976-nm diode laser was used for pumping. As established in Section 4.3, Yb-doped fiber has stronger absorption at this wavelength, thus, the length of the active fiber needed to obtain similar results was much shorter than in the first configuration of the amplifier. Moreover, all the lengths of the passive fibers

were reduced to the necessary minimum to avoid any additional impact of the dispersion on the laser pulses before and after amplification. Fig. 4.8 presents the exact fiber lengths of the second amplifier pumped by a 976-nm-long laser diode.

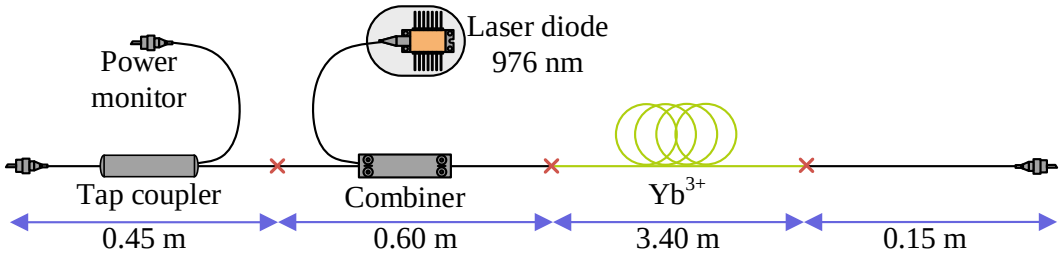

Fig. 4.8. Exact fiber lengths of the GMN amplifier pumped by 976-nm diode laser. Red crosses illustrate the location of the splices.

Simulations were run for the segment consisting of the active fiber and the subsequent passive fiber (PM980XP, Nufern) and were initiated by a reference FROG-trace, measured before the active fiber. The numerical model was created by Robert Lindberg from KTH Royal Institute of Technology in Stockholm as a part of a collaboration, and it was based on his previous work [196]. The background noise level was added to function as a seed for the Raman scattering process. The free parameters were pump-dopant overlap to get comparable power scaling to the experimental one and the nonlinear refractive index to match the simulated spectral broadening to the experimental results obtained for the high-repetition-rate seed source. For the propagation in the passive fiber at the output of the amplifier, the fourth-order Runge-Kutta in the interaction picture technique [197] was used together with an adaptive step size [198]. The details of the numerical simulations can be found in the associated publication [71].

4.4.1. High-repetition-rate oscillator

The first seed source used in the amplification process was a high-repetition-rate laser. Spectra recorded out of the amplifier (without the final compression stage) are shown in Fig. 4.9(a), together with the simulated spectra for nine different launched pump powers. Next to every plot, there is a corresponding pump power, and an average output power is provided. There is a particularly good agreement between the experimental and simulated spectra. However, it is observed that the measured spectra are slightly shifted towards longer wavelengths at higher power levels compared to the corresponding simulated traces. Nonetheless, the spectral widths remain comparable. In addition, it may be noted that for higher pump powers, the amplified spectra are extended beyond the conventional Yb-doped fiber gain window, and despite low absorption of the active fiber at longer wavelengths, the intensity at the right side of the spectrum does not differ from the one at shorter wavelengths.

In Fig. 4.9(b), temporal intensities were measured via FROG after the pulses were compressed in a diffraction grating compressor. The separation between the gratings was adjusted for each pump power to obtain the shortest pulse duration. Apart from temporal intensities in Fig. 4.9(b), there are temporal phases and TL intensities calculated from the magnitude of the FROG-retrieved spectra for different pump powers. It is evident that the pulse duration decreases as the pump power increases, and the phases across the majority of the pulse

are relatively flat. The results proved that generating clean, nearly TL pulses for higher pump powers is possible.

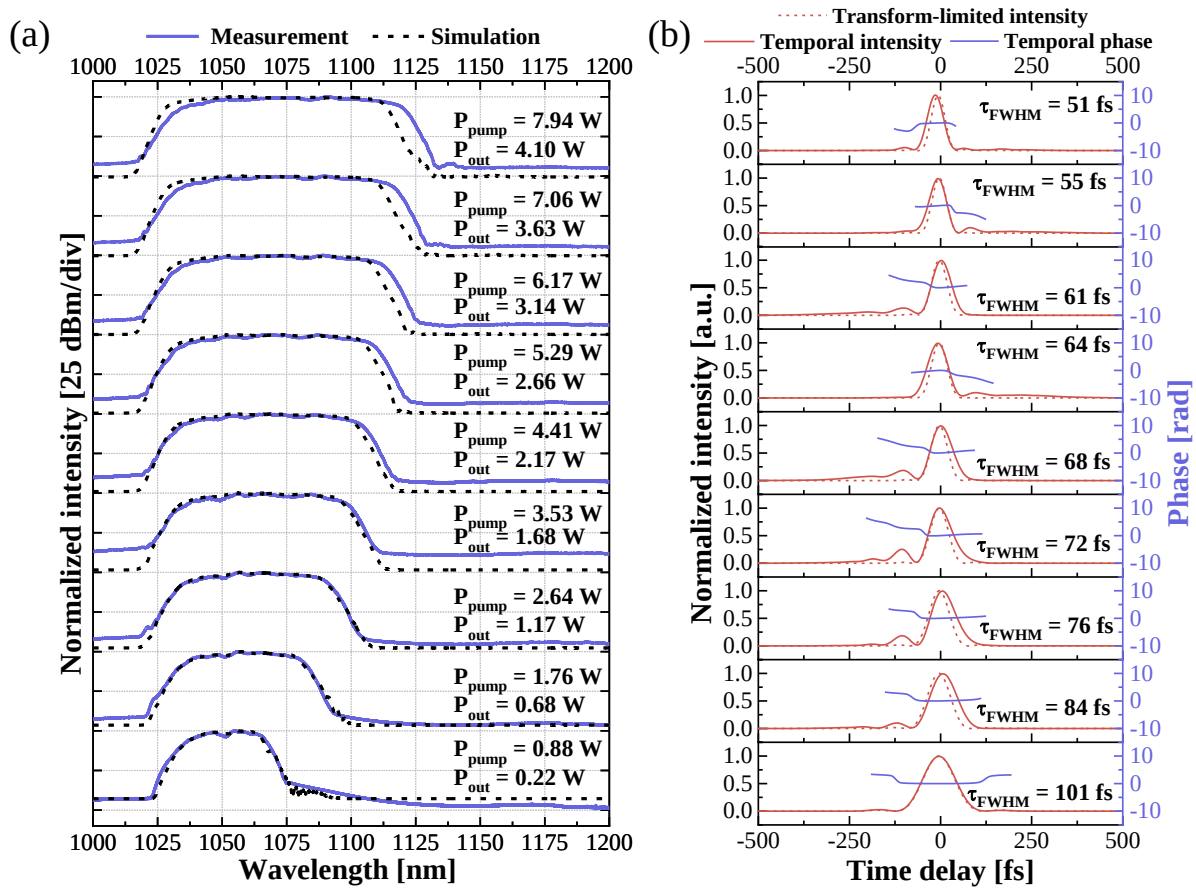

Fig. 4.9. Characterization of the amplified pulses in the GMN regime while pumping with a 976-nm diode laser for the high-repetition-rate seed source: (a) comparison of the spectra measured with the OSA (solid blue line) at the output of the amplifier and simulated traces (dashed black line) with corresponding pump power (P_{pump}) and average output power (P_{out}); (b) FROG-retrieved temporal intensity (solid red line) of the compressed pulses with the temporal phase (solid blue line), TL intensity (dashed red line) and corresponding pulse duration (τ_{FWHM}).

At the highest pump power, the temporal and spectral evolution of the pulse in the amplifier and the passive fiber at the output was investigated by numerical analysis. The result can be observed in Fig. 4.10. In the first 30 cm, the spectrum mainly experiences a spectral shift. Next, the spectrum broadens symmetrically till 75 cm into the amplifier, then it starts a gradual shift towards longer wavelengths while still broadening due to SPM. This shift comes from reduced inversion levels down the fiber, which pushes the gain towards longer wavelengths, indicative of the GMN regime [9,72]. Therefore, the short-wavelength components initially appearing are progressively absorbed until about 1.1 m. In the temporal evolution, these spectral features can be observed as a weak part towards the positive time values. It also fades away at the same distance. Overall temporal evolution of the pulse is indicated by a broadening curved trajectory and becomes rather monotonic after about 1.2 m. This point marks the position where the input pulse is reshaped into a GMN pulse. For lower pump powers, the pulse evolution follows the same trend, but the spectral broadening happens at a further distance from the beginning of the amplifier, which influences the width of the output spectra, they are narrower.

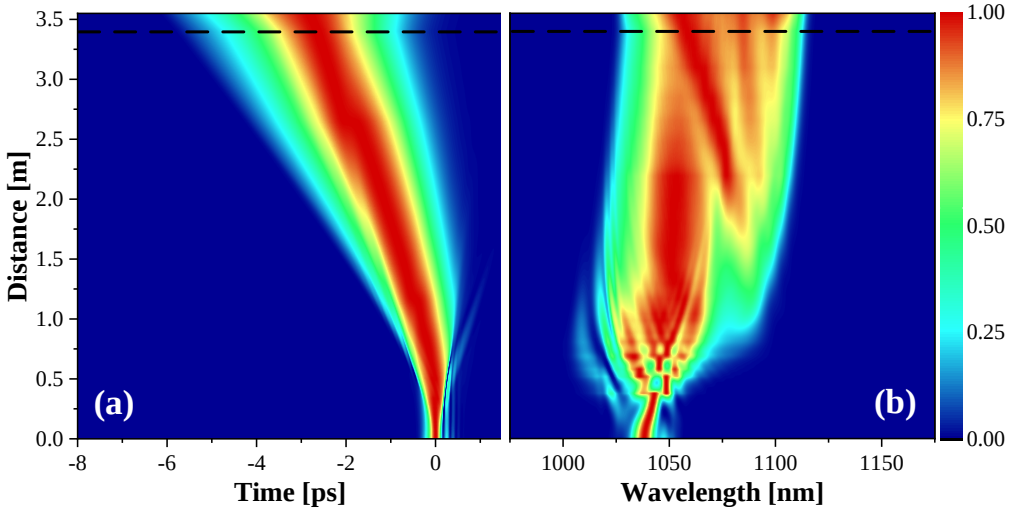

Fig. 4.10. Simulation of pulse evolution at the highest pump for the high-repetition-rate oscillator while pumping with a 976-nm diode laser. (a) temporal and (b) spectral intensities in the amplifier. The dashed black line shows the splice between the active and the passive fiber.

Characterization of the shortest pulse obtained for the high-repetition-rate laser source is presented in Fig. 4.11 and Fig. 4.12. It was obtained for the highest launched pump power of 7.94 W. The pulse duration was 51 fs (according to the FROG-retrieved measurement), with a calculated TL duration of 43 fs. The average output power was equal to 2.85 W, which corresponds to the pulse energy of 22.8 nJ and peak power of 420 kW. As for the spectrum, it had a central wavelength of 1078 nm and an FWHM of 67 nm. The characteristic consists of the optical spectrum measured by the OSA, an autocorrelation trace, and results from FROG: spectral and temporal pulse with phase profiles, measured and retrieved FROG traces.

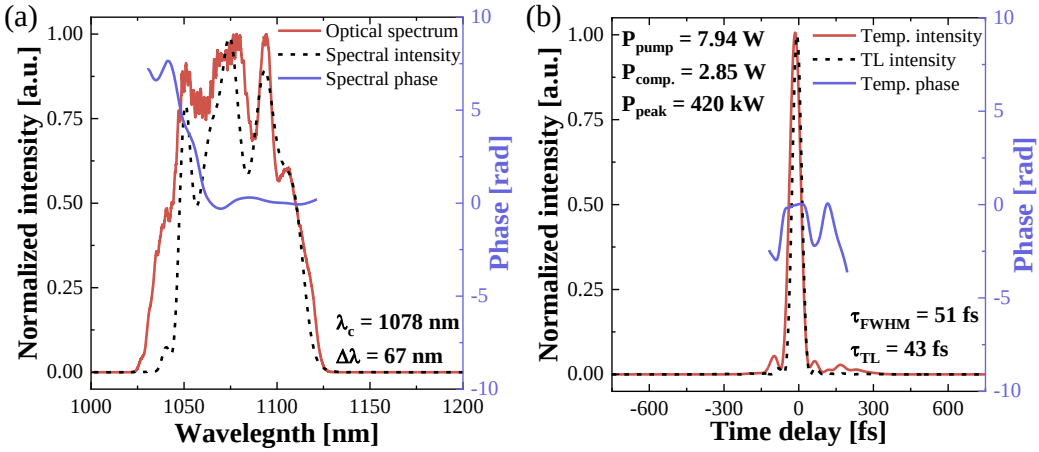

Fig. 4.11. Characterization of the shortest compressed pulse obtained from the GMN amplifier seeded with the high-repetition-rate laser while pumping with a 976-nm diode laser: (a) optical spectrum measured by the OSA (solid red line), the FROG-retrieved spectral profile (dashed black line) with spectral phase (solid blue line), a central wavelength (λ_c) and an FWHM ($\Delta\lambda$) (b) FROG-retrieved temporal intensity (solid red line) of the compressed pulse with a pulse duration (τ_{FWHM}), temporal phase (solid blue line), TL intensity profile (dashed black line) and its duration (τ_{TL}), as well as a pump power (P_{pump}), an output compressed pulse power (P_{comp}) and corresponding peak power (P_{peak}).

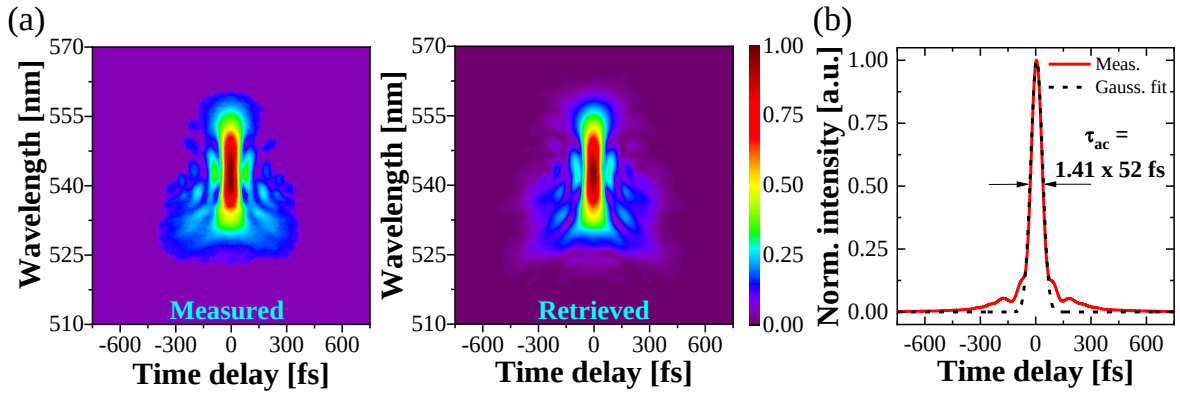

Fig. 4.12. Characterization of the shortest compressed pulse obtained from the GMN amplifier seeded with the high-repetition-rate laser while pumping with a 976-nm diode laser: (a) measured and retrieved FROG spectrograms, (b) autocorrelation trace (solid red line) with its pulse duration (τ_{ac}) and Gaussian fit (dashed black line).

4.4.2. Low-repetition rate oscillator

For the low-repetition-rate laser source, the evolution of the amplified spectrum over different pump powers is shown in Fig. 4.13(a), with corresponding pump powers and average output powers at the output of the amplifier. Next to it, in Fig. 4.13(b), there are temporal intensities of the compressed pulses with calculated TL intensities and temporal phases. The relatively flat temporal phases over the central part of the pulse once again prove the pulses to be close to the transform limit. The first difference between spectra obtained for low and high-repetition-rate sources is their width: it is much broader for the low-repetition-rate laser, thus, it supports shorter pulse durations. At higher pump powers, which are linked to higher output powers, the simulated and measured spectral shapes start notably differing from each other. It is important to note that the high-repetition-rate source had a maximum pulse energy of 33 nJ, which is already surpassed by the low-repetition-rate source at a pump power of 2.64 W. The experimental results are still consistent with simulations at this point. However, for pump powers exceeding 4.41 W, the measured shorter wavelength edge is shifted towards longer wavelengths more than the simulated correlatives.

The input pulse remains the same for all pump power levels, so it cannot be related to a shorter seed pulse, which would start shifting at an earlier point in the fiber since this would result in deviations at all power levels. It seems that the effect is caused by the experimental gain profile, which deviates from the simulated one at higher pump powers and leads to miscalculation of the short-wavelength absorption. It is possible that the fiber is experiencing an increase in thermal load, which was not taken into account during the simulations. This is due to the increased absorption of short-wavelength light for greater spectral broadening and a larger amount of spontaneously emitted light that gets absorbed as the pump level increases. Both of these mechanisms function as short-wavelength pumps for longer-wavelength emission, leading to decreased photon energies. The difference in energy is dissipated as heat, leading to an increased thermal load in the fiber. The effect of changing the effective absorption and emission cross-sections of solid-state lasers due to temperature is described by the McCumber relation [199].

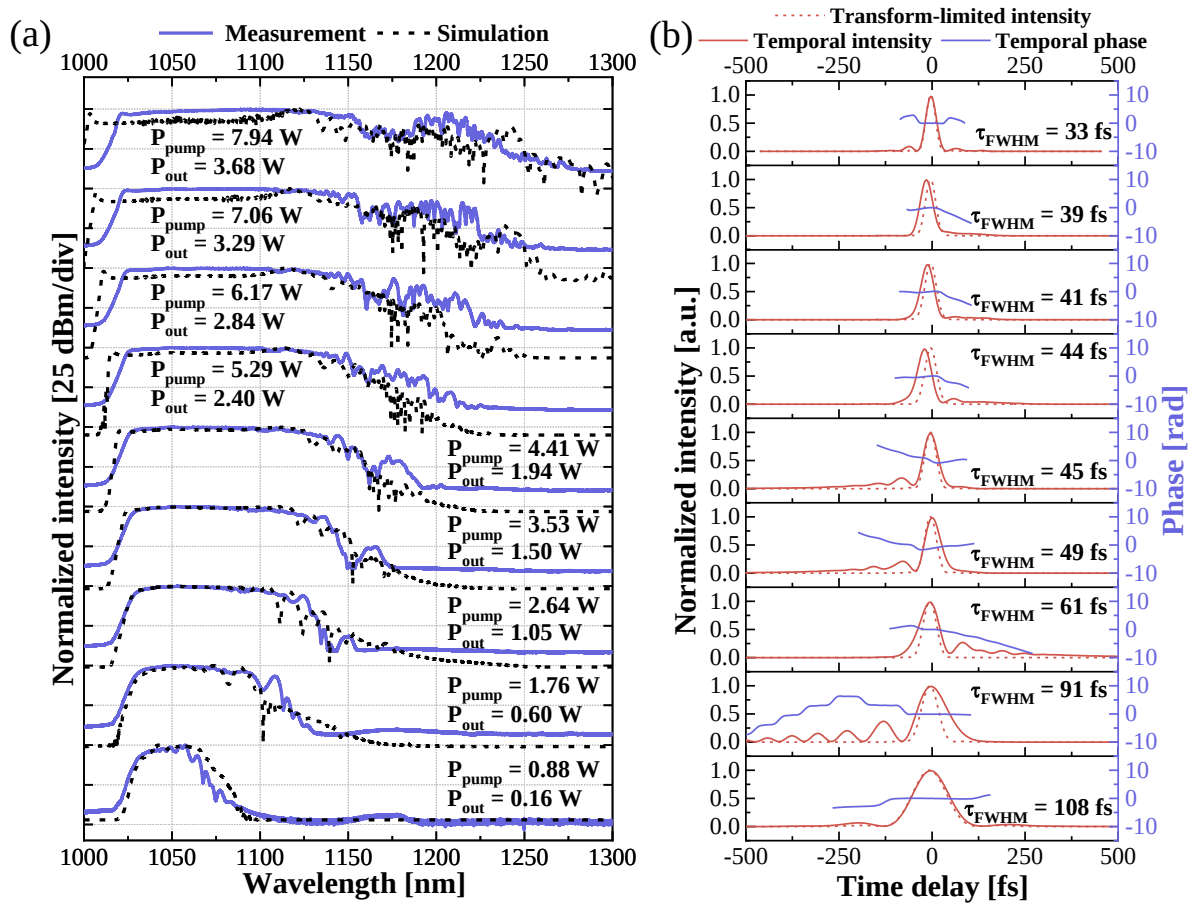

Fig. 4.13. Characterization of the amplified pulses in the GMN regime while pumping with a 976-nm diode laser for the low-repetition-rate seed source: (a) comparison of the spectra measured with the OSA (solid blue line) at the output of the amplifier and simulated traces (dashed black line) with corresponding pump power (P_{pump}) and average output power (P_{out}); (b) FROG-retrieved temporal intensity (solid red line) of the compressed pulses with the temporal phase (solid blue line), TL intensity (dashed red line) and corresponding pulse duration (τ_{FWHM}).

The simulations were first carried out to illustrate the thermal impact on gain profiles [71]. As not all the necessary fiber parameters were available to estimate the amount of heat load in the active fiber, an experiment was conducted, as the fiber's ability to dissipate heat also influences the temperature distribution. The fiber was mounted on a water-cooled block, and the output spectra were observed at different pump powers and various block temperatures. Fig. 4.14 presents the results of the experiment. For this study, two parameters were defined: short- and long-wavelength edge of the spectrum. Both are stated as points with a spectral intensity of 1/10 of the maximum intensity on the left and right sides of the spectrum, respectively. The bottom part of the plot presents how the location of the short-wavelength edge changes. It can be noted that as the temperature of the cooling block increased, the short-wavelength edge shifted towards longer wavelengths. This also leads to decreased heat dissipation from the fiber, resulting in higher core temperatures. The top panel shows that the long-wavelength edge is not affected that much. It cannot be ruled out that the discrepancy between the measured and simulated results at higher pump levels was caused by the impact of the thermal load on the gain profile.

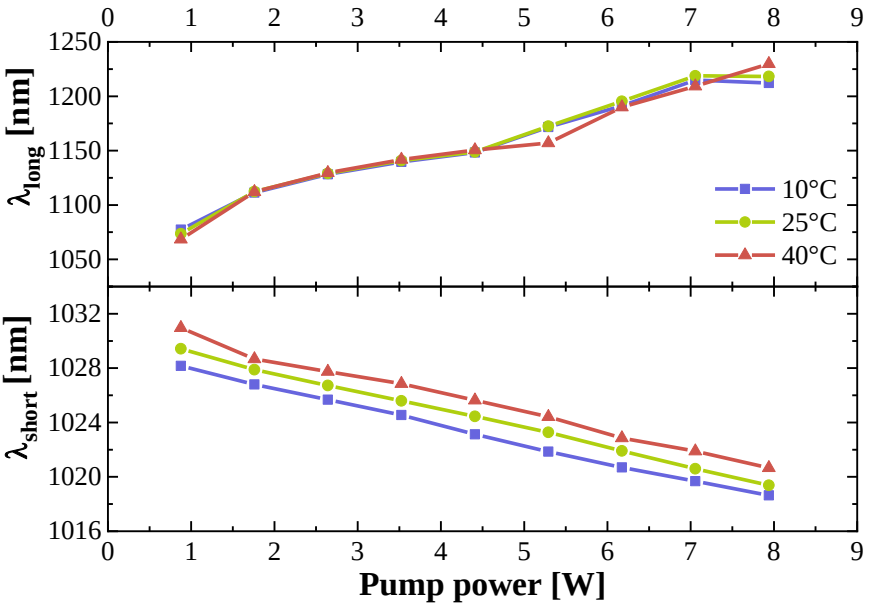

Fig. 4.14. Location of spectral edges in the optical spectrum of amplified pulses in GMN regime, where the intensity equals 1/10 of the maximal intensity for three different temperatures of the cooling plate: (a) long-wavelength edge, (b) short-wavelength edge.

Once again, looking at Fig. 4.13(a), it can be noted that for pump powers exceeding 4.4 W, the simulated spectra appear like asymmetric SPM spectra. In contrast, the experimental ones have similar shapes to the high-repetition-rate source case. In the experiments, the spectra likely undergo a similar spectral evolution with a shifting spectral center of mass. This shift allows the center part of the spectrum to maintain a significant amount of energy, resulting in shapes associated with GMN amplification [9]. However, both experimental and simulated spectra have a non-negligible Raman contribution, which could potentially degrade the pulse chirp. Yet, the simulated pulse evolutions demonstrate that the Raman contributions mainly create secondary pulse structures that are distinct from the main temporal pulse shape. In such circumstances, the Raman part will not limit the compression of the main pulse but instead appear as a low-intensity background. The experimentally observed Raman contributions are believed to form similar secondary structures, as evident in Fig. 4.13(b), with pulses close to the transform limit and relatively flat phases.

As it was established, the simulations and experimental data differ for higher pump powers, so the simulated pulse evolution presented in Fig. 4.15 was performed for a pump level of 4.4 W, where the simulations are still in good agreement with the experimental data. As in the case of a high-repetition-rate source, the initial evolution is characterized by temporal reshaping. In this case, it is connected to a noticeable SPM peak that develops from the middle portion of the pulse's spectral lobe and gradually shifts towards longer wavelengths. After approximately 1.5 m, the spectrum becomes more balanced as the gain for shorter wavelengths begins to catch up. At the same time, the energy contained in the peak starts to decrease as the Raman contribution becomes stronger. This is also the point at which the temporal broadening towards both pulse tails becomes more uniform, indicating that the pulse has reached the GMN regime.

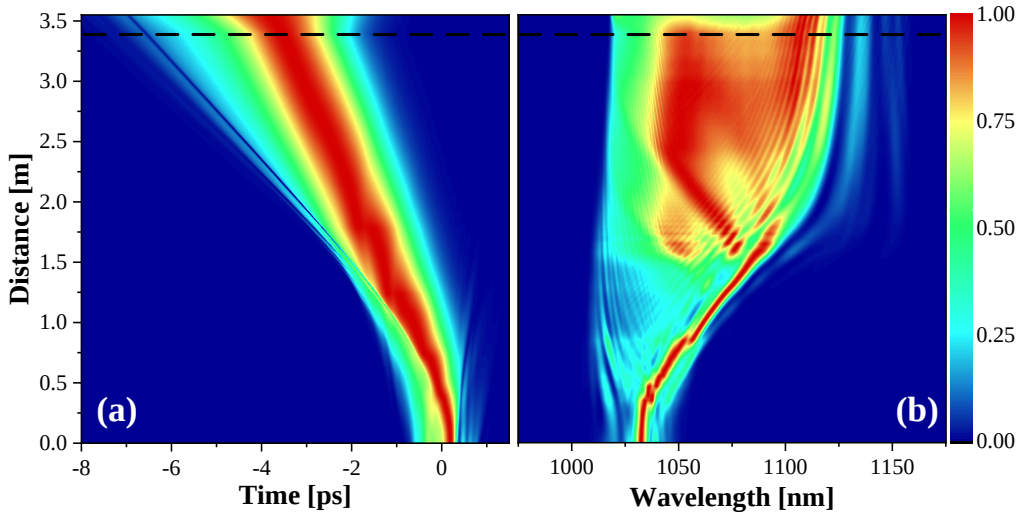

Fig. 4.15. Simulation of pulse evolution at the 4.4 W of pump power for the low-repetition-rate oscillator while pumping with a 976-nm diode laser. (a) temporal and (b) spectral intensities in the amplifier. The dashed black line shows the splice between the active and the passive fiber.

For the low-repetition-rate source, the shortest pulse obtained was 33 fs with an average power of 2.45 W, corresponding to the energy of 80.5 nJ and peak power of 2.29 MW. The TL pulse duration is only 4 fs longer than the one obtained during the experiment. The pulse spectrum had a central wavelength of 1100 nm and an FWHM of 121 nm. The measured parameters for this pulse can be found in Fig. 4.16 and Fig. 4.17, which consist of spectral and temporal pulse shapes and phase profiles, measured and retrieved FROG traces, spectrum recorded by OSA, and an AC trace. It is worth noting that the retrieved pulse spectrum from FROG is narrower than the spectrum measured by OSA and does not include the Raman contribution. It is likely that the Raman component cannot compress properly and appears as a low-intensity dispersive background, which will not be detectable by FROG after the process of second-harmonic generation.

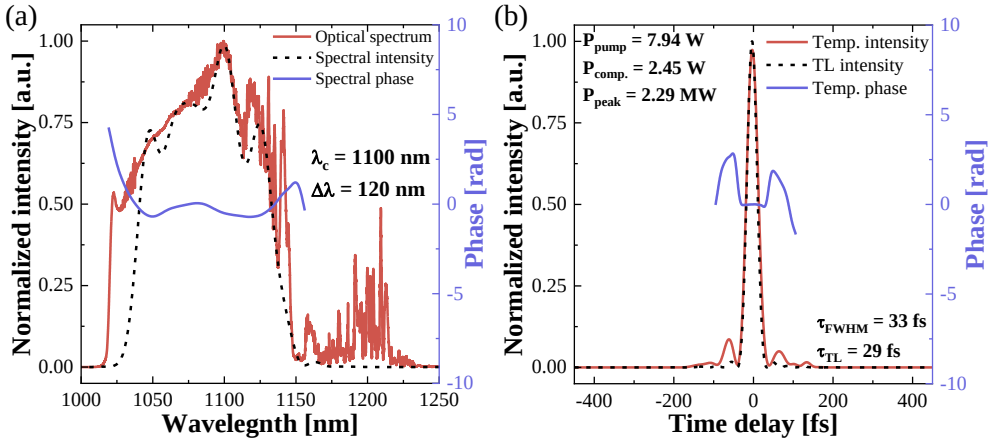

Fig. 4.16. Characterization of the shortest compressed pulse obtained from the GMN amplifier seeded with the low-repetition-rate laser while pumping with 976-nm diode laser: (a) optical spectrum measured by the OSA (solid red line), the FROG-retrieved spectral profile (dashed black line) with spectral phase (solid blue line), a central wavelength (λ_c) and an FWHM ($\Delta\lambda$) (b) FROG-retrieved temporal intensity (solid red line) of the compressed pulse with a pulse duration (τ_{FWHM}), temporal phase (solid blue line), TL intensity profile (dashed black line) and its duration (τ_{TL}), as well as a pump power (P_{pump}), an output compressed pulse power (P_{comp}) and corresponding peak power (P_{peak}).

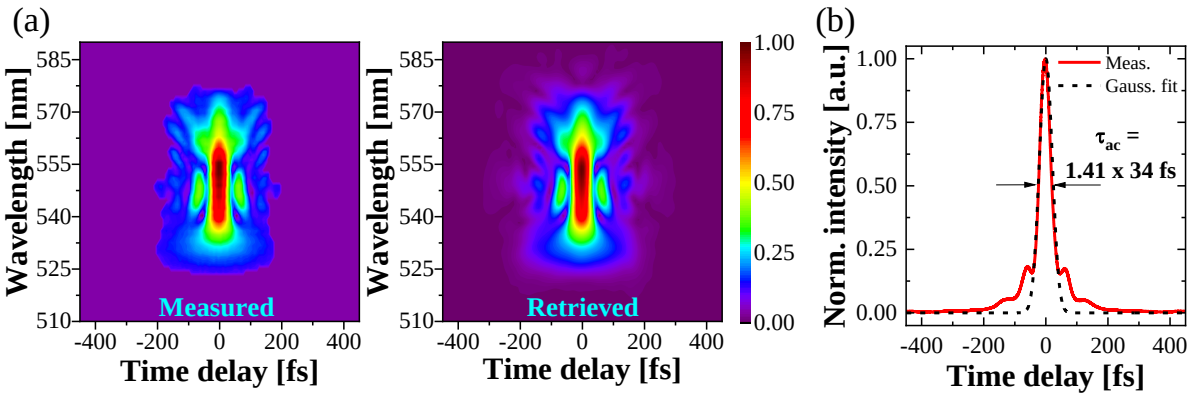

Fig. 4.17. Characterization of the shortest compressed pulse obtained from the GMN amplifier seeded with the low-repetition-rate laser while pumping with 976-nm diode laser: (a) measured and retrieved FROG spectrograms, (b) autocorrelation trace (solid red line) with its pulse duration (τ_{ac}) and Gaussian fit (dashed black line).

Tab. 4.1 presents a summary of the results of the pulses with the shortest duration obtained for different iterations of the amplifier setup. Within two different pump diode lasers with wavelengths of 918 and 976 nm and two different seed sources with high- and low repetition rates, the shortest pulse duration was obtained for the last experimental setup, together with the broadest spectrum, highest peak power, and energy of the pulse. The highest average power was achieved for the amplifier based on a high-repetition-rate seed source pumped by a 976-nm diode laser. Also, the summary points out the better performance of the second setup of the amplifier pumped by the longer wavelength pump.

Tab. 4.1. Summary of parameters obtained in GMN amplification for different pump diode lasers and seed sources for the shortest pulse duration in each iteration of the amplifier. λ_{pump}, the wavelength of the pump diode laser; P_{pump}, the average pump power; λ_c, the central wavelength of amplified pulses; $\Delta\lambda$, the FWHM of amplified pulses; τ_{FROG}, the pulse duration obtained by FROG measurement; τ_{TL}, TL pulse duration; P_{out}, average output power; P_{peak}, peak power; E, the energy of the pulses. Lines shaded in grey correspond to results obtained for high-repetition-rate laser sources, and lines shaded in white for low-repetition-rate laser sources.

λ_{pump} [nm]	P_{pump} [W]	λ_c [nm]	$\Delta\lambda$ [nm]	τ_{FROG} [fs]	τ_{TL} [fs]	P_{out} [W]	P_{peak} [kW]	E [nJ]
918	7.23	1069	39	80	63	2.30	230	18.4
	5.36	1089	75	47	41	1.56	1090	51.2
976	7.94	1078	67	51	43	2.85	420	22.8
	7.94	1100	121	33	29	2.45	2290	80.5

When these results were published, the pulse duration of 33 fs was the shortest obtained in the GMN amplification process. After that, similar pulse durations were obtained but linked to lower average power [10]. The pulse energy of 120 nJ before the compression was also higher than that recorded in the first demonstration of GMN amplification [9]. Since then, progress has been made, and the results with higher energies have been published using larger mode area fibers in the amplifier [72,200].

4.4.3. Relative intensity noise measurements

One of the methods used to characterize the amplitude stability of a laser source is using RIN. It describes fluctuations in the average power of a recorded signal over a given period. This measure represents how stable the signal's average power is. RIN measurements are gaining popularity as a method to compare laser systems. Integrated RIN is a beneficial comparative measure for describing different laser setups if measured in the same frequency range.

In absorption spectroscopy, the RIN of the light source can be the dominant noise source [201]. A lower RIN of the light source can directly result in a higher SNR of the acquired spectra, which allows for shorter acquisition times and improved detection limits [175,202]. At the same time, it has been demonstrated that a high RIN can limit the achievable SNR in dual-comb spectroscopy [203]. Due to the possibility of using the presented GMN amplifier for spectroscopy, a measurement of RIN values complemented the characterization of the laser source. In addition, it should be emphasized that before this study, the noise properties of the GMN amplifier had never been discussed in the literature. Previous studies have shown that various nonlinear processes can produce excess intensity and phase noise [204–207]. It was unknown whether the GMN amplification process adds noise to laser pulses.

The measurements were conducted using a procedure that is similar to the one outlined in the literature [190]. Each signal was recorded 500 times to reduce discrepancies. The recorded signals were converted to the frequency domain using the Fourier transform and normalized by their average value. The obtained results present the power spectral density (PSD) across the 10 Hz to 430 kHz frequency range. To improve the amplitude resolution, an oversampling method was employed, as well as digital filtering during oversampled signal calculations and an anti-aliasing filter at the oscilloscope's input. The last step involved calculating the integrated RIN root-mean-square (RMS) by integrating the PSD over the frequency range of 10 Hz to 430 kHz.

For both seed sources (the high- and low-repetition-rate lasers), RIN and integrated RIN RMS measurements were performed after the final compressor at the highest pump power level. Apart from that, RIN was also measured for the seed sources themselves to determine the contribution of the GMN amplification process to the overall noise. The results can be observed in Fig. 4.18. It is noticeable that the high-repetition-rate laser has a much lower integrated RIN of 0.078% compared to the low-repetition-rate laser with a value of 0.145%. This difference impacts the integrated RIN values for amplified pulses, which are 0.231% and 0.578%, respectively. It can be linked to the quality of driving electronics of the seed lasers or the used mode-locking mechanism. The high-repetition-rate laser is a commercially available product used as a metrological frequency comb. For both seed sources, the integrated RIN value of the amplified output pulse from the GMN is at least three times higher than the value measured for the seed source alone. As a result of this noise properties characterization, it can be concluded that the GMN amplifier significantly increases the signal's amplitude noise. It should be noted that this work aimed to characterize a GMN amplification regime for two different sources, not to construct a low-noise amplifier. The RIN values for GMN amplification should be a topic for additional study as to what it depends on, what factors influence the emerging noise, and whether there are methods to decrease it.

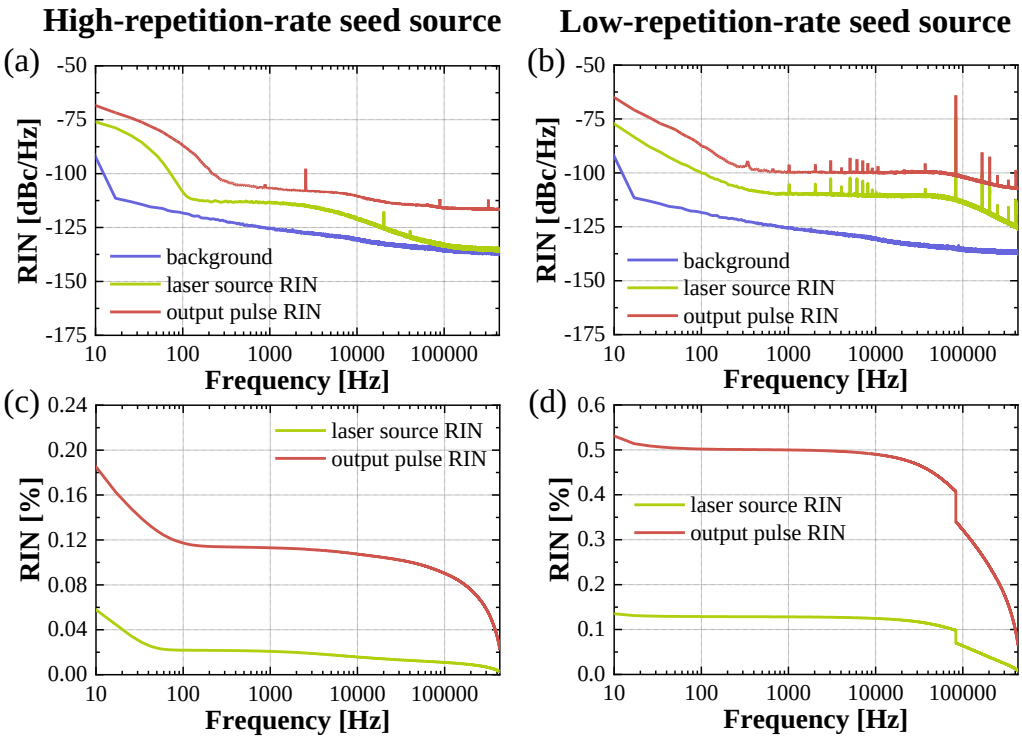

Fig. 4.18. Characterization of the intensity noise of laser sources (green) and also amplified and compressed output pulses (red): RIN results for (a) the high-repetition-rate and (b) the low-repetition-rate seed source, together with integrated RIN for (c) the high-repetition-rate and (d) the low-repetition-rate seed source. For comparison, background noise (blue).

4.5. DFG source based on GMN-amplified frequency comb

As outlined in Section 2.5, DFG is one of the essential methods for obtaining broadband and stable sources for laser spectroscopy in the mid-IR. The experimental setup for amplifying laser pulses presented above provides an ideal basis for a DFG source, as it delivers sub-100 fs pulses with high average power, translating into the high peak power needed for nonlinear processes. In addition, choosing a high-repetition-rate seed source enables easy locking of the oscillator, as it is a commercial source already equipped with all necessary actuators to control the f_{rep} and f_0, as well as electronics needed for locking both frequencies. The repetition rate of the OFC allows it to operate in the range of repetition rates often used in combination with gas absorption cavities. Additionally, it is in the range of nominal resolution of standard FTSs used in laboratory work, so measurements with a resolution of f_{rep} may be carried out. A detailed scheme of the DFG source based on the GMN amplifier is presented in Fig. 4.19. The heart of the system is a commercially available OFC, referred to as a high-repetition-rate laser in previous Sections, with the GMN amplifier pumped by a 976-nm diode laser at the highest pump level. The characteristics of this system are shown in Fig. 4.11 and Fig. 4.12.

The laser radiation from the final compressor in the amplification setup was divided into two parts: signal and pump, via the set of a half-wave plate (HWP) (Thorlabs, WPH05M-1064) and polarization beamsplitter (PBS) (Thorlabs, PBS123). The position of the HWP could change the splitting ratio. In the signal arm, a process of SSFS in the HNLF was used to redshift the wavelength of the pulse. Another HWP was placed just before the HNLF to adjust the input polarization. The light was collimated into a fiber with an aspherical lens with a focal length

of 3.1 mm. After the fiber, an optical filter was placed (Thorlabs, FELH1150) to transmit light only above the wavelength of 1150 nm. Due to this, any left pump light would be cut out, as well as a DW that was also generated in the HNLF. In the pump arm, there was a delay line to match the optical paths in both arms. It was composed of a retroreflector mirror placed on the motorized translation stage (Thorlabs, MTS25-Z8). Moving the stage could extend or shorten the length of the pump arm.

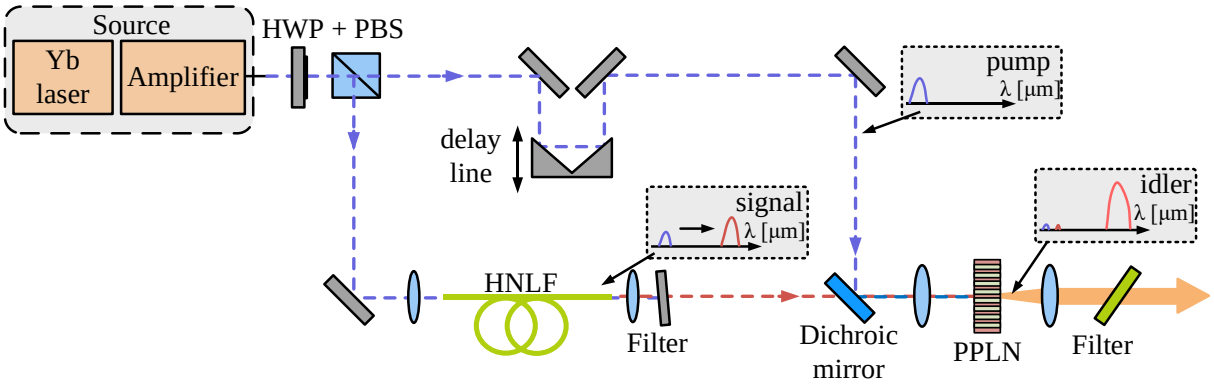

Fig. 4.19. Scheme of the difference frequency source for the mid-IR region. HWP, half-wave plate; PBS, polarization beamsplitter; HNLF, highly nonlinear fiber; PPLN, periodically poled lithium niobate crystal.

Once the two arms were combined with a dichroic mirror (Thorlabs, DMSP1180), the pulses were focused on a nonlinear crystal where the differential frequency generation occurred. The chosen lenses focused the beam on the crystal and then collimated it, which had a focus length of 50 mm. The focusing lens was an achromatic one to correct for chromatic aberration (Thorlabs, AC254-050-C-ML), and a collimating one was made from calcium fluoride to transmit the mid-IR light (Thorlabs, LA5763-E).

The chosen crystal was a PPLN (Covesion, MDFG4-0.5-1), placed in an oven and kept at a fixed temperature of 40 °C. Despite many other crystals available on the market, PPLN crystals are still very attractive due to their high conversion efficiency. After the collimating lens, there was also a filter in the form of a germanium window (Thorlabs, WG91050). Its task was to eliminate residual signal, pump, and generated visible light from the SHG process in the crystal, as well as the sum frequency generation from the pump and signal light.

4.5.1. Soliton self-frequency shift

Four different fibers were evaluated to choose the best nonlinear fiber for the SSFS process, some of them with various lengths. Measured parameters were mainly the input power, the central wavelength of the generated soliton and its width, output power, general efficiency, and stability of the process, as well as higher-order soliton generation. The setup for testing different fibers was just the signal branch of the DFG setup presented in Fig. 4.19. To spectrally tune the solitons, the laser power coupled to the fiber was changed from 100 mW to 250 mW just by changing the angle position of HWP before the PBS. After the light coming out of the fiber was collimated and the residual pump was filtered, the beam was directed into the OSA to record the spectra.

The first item examined during the experiments was a fiber rod (Menlosystems, SN505) with a length of 18.5 cm. The obtained spectra for different input powers are depicted in Fig.

4.20. It can be noticed that for maximum pump power, the central wavelength of the soliton only shifts to 1350 nm. The only advantage is the relatively high power in the soliton, which is 57 mW, corresponding to 23% conversion efficiency.

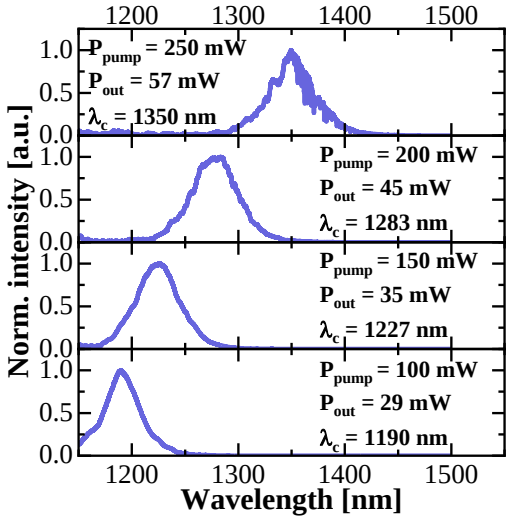

Fig. 4.20. SSFS for different pump powers in fiber rod from Menlosystems. P_{pump}, launched pump power; P_{out}, output soliton power; λ_c, soliton central wavelength.

The next study subject was a commercial fiber from NKT Photonics (NL-3.2-945) at two different lengths, 1.3 and 0.4 m. The results are shown in Fig. 4.21(a) and (b), respectively. The shift is further for a longer piece of nonlinear fiber, but the output power is lower. Both of these features arise from a longer medium to interact with, as the transmission loss is higher, the average power in a soliton decreases. In the case of 1.3-m fiber, the soliton shifts up to 1493 nm for the maximum pumping power. The average power stored in the soliton is 37 mW, which corresponds to 15% conversion efficiency. As for the 0.4-m fiber, the results are 46 mW of power for the soliton with a central wavelength of 1426 nm and 18% conversion efficiency. The shapes of the obtained spectra for this fiber are also not ideal soliton shapes, and second-order soliton can be slightly seen.

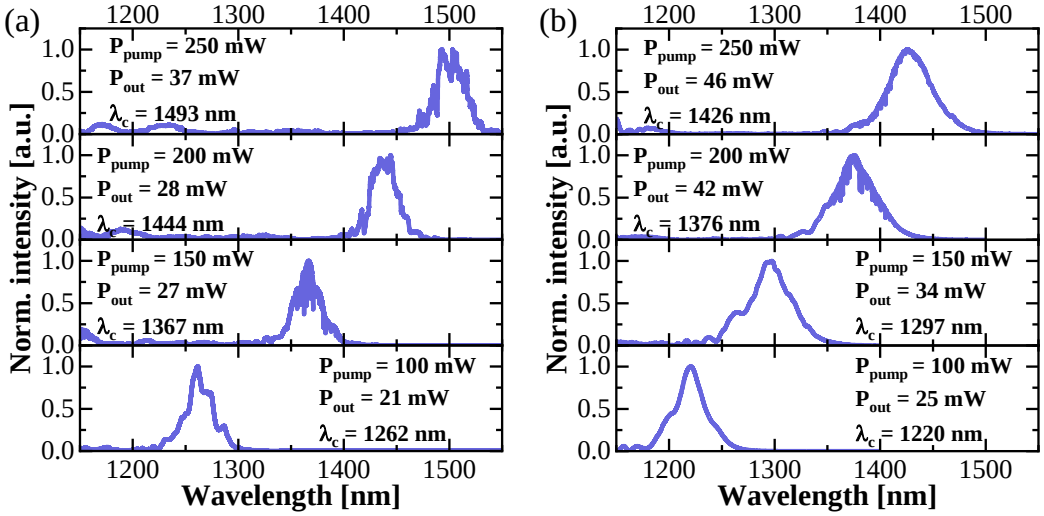

Fig. 4.21. SSFS for different pump powers in NKT Photonics fiber (a) 1.3 m long and (b) 0.4 m long. P_{pump}, launched pump power; P_{out}, output soliton power; λ_c, soliton central wavelength.

The last two nonlinear fibers were made in-house and were similar to the one presented in [208]. They were fabricated in the Laboratory of Optical Fiber Technology in Lublin as a part of a research project. The fiber A had a length of 1 m. For this fiber, the optical soliton shifts furthest, which is 1466 nm, with an average power equaling 46 mW, corresponding to 18% conversion efficiency. However, the spectrum's shape does not resemble the ideal soliton shape. Fig. 4.22 presents the SSFS for the in-house fiber A.

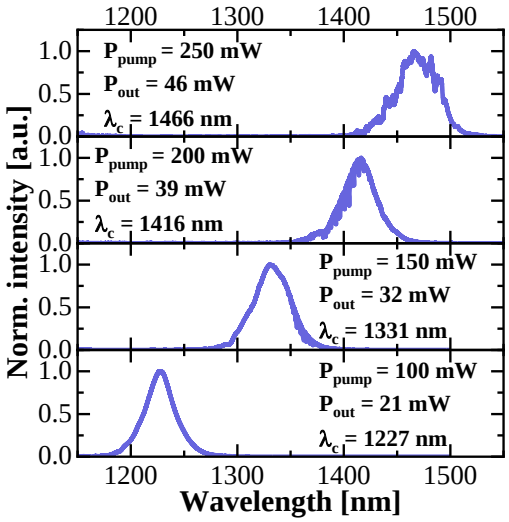

Fig. 4.22. SSFS for different pump powers in in-house-made fiber A 1 m long. P_{pump}, launched pump power; P_{out}, output soliton power; λ_c, soliton central wavelength.

The in-house-made fiber B was assessed at 0.8 and 0.65 m lengths. The obtained spectra are depicted in Fig. 4.23. A second-order soliton can be noticed for both of them, but the soliton shapes resemble the ideal soliton shape. For the longer fiber segment, the optical soliton at the highest pump power is generated at 1413 nm with the average output power at the level of 42 mW. For the shorter piece of fiber, the soliton shifts up to 1423 nm with 49 mW of the average power. The conversion efficiency is 17 and 20% for the longer and shorter fiber, respectively.

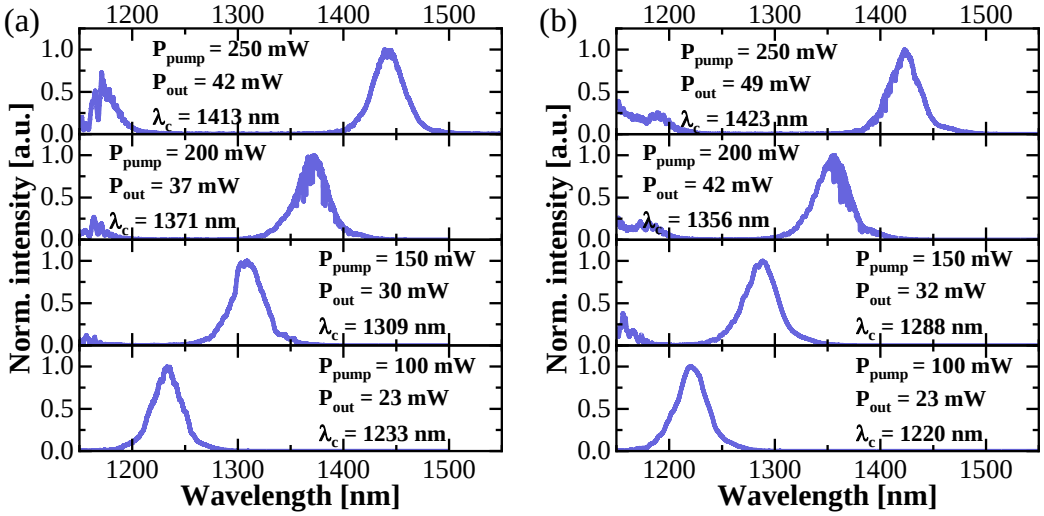

Fig. 4.23. SSFS for different pump powers in in-house-made fiber B (a) 0.80 m long and (b) 0.65 m long. P_{pump}, launched pump power; P_{out}, output soliton power; λ_c, soliton central wavelength.

A table was constructed to summarize all the results obtained for different fibers of different lengths. Tab. 4.2 presents the following data for a pump power of 250 mW: output power with power conversion efficiency and the central wavelength of the soliton. It has to be noted that the power conversion efficiency measurements were carried out using the laser power obtained in front of the fiber tip (the launched power), which means that they include non-ideal coupling to the fiber in the final value. The power conversion efficiency for the fibers was in the range of 15-23%, which was similar to the literature reports: 28% in [208], 22% in [209], and 10% in [210]. Also, the efficiency is higher for the shorter pieces of the same fiber compared to the longer ones, which may be due to higher losses while light interacts with a longer medium, as well as a generated second-order soliton, which the filter could block at the end of the fiber. Considering the achieved spectral range, the obtained output power, and the smoothness of the pulse spectrum for the generated solitons in all tested fibers, it can be concluded that the in-house-made fiber B gives optimal results.

Tab. 4.2. Results of SSFS for maximal pump power for different fibers. L, length of the fiber; P_{pump}, pump power launched to the HNLF; P_{out}, output power out of HNLF; η, power conversion efficiency; λ_c, the central wavelength of the SSFS.

Fiber type	L [m]	P_{pump} [mW]	P_{out} [mW]	η [%]	λ_c [nm]
Menlosystems fiber rod	0.185	250	57	23	1350
NKT Photonics	1.3	250	37	15	1493
NKT Photonics	0.4	250	46	18	1426
In-house-made fiber A	1	250	46	18	1466
In-house-made fiber B	0.8	250	42	17	1413
In-house-made fiber B	0.65	250	49	20	1423

For the final DFG setup, the nonlinear fiber was shortened to 0.43 m, which allowed to avoid the second-order soliton generation. Additionally, higher power of a launched beam was needed to obtain the same frequency shift with a shorter fiber length. So, slightly altering the pump power would result in only a small variation of the shift frequency. It left a larger margin for changing the wavelength of the generated soliton with smaller changes in the input power. The results for changing the pump power from 150 mW up to 450 mW are depicted in Fig. 4.24. In addition to spectra, autocorrelation of the solitons was also recorded. The soliton central wavelength shifted from 1.2 to almost 1.55 μm, with the average power in a soliton from 26 to 82 mW. The pulse duration of the frequency-shifted solitons remains at a similar level for different pump powers. For one of the shortest solitons, obtained for the pump power of 250 mW, the TL pulse duration value was 46 fs, and the measured one was 49 fs. The pulse duration of other solitons was also close to the TL. All the solitons have almost ideal hyperbolic secant shape, which provides a good foundation for further conversion to mid-IR.

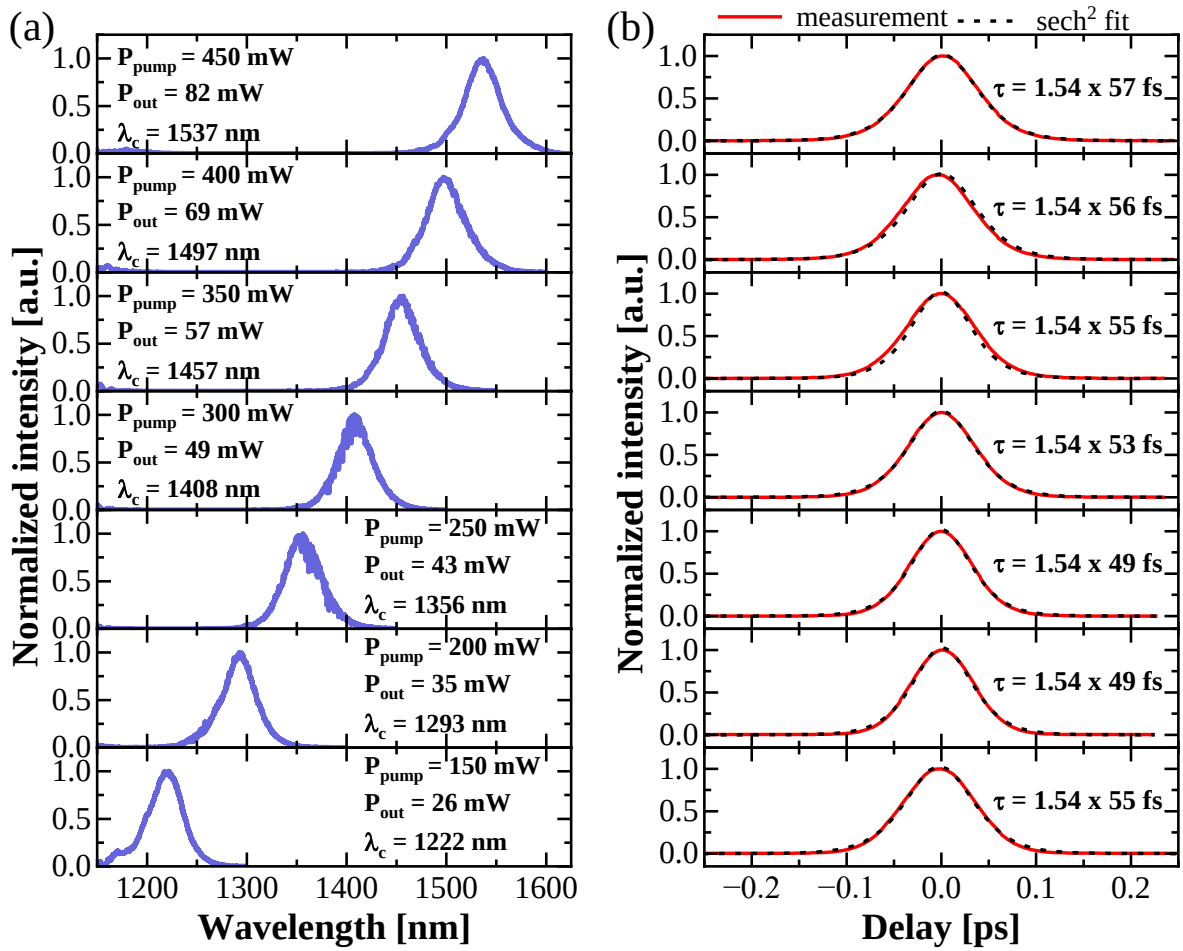

Fig. 4.24. (a) the spectra, with launched pump power (P_{pump}), soliton output power (P_{out}), and its central wavelength (λ_c) and (b) autocorrelation function (solid red line) and its duration (τ) with hyperbolic secant fit (dashed black line) of SSFS in 0.43-m-long in-house-made nonlinear fiber B used in the DFG setup.

4.5.2. Optical spectra obtained for DFG-based OFC

In order to achieve the highest efficiency when converting an OFC to mid-IR, several conditions must be met. The two beams focused on the nonlinear crystal must overlap as much as possible and be of similar size, phase matching conditions must be met, and the difference in optical paths between the arms must be as small as possible. After all the necessary steps had been carried out, mid-IR radiation was obtained for the signal beam of around 50 mW and the pump beam of 2.4 W, both depending on the soliton wavelength. Ten different optical spectra were recorded, acquired for both different periods of the PPLN crystal and different wavelengths of the signal beam. Fig. 4.25 shows the optical spectra obtained using the DFG process, together with the central wavelengths and average output powers of the mid-IR beam.

From the obtained results, it can be noted that the highest output power of 95.45 mW was achieved for the central wavelength of 3752 nm (2665 cm^{-1}). The lowest powers were achieved at the ends of the ranges, that is, for the shortest (3372 nm) and longest (4902 nm) wavelengths. It is also worth noting that the transmission range of the PPLN crystal ends at a wavelength of 5000 nm, which may be the reason for the low power obtained for the spectrum with the longest wavelength.

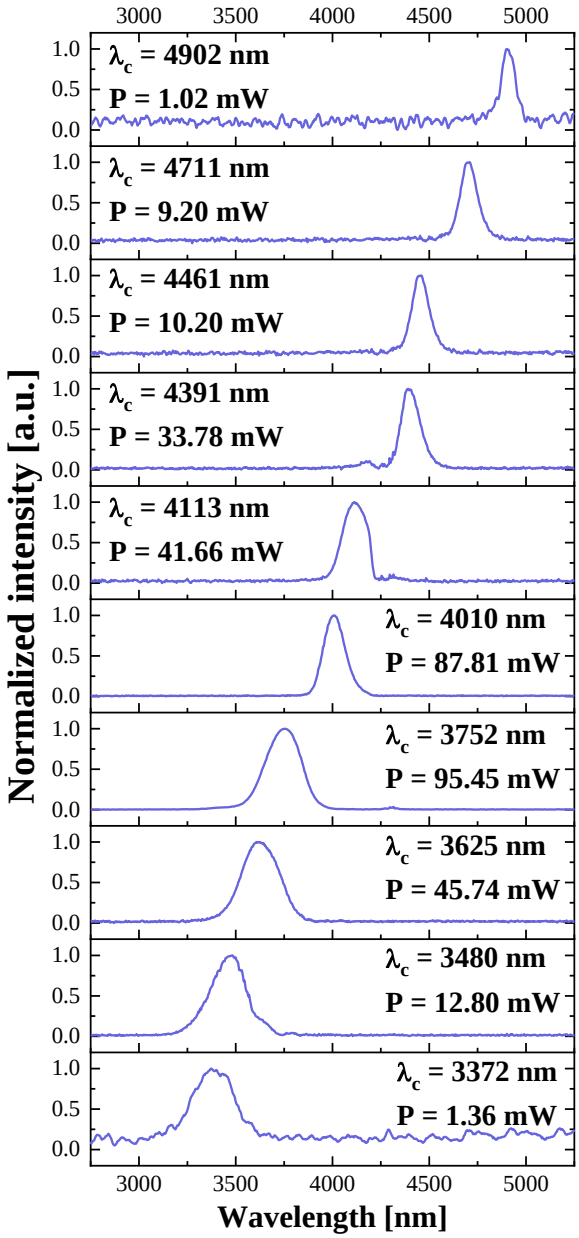

Fig. 4.25. Spectra of DFG-based OFC from Yb-doped fiber laser and GMN amplifier for different crystal periods, with central wavelengths (λ_c) and average output power (P).

In Fig. 4.26, a summary of the obtained spectra was gathered, with the plot presenting average output power as a function of central wavelength. DFG sources in the range of 3-5 μm are reported in the literature and include generation by mixing two independent sources (for example, a mode-locked oscillator and CW laser [99,211]) or by using one master OFC source (described in detail in Section 2.5.2). The DFG frequency combs obtained using an Er-doped fiber laser can be characterized by an average power from dozens to even over a hundred milliwatts [105,106,118], however, their tuning range was not as broad as the one presented in this dissertation. As for DFG setups using the same starting wavelength, Yb-doped fiber laser [115,116], the tuning ranges of the obtained spectra in the literature were similar, and the achieved powers were higher than for the DFG shown above. In Ref. [117], the average power was higher than 140 mW throughout the tuning range and reached a maximum of 237 mW. It should be noted that some of these cited sources used stabilization of the delay line for better performance of the DFG sources.

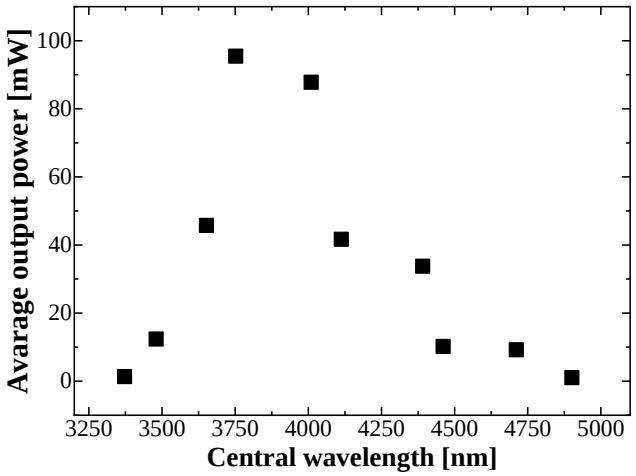

Fig. 4.26. The average output power of the generated beam in the mid-IR as a function of the central wavelength of the spectrum.

4.6. Conclusions

This Chapter characterized a novel type of amplification regime, experimental results, and numerical analysis. An in-depth analysis was presented, consisting of pumping the GMN amplifier with two laser diodes operating at different wavelengths and seeding the amplifier by two lasers with different repetition rates. For both seed sources, spectra of the amplified pulses extended beyond the conventional Yb-doped fiber gain window, and the numerical simulations confirmed the GMN pulse evolution. The shortest obtained pulse had a duration of 33 fs, which is, up to date, the shortest pulse duration reported for this type of amplification. Tab. 4.3 compares results obtained for this work with outcomes from the literature. In Ref. [10], the pulse duration matched 33 fs, but the energy before and after the compression was lower than for results shown here. The pulse energy of 120 nJ before compression is also higher than the one recorded in different demonstrations of GMN amplification [9,212,213] but lower than reported in Ref. [72], where the authors used an LMA fiber in the amplifier.

Tab. 4.3. Results of the GMN amplification for literature. d_{core}, a core diameter of an active fiber; f_{rep}, a repetition rate of a seed source; τ, duration of an amplified and compressed pulse; $E_{uncomp.}$, the energy of an amplified but not compressed pulse; $E_{comp.}$, the energy of an amplified and compressed pulse.

Reference	d_{core} [µm]	f_{rep} [MHz]	τ [fs]	$E_{uncomp.}$ [nJ]	$E_{comp.}$ [nJ]
Sidorenko et al. [9]	5	12.5	42	107	-
Stoliarov et al. [212]	10	0.95	57	53	-
Sidorenko et al. [10]	10	31	33	84	58
Xing et al. [213]	10	43	34	-	92
Sidorenko et al. [72]	30	5.4	37	1200	-
This work	10	30	33	120	80
This work	10	125	51	33	23

In this study, the Author constructed the amplification setup, performed all the experimental measurements, and managed data processing. The numerical analysis and theoretical side of this study were implemented by the research group from KTH Royal Institute of Technology in Stockholm. In the next step, the compressed pulses from the high-repetition-rate source were further used to seed the DFG. The setup design consisted of selecting the appropriate fiber for the SSFS process, which the Author conducted. It enabled obtaining laser radiation from a 3-5 μm spectral range with an average power of up to 100 mW, which is at a similar level or lower than for sources built so far [105,115,117].

The GMN amplification still needs to be further investigated in order to be better understood and to make better use of its advantages. In particular, continuing to identify parameters influencing the excess noise, as well as studying this amplification regime at different spectral regions, for example, for Er-doped fiber lasers. For the presented DFG-based OFC to be used as a source for spectroscopy, the f_{rep} and output power of the comb source should be stabilized. It would make the source more stable, which would translate into better spectroscopic sensitivity.

Chapter 5.

Laser spectroscopy in the mid-infrared

5.1. Introduction

In this Chapter, experimental results for laser spectroscopy are presented. First, the details of the constructed DFG source are presented, where the Er-doped fiber laser was utilized as an initial seed source. Next, two examples of laser spectroscopy are introduced. The first one is related to multispecies gas detection, where methane and ethane were measured at the same time. Through the use of a broadband source, it is possible to measure whole absorption bands of molecules and distinguish the lines of different gases. Besides measurements, a fit based on the HITRAN database was conducted, and it matched the obtained results. This work was published in [118]. The second experiment involved using an ARHCF to elongate the interaction length between light and gas, which led to increased detection sensitivity. This experiment was the first demonstration of combining the ARHCF and OFC for broadband spectroscopy in the mid-IR. Access to this type of fiber, together with the experience in using them and filling them with gas samples, was enabled by Piotr Jaworski and Karol Krzempek from Wrocław University of Science and Technology. The fiber itself was manufactured by Fei Yu and his research group from the Shanghai Institute of Optics and Fine Mechanics. The study compares ARHCF performance with a commercially available MPC of similar length and includes detailed parameters for both gas absorption cells. The experiment proved that broadband sources, like OFC, can be combined with adequately designed ARHCFs to enable measuring both narrow and broad gas absorption spectra. The results of this research were published [164]. An increase in the resolution of the measurements conducted by the presented DFG source is possible due to the capabilities of the home-built FTS. It could be even further scaled up when using the sub-nominal method. For both experiments, prof. Aleksandra Foltynowicz from Umeå University in Sweden provided support and expertise in performing spectroscopic measurements and additional data processing.

5.2. DFG source

The DFG source used for the spectroscopy experiments had the same principle of operation as the one presented in Fig. 2.14(b) with a 1.56 μm seed. The scheme for the DFG source is depicted in Fig. 5.1, and the details can be found in Ref. [118]. It was mainly constructed by the supervisors of the thesis, Karol Krzempek and Grzegorz Soboń. The setup starts from a graphene mode-locked Er-doped fiber laser with an operating wavelength of 1565 nm. The

laser generated pulses with a duration of 320 fs at a repetition rate of 125 MHz. The oscillator can be considered an OFC, as the f_{rep} was controlled and stabilized. For this purpose, two approaches were implemented. One was temperature stabilization, achieved by placing the entire laser resonator onto a custom-designed heating board confined in a 3D-printed enclosure. The laser cavity was kept at a stable temperature of 35 °C, which limited the influence of ambient temperature drifts. The second approach was to incorporate a piezoceramic stretcher with a 40-µm displacement onto the active erbium-doped fiber, which allowed for controlling the f_{rep}. The details about methods of f_{rep} stabilization can be found in Ref. [123].

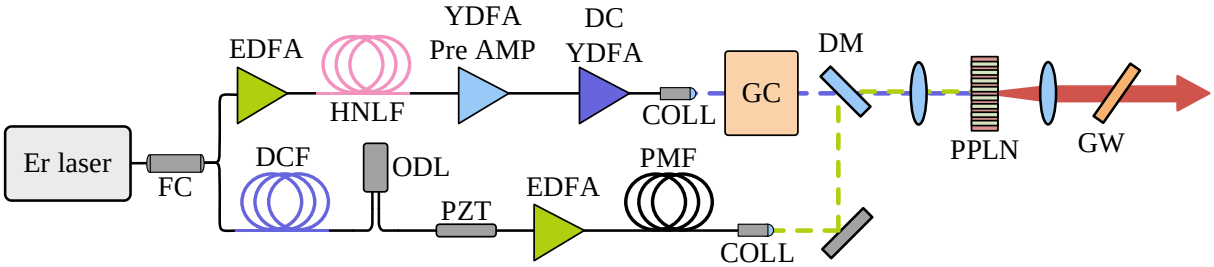

Fig. 5.1. Schematic of the fiber-based mid-IR comb source. FC, fiber coupler; EDFA, Er-doped fiber amplifier; DC YDFA, double-clad Yb-doped fiber amplifier; HNLF, highly nonlinear fiber; DCF, dispersion compensating fiber; ODL, fiberized optical delay line; PZT, piezoceramic fiber stretcher; PMF, polarization-maintaining single-mode fiber; COLL, collimator; GC, grating compressor; DM, dichroic mirror; PPLN, periodically poled lithium niobate crystal; GW, germanium window.

The pulses generated by the mode-locked laser were divided into two separate arms with a fiber coupler. The first arm used dispersion-compensating fiber (DCF) to stretch the pulses in time through normal dispersion. Next, the pulses were amplified in the erbium-doped fiber amplifier (EDFA) and compressed in a single-mode, polarization-maintaining fiber (PMF). This method of amplification and compression is possible at this wavelength because the SMF at a wavelength of 1.56 µm has anomalous dispersion. In addition, this arm of the DFG source included a motorized fiber optical delay line to match the optical length of both branches and for precise adjustment, a piezoelectric transducer was added. In Fig. 5.2, an optical spectrum and autocorrelation measurement are presented for the compressed pulses after the collimator, which had a central wavelength of 1565 nm with 41 nm of FWHM, pulse duration of 99 fs, and average power of 77 mW.

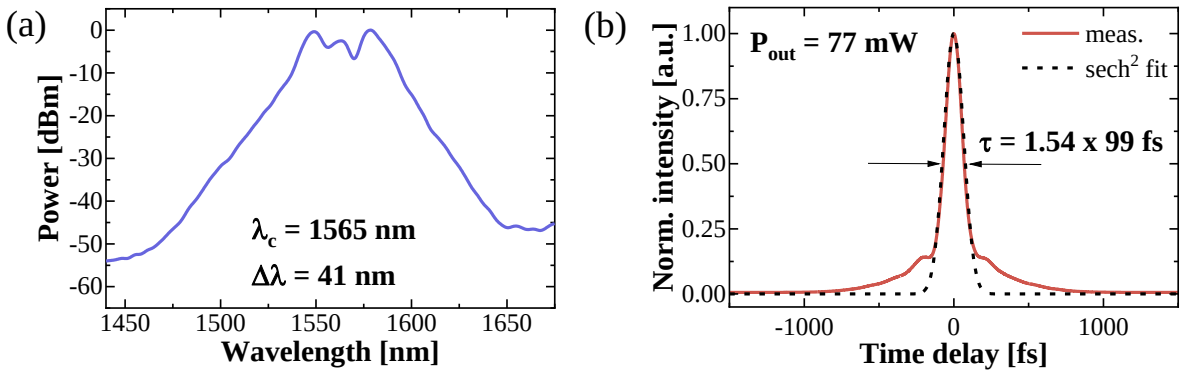

Fig. 5.2. Characterization of signal pulses for the DFG before the dichroic mirror. (a) Optical spectrum with the central wavelength (λ_c) and FWHM ($\Delta\lambda$). (b) Autocorrelation function (solid red line) with hyperbolic secant fit (dashed black line), pulse duration (τ), and average output power (P_{out}).

In the second arm, the pulses were converted to the shorter wavelength range. To achieve that, first, the 1.56 µm pulses were amplified to the average power of 280 mW with a pulse duration of 55 fs, to be then blueshifted. A DW generation occurred in the HNLF, which was spliced to the amplifier output. Then, the 1 µm radiation was amplified in a Yb-doped fiber pre-amplifier and subsequently in a double-clad Yb-doped amplifier. A free-space optics compressor based on a grating was used to compress the pulses. Before the dichroic mirror, the pulses had a central wavelength of 1060 nm, with an FWHM of 25 nm, a pulse duration of 195 fs, and an average power of 1.9 W. The characteristics of the pump pulses are presented in Fig. 5.3.

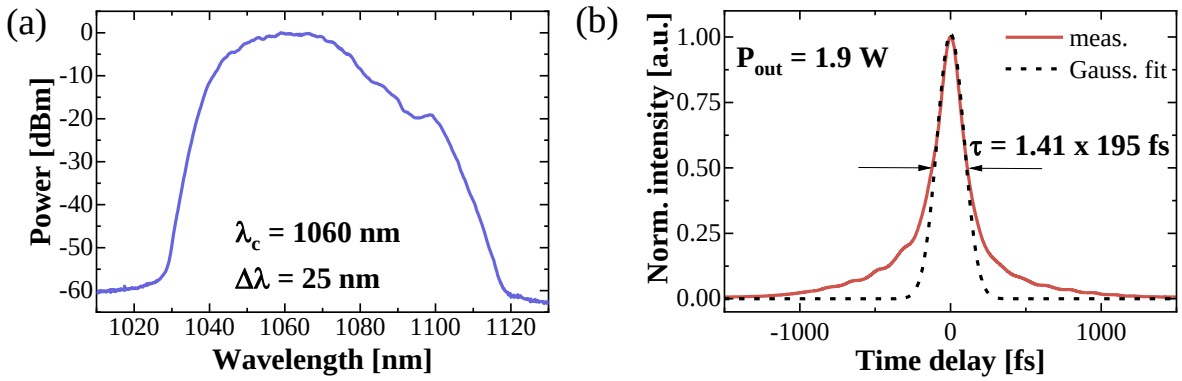

Fig. 5.3. Characterization of pump pulses for the DFG before the dichroic mirror. (a) Optical spectrum with the central wavelength (λ_c) and FWHM ($\Delta\lambda$). (b) Autocorrelation function (solid red line) with Gaussian fit (dashed black line), pulse duration (τ), and average output power (P_{out}).

The pulses from the signal arm were collimated and co-aligned on a dichroic mirror with a pump beam. Next, the achromatic lens with a 75 mm focal length was used to focus both beams onto a PPLN crystal with a 3 mm length. The crystal had five QPM periods (29.52-31.59 µm). DFG process in the crystal generated broadband radiation, which could be tuned between 2900 cm^{-1} (3450 nm) and 3400 cm^{-1} (2940 nm). The change could be made by switching the crystal period, tuning its temperature, or shifting the wavelength of the DW spectrum, which was influenced by how much power was coupled into the HNLF. In Fig. 5.4, different spectra of the DFG are presented, registered using a commercial Fourier-transform spectrometer (Thermo Scientific, Nicolet iS50). The highest obtained power was 70 mW for the central wavelength of 3160 nm (3165 cm^{-1}).

An essential aspect of constructing a DFG source for spectroscopy is stabilizing the spectrum and output power of the source, which depends on the temporal overlap between the pulses interacting in the crystal. The method was based on previous work [109,123], in which part of the generated mid-IR radiation after processing is used as an error signal for the PID controller, which generated a correction signal for a piezoelectric transducer driver controlling a length of the fiber in the pump arm of the DFG source. When the *OPD* between the signal and pump arm equaled zero, which corresponds to the perfect overlap between pulses, it resulted in the maximum average output power of the DFG.

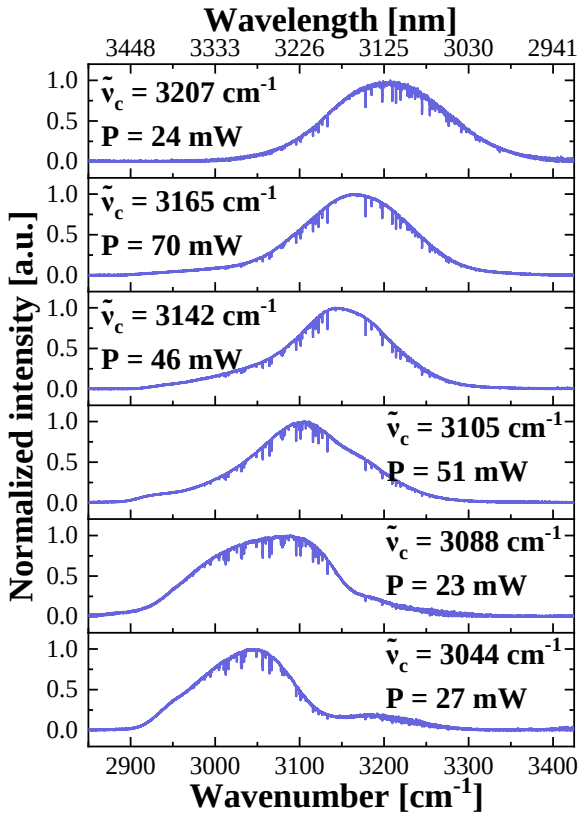

Fig. 5.4. Spectra of DFG-based OFC from Er-doped fiber laser for different crystal periods, with central wavenumber ($\tilde{\nu}_c$) and average output power (P).

To evaluate the performance of the stabilization loop, a 3-hour-long measurement of optical spectra was conducted (Fig. 5.5). When stabilization was turned off, the spectral envelopes fluctuated significantly. When the active loop was employed, the generated spectrum did not vary much during the 4.5 h measurement period.

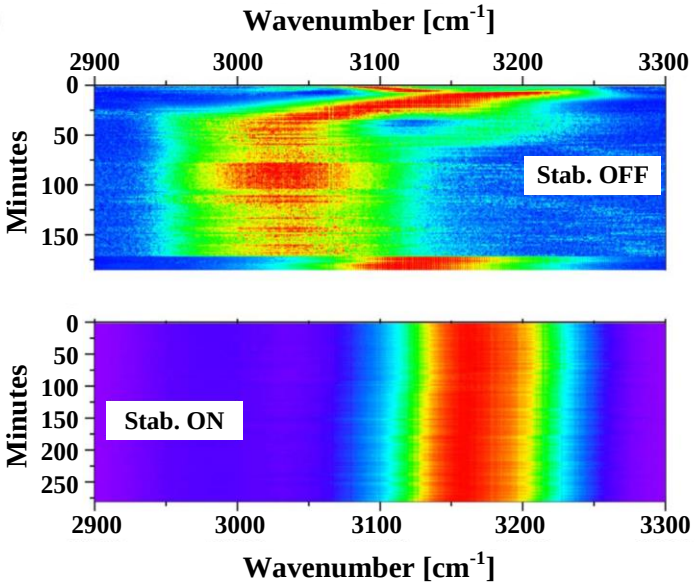

Fig. 5.5. Heatmaps showing the time evolution of the optical spectrum for non-stabilized and stabilized cases of the DFG-based OFC source.

Similar conclusions come from the output power measurement presented in Fig. 5.6. Without the stabilization, the power varies, but for the stabilized source, the average output

power fluctuation did not exceed a 1σ standard deviation of 0.2 mW in 4.5 h. This result is four times better compared to the non-stabilized case. Thanks to the active feedback loop, the thermal drift was compensated, and a tight overlap between pulses was ensured for long-time operation. The stabilization loop and related measurements were carried out by the assistant supervisor, Karol Krzempek.

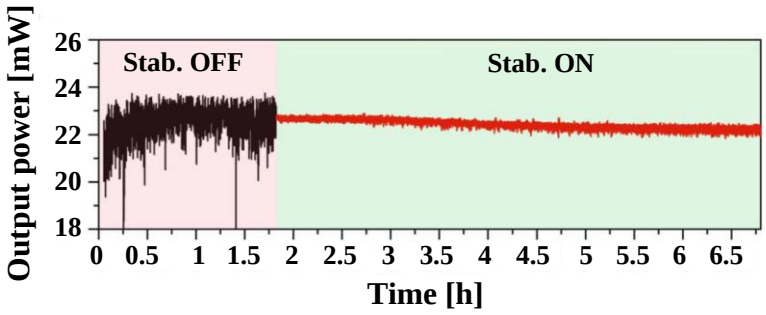

Fig. 5.6. Average output power stability of DFG-based OFC source as a function of time.

There are examples of similar DFG setups in the literature. For instance, in Ref. [105], the generated OFC spanned from 2.9 to 3.6 µm with 120 mW of average power, whereas in Ref. [119], the DFG covered the range from 2.8 to 3.5 µm with 500 mW of average power. Nonetheless, none of these DFG sources based on Er-doped fiber laser was fully stabilized in terms of output power and spectral envelope, like in the presented DFG via active lock of the DFG pulse overlap. The intra-pulse DFG approach is an alternative solution to avoid active pulse overlap control in DFG. Examples of IDFG generated from an Er-doped fiber laser were presented but suffered from relatively low output power [214].

5.3. Multispecies detection

The OFC source described above was used to detect absorption lines of methane (CH_4) and ethane (C_2H_6) simultaneously. The experimental setup consisted of the laser source, two cells filled with different gases, and an FTS. The scheme for this study is depicted in Fig. 5.7. The FTS was a home-built one with a design similar to the one in Ref. [175], which was constructed as a part of the Author's work. The details of the spectrometer are presented in Section 3.4.3. The gas absorption cells were 10 cm long each, one was filled with 615 ppmv of ethane at a pressure of 200 Torr, and the second was 0.245% of methane at 760 Torr.

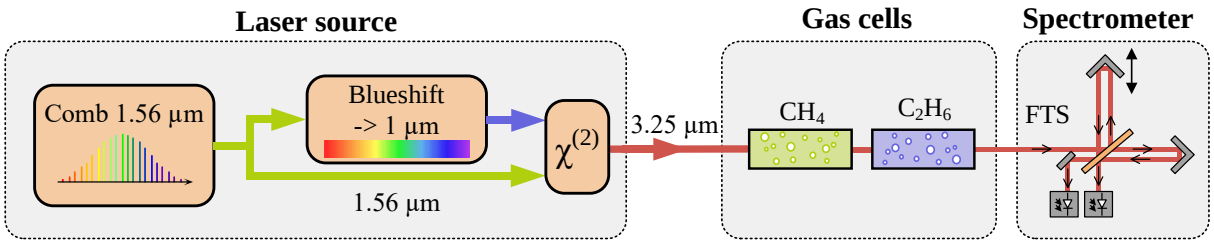

Fig. 5.7. Scheme of experimental setup for multispecies detection of methane and ethane. The laser source passes through two gas cells, and its spectrum is acquired by the Fourier transform spectrometer (FTS).

5.3.1. Procedure for acquiring the absorption coefficient

The measurements can be divided into two steps: reference measurement without the absorption cells and target measurement with the cells. The reference spectrum, defined as optical intensity as a function of wavenumber, is presented in Fig. 5.8(a), while the spectrum with CH_4 and C_2H_6 absorption is shown in Fig. 5.8(b). All the examples demonstrated in this Section come from actual experimental data from the study of multispecies detection. The interferograms were measured 100 times with a spectral resolution of 125 MHz and then averaged. In the reference spectrum, visible absorption lines can be affiliated with water vapor in the lab air. In comparison, in the spectrum obtained after the light beam propagated through two gas absorption cells with samples (Fig. 5.8(b)), apart from the same water vapor lines, there are also more prominent lines coming from methane and ethane, for example, the ones around 3020 cm^{-1}.

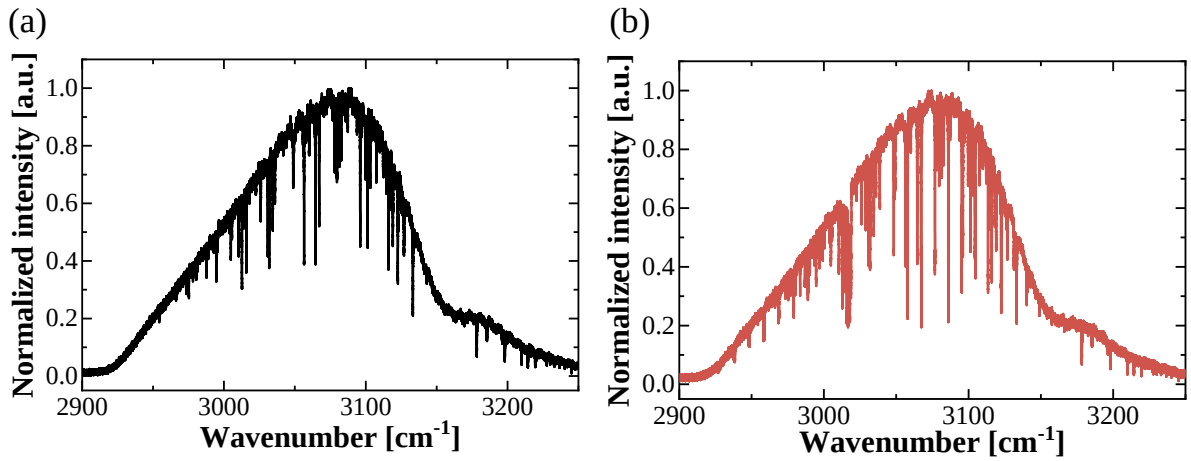

Fig. 5.8. The reference (a) and gas target (b) spectrum obtained by the home-built FTS for the DFG source. In the gas target spectrum, the light from DFG is propagated through two gas absorption cells with CH_4 and C_2H_6.

In the notation used in Section 3.2, the optical intensity from Fig. 5.8(b) corresponds to $I_T(\tilde{\nu})$, where absorption lines can be observed on top of the spectral envelope of the source $I_0(\tilde{\nu})$ (Fig. 5.8(a)). It needs to be noticed that the envelope shape is subjected to all the losses along the beam path, which are common for $I_0(\tilde{\nu})$ and $I_T(\tilde{\nu})$. Then, it is proper to address the spectral envelope as $I_B(\tilde{\nu})$, the background spectrum measured without the absorber. The transmission through the sample is then calculated by normalizing $I_T(\tilde{\nu})$ to $I_B(\tilde{\nu})$, giving the intensity transmission function, shown in Fig. 5.9.

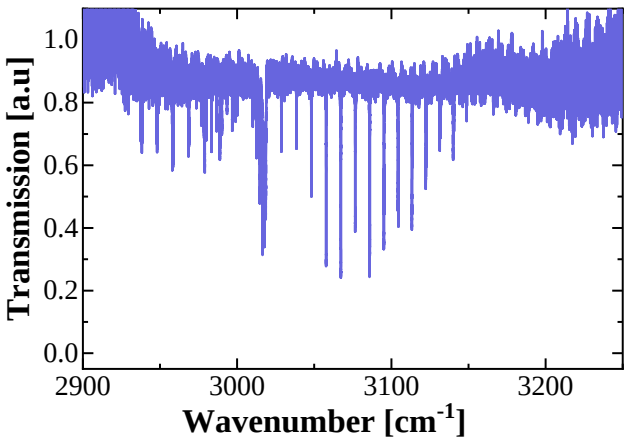

Fig. 5.9. The transmission through both gas cells (CH_4 and C_2H_6) obtained by normalizing the transmitted intensity to reference intensity.

The obtained transmission spectrum also shows the baseline. The cepstral method was used to remove the remaining baseline after the normalization process [215]. The cepstral analysis approach was developed initially for audio signal processing but is now widely used to eliminate the varying intensity of the light source and effects like etalons in the transmission spectrum. Fig. 5.10 demonstrates the transmission of a background retrieved by the cepstral analysis and the transmission through the gas sample without the background.

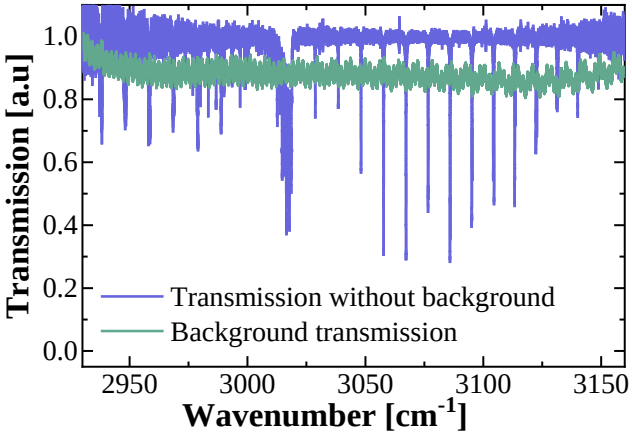

Fig. 5.10. The transmission (blue) through both gas cells (CH_4 and C_2H_6) without the background (green) retrieved from the cepstral analysis.

The absorption coefficient is then calculated from Eq. (3.8), but with the replacement of $I_0(\tilde{\nu})$ as $I_B(\tilde{\nu})$:

$$\alpha(\tilde{\nu}) = \frac{1}{L}\ln\frac{I_T(\tilde{\nu})}{I_B(\tilde{\nu})} \,. \tag{5.1}$$

The absorption coefficient resulting from these calculations is presented in Fig. 5.11. In parallel, the fitted models of methane and ethane absorption coefficients are calculated using the Voigt profile, the experimental specifications (like gas pressure and temperature), and the line parameters from the HITRAN 2016 database [216]. For the model, the only fitting parameters were the gas concentrations.

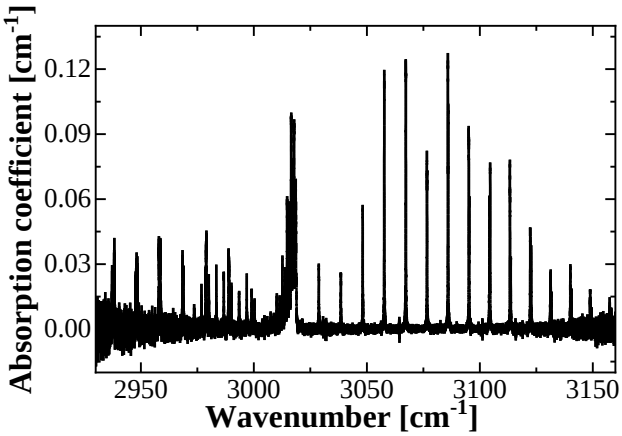

Fig. 5.11. The absorption coefficient of CH_4 and C_2H_6 calculated from Eq. (5.1).

For this experiment with multispecies detection, the model fitting and the cepstral analysis were conducted in collaboration with prof. Aleksandra Foltynowicz (Umeå University). The experiment results are shown in Fig. 5.12, where the absorption coefficient calculated from the transmission spectrum is shown in black, and the blue and red lines present the fitted models (plotted in negative for clarity). The lower panel of Fig. 5.12 illustrates the residuum of the fit and demonstrates a good agreement between the model and the experimental data. The results of this study were published [118]. The study showed that constructed DFG-based OFC, together with FTS, are capable of multispecies detection.

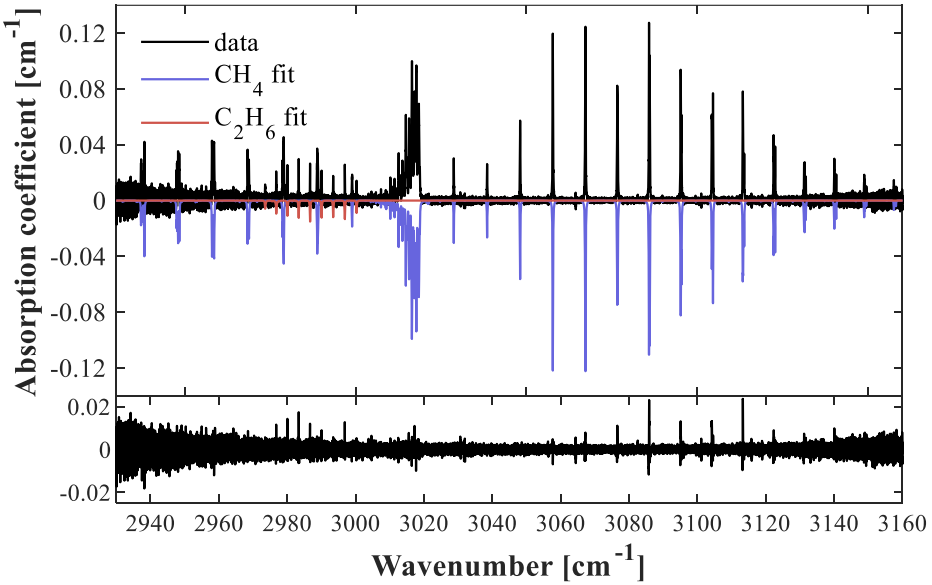

Fig. 5.12. Absorption spectra of 615 ppmv of CH_4 at 200 Torr and 0.245% of C_2H_6 at 760 Torr measured using the DFG comb and an FTS (black) compared to the spectra of the two molecules (blue for CH_4 and red for C_2H_6, in negative for clarity). The residuum of the fit is shown in the lower panel.

Furthermore, the NEA coefficient per spectral element was calculated from Eq. (3.9). Two spectra averaged 10 times were used for noise floor calculation. L_{eff} equaled 10 cm, and the acquisition time was 67 s. The standard deviation result was 9.3×10^{-4}, in the central range of spectra covering 150 cm^{-1}, and the number of spectral elements was ~36 000. From this data, the NEA coefficient was calculated, which amounted to 4.0×10^{-6} cm^{-1} $Hz^{-1/2}$ per spectral element. The obtained NEA coefficient is at a comparable level to the outcomes presented in the

literature for single-pass cells used in OFC Fourier transform spectroscopy [138]. However, the NEA values for MPCs and optical cavities are a few orders of magnitude better [142,217]. Therefore, the Author's further work was focused on different ways of increasing the light-gas interaction as it influenced the sensitivity of spectroscopy measurements.

5.4. Spectroscopy in an antiresonant hollow-core fiber

The OFC presented in Section 5.2 was also used to conduct an experimental study of ARHCFs for spectroscopic applications. As the absorption strength in spectroscopic setups, according to Lambert-Beer law, depends on the interaction length between light and gas, elongating the optical path is a non-complex method to increase the detection sensitivity. In conventional methods, the extension of the interaction length is realized through MPCs or optical cavities, but the novel approach is based on ARHCFs (fibers with an empty core, which can be filled with a gas sample). ARHCFs were used for spectroscopy before, either with CW laser sources in various spectral regions or with OFC, but only in near-IR. Before this study, the usage of ARHCFs together with OFCs in mid-IR for laser absorption measurements had never been presented in the literature.

The aim of the study was to compare the performance of ARHCF- and MPC-based gas absorption cells in broadband laser spectroscopy with the usage of OFCs. The direct comparison of both gas chambers could have been performed thanks to similar light-gas interaction lengths given by the ARHCF and the MPC. The setup consisted of a light source, gas absorption cells, and FTS to acquire the spectra. In Fig. 5.13, the setup scheme is presented. Comparable experimental conditions for both gas absorption cells were achieved by flip mirrors, which aligned the laser light into ARHCF or MPC.

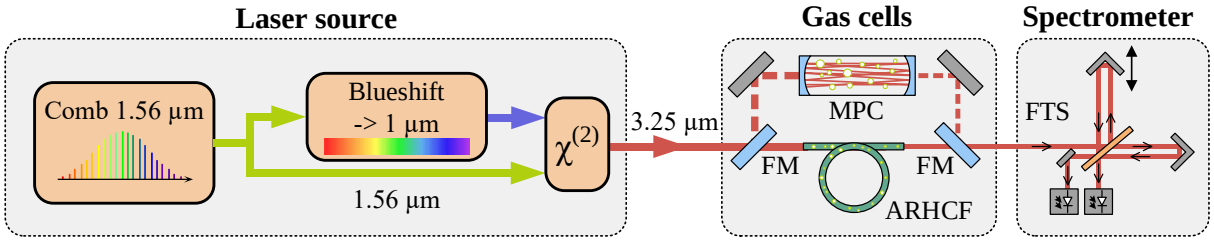

Fig. 5.13. Scheme of the experimental setup for laser spectroscopy using DFG-based OFC, two absorption gas cells: antiresonant hollow-core fiber (ARHCF) and multipass cell (MPC) that could be chosen by flip mirrors (FM), and Fourier transform spectrometer (FTS).

The details of the OFC source were described in the previous Section, as well as in Ref. [118]. For this experiment, the power measured at the output of the optical comb (before the first flip mirror) equaled 18 mW. The light from the frequency comb was directed to the ARHCF or redirected to the MPC by the flip mirror. The ARHCF used in this study was produced from fused silica glass preform of high purity (Suprasill F300) by the stack-and-draw technology [157,158], and its length was equal to 26.15 m. The fiber was manufactured by the research group from the Shanghai Institute of Optics and Fine Mechanics as a part of a collaboration with Fei Yu's research group. The fiber structure consisted of seven non-touching circular capillaries, which were pressurized during the fiber fabrication to prevent them from collapsing. The internal diameter of the capillaries was around 54 µm. They formed a fiber cladding area with a core diameter of around 84 µm, while the total diameter of the fiber was equal to ~318 µm. Fig. 5.14 shows an SEM image of the fiber's cross-section.

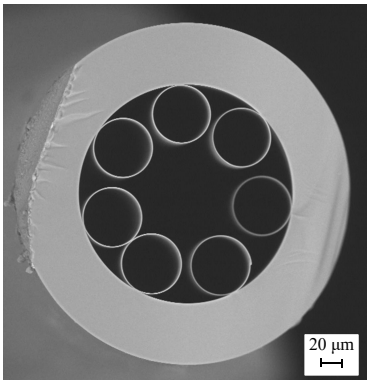

Fig. 5.14. SEM image of the ARHCF's cross-section. Seven non-touching capillaries with an internal diameter of 54 µm formed an air core with a diameter of 84 µm.

In the case of the used fiber, the wall of capillaries had a thickness of around 1 µm for the fiber to operate in the ~3.4 µm spectral region. As for the transmission window of the fiber, it is presented in Fig. 5.15 and covers almost 900 nm in the mid-IR range.

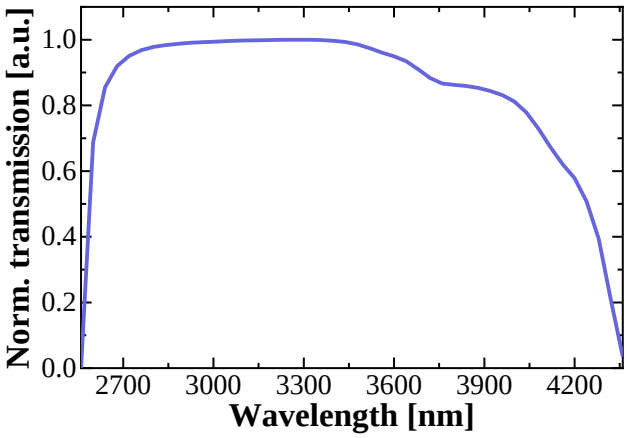

Fig. 5.15. Simulated transmission spectrum of the ARHCF in the mid-infrared range (calculations conducted by Shanghai Institute of Optics and Fine Mechanics).

The measurement of fiber attenuation for mid-IR was performed via a cut-back technique at the wavelength of 3.334 µm, leading to the value of 0.03 dB/m [158]. The simulations of the losses for the whole fundamental band of the ARHCF are shown in Fig. 5.16(b). Comparing the obtained result to solid core mid-IR fibers, the fiber loss for the ARHCF was 1.5 and 4.2 times lower than for commercially available fibers made from fluorozirconate (ZBLAN) and fluoroindate (InF_3), respectively [218]. In the near-IR, the losses for the ARHCF were around 0.5-1.5 dB/m (Fig. 5.16(a)). Higher losses for the near-IR region result from greater bending sensitivity of the ARHCF at shorter wavelengths due to the large core size for this spectral range. As presented in Ref. [163], the ratio of capillary diameter to core diameter directly impacts the bend loss. The ARHCF was optimized to work in the mid-IR, so the fiber exhibited good single-mode guidance in this range, resulting from the increased loss ratio of higher-order modes [163]. In the near-IR region, the designed fiber supported both LP_{01} and LP_{11} modes. The insets of Fig. 5.16(a) and (b) present supported modes at 1.574 µm and 3.334 µm, respectively.

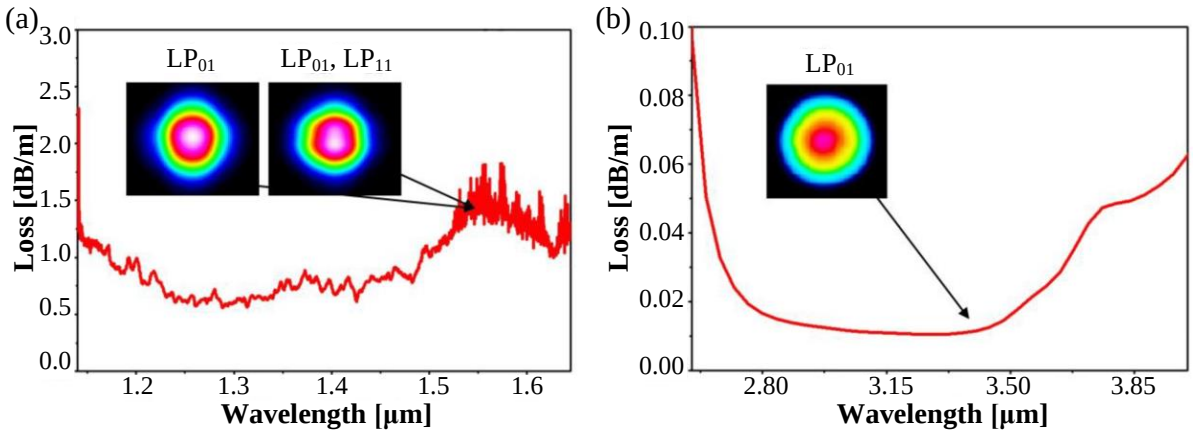

Fig. 5.16. Attenuation spectra of the used ARHCF in the (a) near-IR (measured) and (b) mid-IR (simulated) spectral regions. The insets present beam profiles of delivered modes measured at wavelengths pointed by the arrows. [158]

To make an absorption cell out of the ARHCF, it was necessary to close both ends of the fiber. The co-worker of the Author, Piotr Jaworski, was in charge of preparing this part of the experiment, as he has the knowledge and expertise about using ARHCFs as gas absorption cells. The ends of the fiber were glued to gas chambers, which were self-designed and developed based on existing SWAGELOK elements, described in detail in Ref. [219]. Both chambers were closed by the BaF_2 wedged windows, allowing the mid-IR light to enter the chamber. This method allows the use of the overpressure technique [220] to fill the fiber, which reduces the filling time compared to purely diffusion-based methods [221]. The filling practice began with using the pressure of 5 bar to fill the empty core of the ARHCF with the target gas mixture. This process took around 100 seconds, and then the pressure was subsequently equalized to the ambient value of 760 Torr, which happened by exposing both ends of the fiber to laboratory air. To obtain a stable gas pressure level, 15 minutes were required. After that time, the pressure was increased to 850 Torr, and the gas flow was started and maintained throughout the measurement. It is customary to perform spectroscopic measurements in a continuous gas flow to mimic the gas sensors used in real life, where this mode of operation provides a fast response in case of a change in concentration of a monitored substance. The total volume of the gas absorption cell developed based on ARHCF was around 0.77 mL, and the fiber was kept coiled with a diameter of 35 cm during the experiment. A plano-convex lens from calcium fluoride (CaF_2) was used to couple the light from OFC into the ARHCF, with a focal length of 50 mm. The focal length of the coupling lens was chosen to meet the numerical aperture of the ARHCF, which was ~0.03. The power of the frequency comb transmitted through the ARHCF filled with nitrogen (N_2) dropped to 2.85 mW, which was associated with fiber attenuation, light coupling, and bending loss. The total losses reached the level of 8 dB.

In the experiment, the performance of the ARHCF was compared to a commercial Herriot-type MPC [146] with a similar length of 31.227 m (Thorlabs, HC30 L/M-M02). The volume of the MPC was 0.85 L. To couple the light from the frequency comb to the MPC, a plano-convex lens from CaF_2 with a focal length of 500 mm was used. To collimate the light coming out of the cell, an additional 250 mm lens was used. The power measured at the cell's output equaled 1.47 mW, which corresponds to total losses of 10.8 dB. A decrease in power was associated with 80 internal reflections on the cell's mirrors, coupling, and transmission losses

through the windows of the MPC. The reflectance of the CaF_2 mirrors at the 3.3 μm wavelength is at the level of ~98.6%. For the same experimental conditions, the pressure of a gas sample inside the MPC was also 850 Torr with continuous gas flow.

The laser beam out of either ARHCF or MPC was directed into the FTS. The scheme for the FTS used in this experiment is presented in Section 3.4.3. The same as in the multispecies detection experiment, first, the reference spectra were obtained. In this case, the fiber and cell were filled with N_2, and then sample measurements were performed with gas cells filled with target gas. The 100 spectra were acquired in both cases with the spectral resolution of 500 MHz, then submitted to the FFTs and averaged. The procedure was the same as in Section 5.3.1, the sample gas spectrum was normalized to the reference one, and then the baseline was removed using the cepstral method [215]. The Lambert-Beer law was used to compute the absorption coefficients. For the fit models, the only fitting parameter was the concentration. For methane and ethane, the absorption lines parameters from the HITRAN database [222] and the Voigt profile were used, and for butane and pentane, the absorption cross-sections from the Pacific Northwest National Laboratory (PNNL) database [223]. Once again, prof. Aleksandra Foltynowicz supported the fitting of the models and cepstral analysis and also provided expert opinions.

5.4.1. Comparison of ARHCF and MPC

To compare the performance of the ARHCF and MPC as gas absorption cells, both of them were filled with N_2, as it is a neutral gas in this spectral range and does not have any absorption lines in this mid-IR region. Reference spectra were acquired and can be observed in Fig. 5.17 normalized to their peak intensity. In the lowest panel of the figure, there is a difference between the two spectra presented. The excellent compatibility of the spectra proves that the beam was correctly collimated into the fiber. Otherwise, the improper coupling of the light into the ARHCF or bending of the fiber may result in the excitation of higher modes and changes in the spectrum of the transmitted light [224,225]. The visible absorption lines that can be observed in both spectra are from the water vapor in the laboratory air, as the FTS is not vacuumed. Another noticeable component in the residuals comes from etalon effects in both absorption cells.

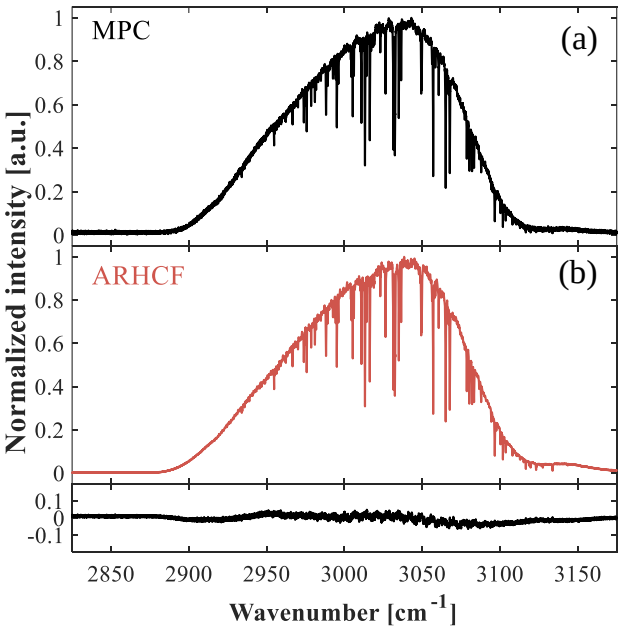

Fig. 5.17. Comparison of transmission spectra of the OFC for the absorption cells filled with N_2: (a) antiresonant hollow-core fiber (ARHCF) and (b) multipass cell (MPC), together with the residuals, measured by the FTS.

Another parameter worth comparing is the gas sample volume needed to fill the absorption cells. For the ARHCF, the gas is only located in the fiber's core, so the volume is equal to ~0.77 mL, while for the MPC, it is 0.85 L, with a similar interaction length. The difference in the volume value is higher than three orders of magnitude. This enables the conduct of research with gas samples of limited availability. The use of ARHCF could be a solution for measuring gases that are hazardous or difficult to obtain or for conducting research on human breath samples. So far, a method that supported such measurements is PAS [2]. Techniques using CW lasers are fast and sensitive but limited to a narrow bandwidth limited by the laser tunability [226,227]. For broadband detection, OFCs with mechanical FTS could be implemented to carry out cantilever-enhanced PAS [228,229]. However, the downside of this approach is the relatively long measuring time, which is in the order of a few minutes. By using the phase-controlled FTS, one can achieve 10 times faster acquisition times but at the cost of reduced performance [230]. Another approach is based on dual-comb systems, but it has only been implemented in the near-IR range [231–233] so far.

The second parameter worth noting is the transmission loss. The power from the same OFC source after the ARHCF was equal to 2.85 mW, and for MPC, it was 1.47 mW. It corresponds to 8 dB and 10.8 dB of transmission losses, respectively. In the case of low-power laser sources used for the spectroscopy, the value of power after the MPC could be insufficient to measure in the FTS or another method of obtaining the spectrum. Moreover, in the case of longer interaction length, it would be crucial to minimize the losses. Additionally, the output power influences the sensitivity of the setup, as it impacts the noise floor level (Eq. (3.9)).

5.4.2. Measurements of individual molecular species

For the performance evaluation of the ARHCF, an experiment for broadband laser spectroscopy was conducted. Spectra for various gases were recorded in the mid-IR region for ARHCF and MPC. It is important to note that there have not been any reports of using the ARHCF with OFC in the mid-IR range for spectroscopy purposes before. Four different hydrocarbons were chosen, as they are molecules critical for environmental monitoring. Two of them had narrow absorption lines at atmospheric pressure: methane (CH_4) and ethane (C_2H_6), while two had broadband, continuous absorption spectra: butane (C_4H_{10}) and pentane (C_5H_{12}). Such a selection emphasizes the advantages of this approach, having an absorption cell with wide transmission windows and a laser source with the broadband spectrum and simultaneously acquiring them with an FTS, allowing for simultaneous measurement of crucial parameters of the gas samples.

Measured gases came from certified cylinders, and the concentration of specific molecules was as follows: 2.08 ppmv of CH_4 (3% uncertainty), 1.07 ppmv of C_2H_6 (10% uncertainty), 9.64 ppmv of C_4H_{10} (5% uncertainty) and 10.26 ppmv of C_5H_{12} (3% uncertainty). In Fig. 5.18, there are measured spectra (in black) presented of methane (Fig. 5.18(a) and (b)), ethane (Fig. 5.18(c) and (d)), butane (Fig. 5.18(e) and (f)) and pentane (Fig. 5.18(g) and (h)). Each plot has a fitted spectrum (in red and plotted in negative for clarity) using the data from databases (HITRAN or PNNL) and the value of fitted concentrations. At the bottom panel of every figure, residuals are plotted. Furthermore, the division of Fig. 5.18 into two columns helps distinguish the measurements performed for the ARHCF (left column – Fig. 5.18(a), (c), (e), and (g)) from the ones taken for MPC (right column – Fig. 5.18(b), (d), (f), and (h)).

Results of spectroscopic measurements presented in Fig. 5.18 portray the capability of the ARHCF for being used as an absorption cell in the same way as the MPC. Additionally, it is essential to note that measurements of continuous absorption lines, like in the case of butane and pentane, can be influenced by improper baseline fitting if the laser source does not extend beyond the gas absorption profile. In this example, it did not happen, as it was possible to acquire all data at once, and the structure of the absorption spectrum did not influence the extracted concentrations.

To demonstrate the resolution of the proposed method, Fig. 5.19 presents zooms of the CH_4 absorption spectrum registered using the ARHCF-based gas absorption cell (from Fig. 5.18(a)). Actual data points are plotted as open circles and are separated by 500 MHz. The nominal resolution of the used FTS could be further improved with the length of the delay line, even up to 75 MHz. If the nominal resolution were matched with the comb mode spacing of 125 MHz, the measurements could be performed with the sub-nominal resolution, where one is limited by the linewidth of individual teeth of a stabilized comb [141]. It would allow us to measure low-pressure spectra with high precision.

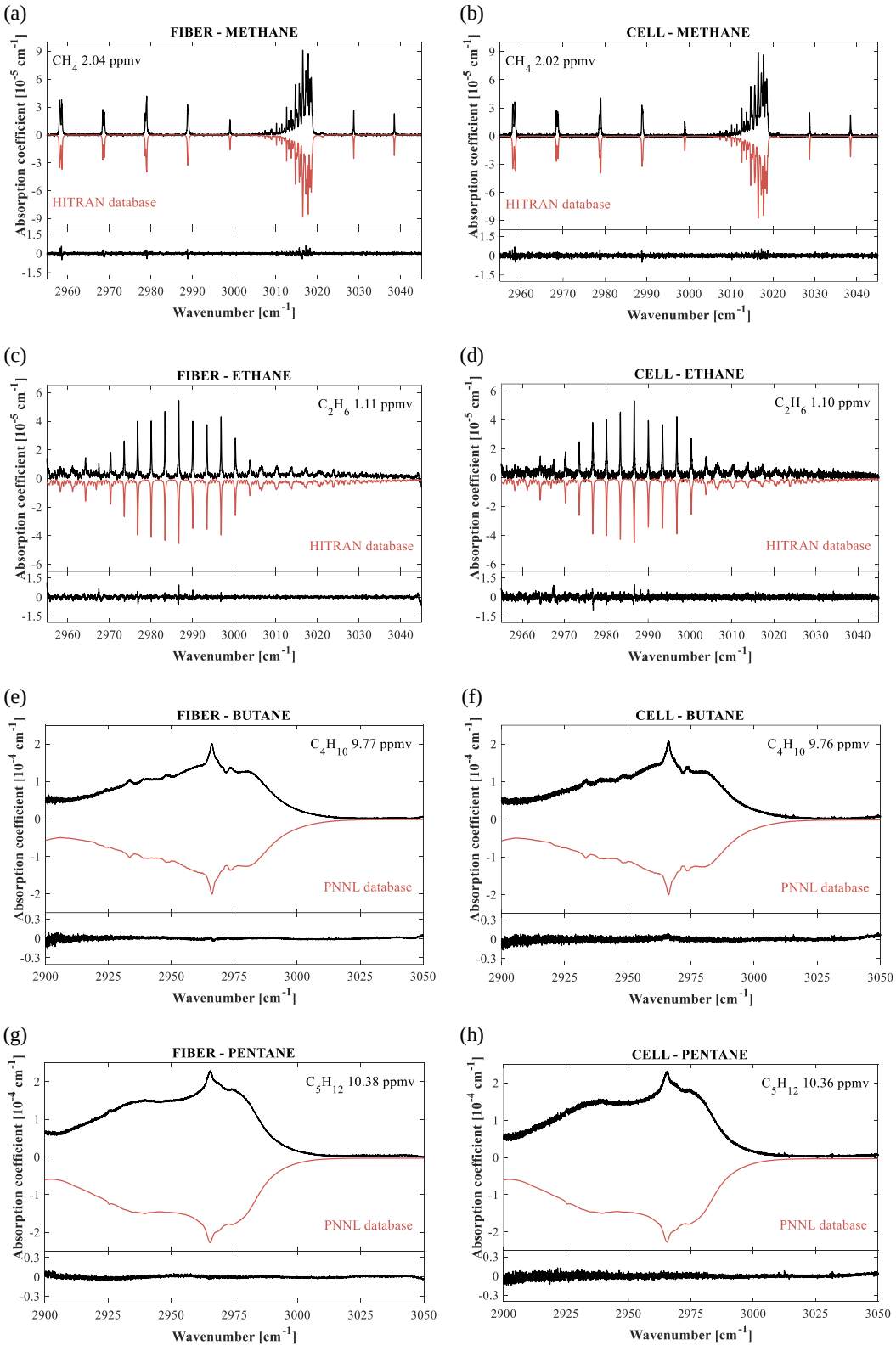

Fig. 5.18. Absorption spectra measured using a DFG-based OFC and FTS (black) at 850 Torr in the ARHCF and MPC, compared to fits based on HITRAN or PNNL database (red, plotted in negative for clarity). The residuals of the fits are shown in the lower panels of every figure. The gas type and concentration are designated in the panels: (a) and (b) 2.08 ppmv of methane (CH_4); (c) and (d) 1.07 ppmv of ethane (C_2H_6); (e) and (f) 9.64 ppmv of butane (C_4H_{10}); (g) and (h) 10.26 ppmv of pentane (C_5H_{12}). A column consisting of (a), (c), (e), and (g) shows spectra obtained when the gas sample was in the ARHCF, and a second column with (b), (d), (f), and (h) shows spectra retrieved with the gas sample in the MPC.

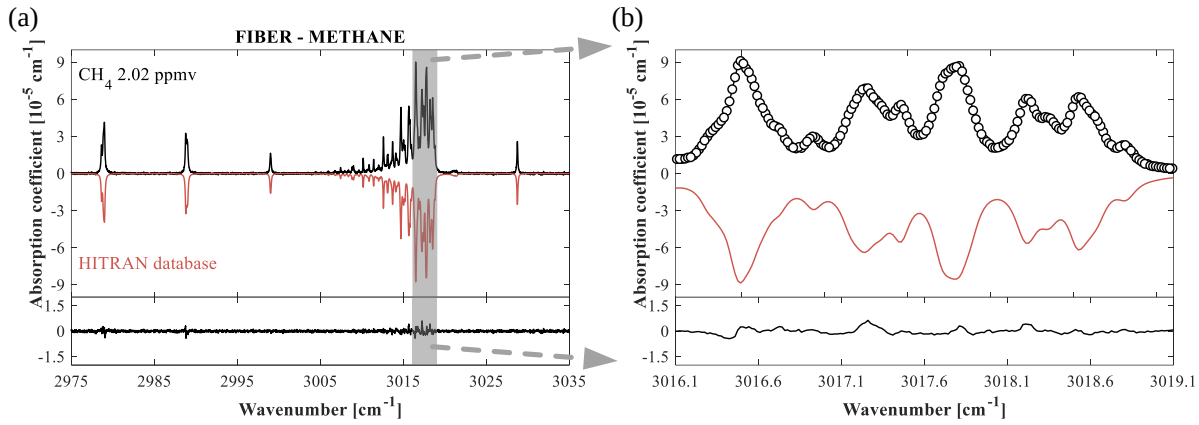

Fig. 5.19. (a) A zoom of the CH_4 spectrum measured in the ARHCF together with the residuum. (b) A further magnified view of one of the line features; open circles in black are measured single data points; fitted HITRAN-based spectrum is shown in red and plotted in negative for clarity.

The NEA coefficient was also calculated for these spectroscopic setups, where the acquisition time was equal to 167 s. Two background spectra were averaged 100 times and divided by each other. The standard deviation of this ratio was 1.2×10^{-3} for the ARHCF and 4.1×10^{-3} for the MPC in the central range of spectra covering 90 cm^{-1}, and the number of spectral elements was 5400. From this data, the NEA coefficient was calculated, which amounted to 8.3×10^{-8} cm^{-1} $Hz^{-1/2}$ per spectral element for ARHCF and 2.3×10^{-7} cm^{-1} $Hz^{-1/2}$ per spectral element for MPC. Comparing those values to the NEA coefficient achieved during the multispecies detection described in the previous Section, it can be noticed that using the same light source and spectrometer but increasing the interaction length from 10 cm to 30 meters improved the sensitivity by almost two orders of magnitude. Nevertheless, the obtained values of the NEA are at a similar level to previously published results for the experiments employing comb-based systems, MPCs, and FTS in the mid-IR region [98,142]. When the results were compared to the comb-based PAS methods, NEA values were 100 times better than those in the previously published work [228,229].

5.5. Conclusions

This Chapter demonstrated the potential of OFCs as sources for laser absorption spectroscopy. Their wide spectrum allows them to measure all absorption bands of molecules, distinguish gases during simultaneous analysis, and measure narrow and wide absorption lines with high precision. Two experiments showed these advantages. For both of them, a DFG-based OFC was constructed mainly by the Author's supervisors, Grzegorz Soboń and Karol Krzempek. The built source had a similar spectral tunability but less average output power than similar setups [105,106,119]. However, it is distinctive from previous sources because of the active lock for the delay line, which has fully stabilized the pulse's output power and spectral envelope.

The first spectroscopic experiment included joint measurements of methane and ethane, both of which were recognizable, and their absorption lines were separated. During the experiment, the absorption coefficient of 615 ppmv of methane at a pressure of 200 Torr and 0.245% of methane at 760 Torr were measured and retrieved. The obtained results were

in agreement with the model. The received NEA coefficient amounted to 4.0×10^{-6} cm^{-1} $Hz^{-1/2}$ per spectral element, which is similar to the value obtained for a single-pass cell OFC Fourier transform spectroscopy [138].

In the second study, four different hydrocarbons were measured separately, two with narrow and two with broad absorption lines. The research was conducted in ARHCF and MPC, both of which were of similar lengths. Due to that, a comparison of their performance was prepared, proving that ARHCFs can be used as a reliable substitute for MPCs. Additionally, the small volume needed to fill the ARHCF makes it an eligible candidate for measuring gas samples of limited availability. The ARHCF was designed and manufactured by Fei Yu and his research group from the Shanghai Institute of Optics and Fine Mechanics. Part of the experiment connected with filling the fiber and cell with gas samples was performed by Piotr Jaworski, the Author's co-worker. Tab. 5.1 contains a comparison of parameters for both absorption cells: their length, volume of the gas sample, measured transmission losses, and the NEA coefficient per spectral element. These results highlight the better performance of the ARHCF than that of MPC.

Tab. 5.1. Comparison of ARHCF- and MPC-based absorption cells. The parameters point to better capabilities of ARHCF.

	ARHCF	**MPC**
Absorption cell length [m]	26.15	31.227
Gas sample volume [mL]	0.77	850
Transmission losses [dB]	8	11
NEA coefficient per spectral element [cm^{-1} Hz^{-1}]	8.3×10^{-8}	2.3×10^{-7}

The absorption coefficients were retrieved for four different hydrocarbons, whose concentrations are stated in Tab. 5.2. The slight difference in concentrations measured in ARHCF and MPC may have been caused by measurement errors of the optical path length of ARHCF and MPC, the pressure in gas cells, varying temperatures in the lab, different power levels, or instability of the laser source, especially its spectrum. Despite these discrepancies, both values are in the range of concentration given by the producer of the gas cylinders.

So far, ARHCFs have been successfully used for spectroscopy with narrow-linewidth CW sources, both in near-IR [165] and mid-IR [234]. In combination with OFC, they were reported only in near-IR [235]. However, none of the research published to date has reported using ARHCFs to detect spectrally broad gases, such as hydrocarbons like pentane or butane. The presented research was the first literature report on combining ARHCF with OFCs for spectroscopy in the mid-IR. Also, the work benefited from one of the most valuable advantages of ARHCFs: very broad and low-loss transmission bands, particularly within the mid-IR spectral range. The spectroscopic part of both experiments was conducted by the Author herself, under the supervision of prof. Aleksandra Foltynowicz from Umeå University, apart from the line fitting for the multispecies detection conducted by prof. Aleksandra Foltynowicz.

Tab. 5.2. The concentrations and uncertainties given by the producer and concentrations retrieved from the measurements in ARHCF and MPC.

Gases	Concentration from producer [ppmv]	Uncertainty from producer [ppmv]	Concentration measured in ARHCF [ppmv]	Concentration measured in MPC [ppmv]
CH_4	2.08	0.06	2.04	2.02
C_2H_6	1.07	0.10	1.11	1.10
C_4H_{10}	9.64	0.50	9.77	9.76
C_5H_{12}	10.26	0.30	10.38	10.36

The still-emerging applications of ARHCFs for spectroscopy offer many opportunities for future research work. One of the fields would be using an absorption cell based on ARHCF with OFC as a light source for measuring gases at low pressure. Complementary use of the sub-nominal method [141] would allow for high-precision measurement of low-pressure spectra, which could result in determining the accurate parameters of absorption lines with high accuracy. Another research direction worth considering is exploiting different transmission windows of ARHCF during one experiment with OFC sources. Either one tunable OFC source or two OFCs could be used to measure the same molecule in the ARHCF at two different broadband spectral regions, which cannot be performed with CW laser sources. The improvements in gas-filling methods will allow future miniaturization of spectroscopic systems using ARHCF-based absorption cells.

Chapter 6.

Conclusions

The subject of the dissertation was a study of optical frequency combs generated in the mid-infrared spectral region to use in laser spectroscopy. The first thesis was that a gain-managed nonlinear amplification regime allows the generating of short laser pulses with high power and a spectral bandwidth reaching beyond the gain profile of the active medium. The second thesis read the combination of antiresonant hollow-core fibers and optical frequency combs converted to mid-infrared by nonlinear effects, enables conducting absorption spectroscopy of broad and narrow absorption lines with parameters as good as those obtained with a multipass cell of similar length. The dissertation consists of 6 Chapters, among which two contain theoretical information and the other two present experimental work.

Chapter 2 provided a theory about optical frequency combs – the principle of their operation and different methods of obtaining them. The basics of laser mode-locking and stabilization of optical frequency comb were described following the amplification of laser pulses. The Author presented a new regime of amplification – a gain-managed nonlinear regime and its properties. Lastly, nonlinear methods of converting the optical frequency comb to mid-infrared were given among other laser sources in this spectral region.

In Chapter 3, the topic of absorption spectroscopy with optical frequency combs was discussed. It started with a theory behind molecular absorption and details about direct frequency comb spectroscopy. Descriptions of different gas cells like multipass cells, enhancement cavities, and antiresonant hollow-core fibers were presented, as well as their properties and applications. The Chapter ended with various spectrometer designs, especially the Fourier transform spectrometer, as it was used for experiments presented in this dissertation.

Chapter 4 described the experiment in which a gain-managed nonlinear amplification regime for an ytterbium-doped fiber laser was studied. Two different pump diode lasers were used, with wavelengths of 918 and 976 nm, and two different seed sources, with high (125 MHz) and low repetition rate (30 MHz). The study included numerical analysis, and the simulations were in good agreement with the experimental results. The shortest obtained pulse had a duration of 33 fs, which is, up to date, the shortest pulse duration reported for this type of amplification. Additionally, it was the first measurement of the relative intensity noise of a gain-managed nonlinear amplifier. The setup for amplification was then used to build the difference frequency generation source based on an ytterbium-doped fiber laser.

Chapter 5 presented examples of optical frequency comb spectroscopy in the mid-infrared range. Simultaneous measurement of methane and ethane proved that thanks to the broad

spectrum of frequency combs, it is possible to measure entire absorption bands of different molecules at the same time and distinguish them from each other. The second experiment demonstrated for the first time the ability to use antiresonant hollow-core fiber as absorption gas cells to detect the concentration of different hydrocarbons with broad and narrow absorption in the mid-infrared via an optical frequency comb Fourier transform spectroscopy. The results were compared to one obtained for the multipass cell, which demonstrated the better performance of the antiresonant hollow-core fiber.

All the thesis goals have been achieved. The results presented in Chapter 4 confirmed the first thesis that high-power, short laser pulses whose spectral range extends beyond the gain profile of the active medium can be generated in the gain-managed nonlinear amplifier. In addition, Chapter 5 proved the second thesis, which stated that absorption spectroscopy of broad and narrow absorption lines carried out by optical frequency comb converted by nonlinear effects to mid-infrared and antiresonant hollow-core fiber achieves as good parameters as the one obtained with a multipass cell of similar length.

The most important original technical achievements of the presented work include:

- The construction of gain-managed nonlinear amplifiers for the 1 μm spectral region, which enable obtaining high-power, ultrashort pulses.
- Development of optical frequency combs in the 3-5 μm mid-infrared region based on difference-frequency generation.
- The construction of setup for optical frequency comb spectroscopy, consisting of a Fourier transform spectrometer working in the 3.2-11.8 μm spectral range with a nominal resolution of 75 MHz.

The most important original scientific achievements of the presented work include:

- Investigating the gain-managed nonlinear amplification for high- and low-repetition-rate laser seed sources at 1 μm in terms of the optical spectrum, pulse duration, spectral and temporal phase analysis, relative intensity noise, and output powers.
- The study of soliton self-frequency shift in different highly nonlinear fibers: commercially available and in-house-made.
- Conducting research on multispecies detection of gases in the optical frequency comb Fourier transform spectroscopy.
- The world's first demonstration of using antiresonant-hollow-core-fiber-based absorption cell for optical frequency comb Fourier transform spectroscopy in the mid-infrared region.
- The comparative study of antiresonant hollow-core fiber and multipass cell as absorption cells for optical frequency comb Fourier transform spectroscopy.

Streszczenie

Dzięki swojemu szerokopasmowemu widmu, wysokiej rozdzielczości spektralnej i dokładnej częstotliwości, optyczne grzebienie częstotliwości (ang. *optical frequency* comb, OFC) otworzyły drogę do precyzyjnej spektroskopii całych pasm molekularnych w krótkim czasie akwizycji, a także jednoczesnego monitorowania wielu rodzajów gazów za pomocą jednego źródła światła. Stabilne źródła OFC w średniej podczerwieni, gdzie linie absorpcyjne cząsteczek są silne, można uzyskać poprzez nieliniową konwersję spektrum, taką jak generacja częstotliwości różnicowej (ang. *difference frequency generation*, DFG). W niniejszej rozprawie przedstawiono analizę generowania OFC w średniej podczerwieni oraz eksperymentalne przykłady wykorzystania ich do zastosowań w spektroskopii laserowej.

Pierwsza część rozprawy poświęcona jest teoretycznym badaniom OFC oraz podstawom laserowej spektroskopii absorpcyjnej. Obejmuje ona różne metody otrzymywania OFC, zwłaszcza w średniej podczerwieni, a także ich charakterystykę, stabilizację, wzmocnienie i konwersję. Szczególną uwagę zwrócono na nową metodę wzmacniania impulsów laserowych, nieliniowy reżim zarządzania wzmocnieniem (ang. *gain-managed nonlinear,* GMN). Może ona dostarczać impulsy o dużej mocy z szerokopasmowym widmem optycznym, wykraczającym poza konwencjonalny profil wzmocnienia ośrodka aktywnego i z możliwością ich kompresji do impulsów prawie ograniczonych fourierowsko. Następnie opisano spektroskopię OFC, wskazując na jej zalety. Omówiono różne techniki wzmacniania sygnału absorpcji, z naciskiem na antyrezonansowe światłowody z rdzeniem powietrznym (ang. *antiresonant hollow-core fiber*, ARHCF). Część teoretyczna rozprawy kończy się krótkim opisem metod detekcji oraz szczegółami dotyczącymi spektrometru Fourierowskiego (ang. *Fourier transform spectrometer*, FTS) wykorzystywanego do badań eksperymentalnych.

Dwa rozdziały rozprawy poświęcone są układom eksperymentalnym, które zostały zademonstrowane i omówione. Najpierw przedstawiono dogłębną analizę wzmacnienia GMN lasera światłowodowego domieszkowanego iterbem. Skonstruowano dwa różne wzmacniacze z innymi diodami laserowymi do pompowania (o długości fali 918 i 976 nm). Dodatkowo, dwa różne źródła laserowe o wysokiej (125 MHz) i niskiej częstotliwości repetycji (30 MHz) zostały użyte jako źródła do wzmacniacza. Uzyskane wyniki pokazały wpływ parametrów lasera źródłowego i diody pompującej na charakterystykę wzmacnianych impulsów. Porównanie opierało się na parametrach takich jak widma optyczne, funkcje autokorelacji, czas trwania impulsów, fazy widmowe i czasowe, właściwości szumowe i moc wyjściowa. Była to pierwsza prezentacja właściwości szumowych wzmacnienia w reżimie GMN. Symulacje numeryczne wzmacnienia GMN uzupełniły dane eksperymentalne. Co więcej, wzmocniony i skompresowany impuls o czasie trwania 33 fs i mocy szczytowej 2,29 W jest, jak dotąd, najkrótszym impulsem laserowym o najwyższej mocy szczytowej osiągniętej dla tego reżimu. Konfiguracja do wzmacnienia została również wykorzystana do skonstruowania OFC opartego na DFG, pracującego w zakresie spektralnym 3-5 μm.

Kolejna część rozprawy koncentrowała się na eksperymentalnym wykorzystaniu OFC do spektroskopii laserowej w średniej podczerwieni. Pierwszy eksperyment wykazał zdolność do wykrywania wielu gazów jednocześnie dzięki szerokiemu spektrum OFC. Zaprezentowano wyniki jednoczesnego pomiaru metanu i etanu. Drugie badanie było pierwszą demonstracją

zastosowania komórki absorpcyjnej na bazie światłowodu ARHCF w połączeniu z OFC w średniej podczerwieni. W tym eksperymencie zmierzono stężenia czterech różnych węglowodorów z szerokimi i wąskimi liniami absorpcyjnymi za pomocą spektrometru FTS. Przeprowadzono porównanie wyników dla ARHCF i komórki wieloprzejściowej, wykazując lepszą charakterystykę dla ARHCF.

W niniejszej rozprawie zademonstrowano potencjał spektroskopii z wykorzystaniem OFC. Otrzymane wyniki zostały porównano z najlepszymi osiągnięciami w tej dziedzinie i zidentyfikowano dalsze perspektywy rozwoju badań. Wyniki pracy zostały opublikowane w trzech artykułach w czasopismach z listy JCR oraz zaprezentowane na czternastu krajowych i międzynarodowych konferencjach naukowych.

Abstract

Thanks to their broadband spectrum, high spectral resolution, and frequency accuracy, optical frequency combs (OFCs) have opened the way for precise spectroscopy of entire molecular bands in short acquisition time, as well as simultaneous monitoring of multiple gas species with a single light source. Stable OFC sources in the mid-infrared, where the absorption lines of molecules are strong, can be obtained by nonlinear conversion, such as difference frequency generation (DFG). The dissertation presents an analysis of generating OFCs in mid-infrared and experimental examples of using them for laser spectroscopy purposes.

The first part of the dissertation is devoted to the theoretical study of OFCs and the basics of laser absorption spectroscopy. It consists of various methods of obtaining OFC, especially in the mid-infrared, as well as their characteristics, stabilization, amplification, and conversion. Particular attention was paid to the new amplification method of laser pulses, gain-managed nonlinear (GMN) regime. It can deliver high-power pulses with an optically broadband spectrum beyond the conventional gain profile of the active medium and with the possibility of compressing them to nearly transform-limited pulses. Next, OFC spectroscopy was described, pointing out its advantages. Different techniques for enhancing the absorption signal were covered, with an emphasis on using antiresonant hollow-core fibers (ARHCFs). The theoretical part of the thesis ends with a short description of detection methods and details on the Fourier transform spectrometer (FTS) used for experimental studies.

Two Chapters of the dissertation are dedicated to experimental setups, which have been demonstrated and discussed. First, an in-depth analysis of GMN amplification of ytterbium-doped fiber laser is presented. Two different amplifiers were constructed with various laser pump diodes (918 and 976 nm wavelengths). Additionally, two different laser sources with high (125 MHz) and low repetition rate (30 MHz) were used for seeding the amplifier. The obtained results showed the influence of seed laser and pump diode parameters on the characteristics of amplified pulses. The comparison was based on parameters like optical spectra, autocorrelation functions, pulse durations, spectral and temporal phases, noise properties, and output powers. It was the first presentation of the GMN amplification noise properties. Numerical simulations of the GMN amplification complemented the experimental data. Furthermore, the amplified and compressed pulse with a duration of 33 fs and peak power of 2.29 W is, up to date, the shortest laser pulse with the highest peak power achieved for this regime. The setup for amplification was also used for constructing the DFG-based OFC working in the 3-5 μm spectral range.

The next part of the dissertation concentrated on the experimental usage of OFC for laser spectroscopy in the mid-infrared. The first experiment demonstrated the ability to detect multispecies thanks to the broad spectrum of the OFC. The results of simultaneous measurement of methane and ethane were presented. The second study was the first demonstration of using ARHCF-based absorption cell with OFC in the mid-infrared. In this experiment, concentrations of the four different hydrocarbons with broad and narrow absorption lines were measured by the FTS. A comparison of the results for ARHCF and a multipass cell was conducted, demonstrating better performance of the ARHCF.

The dissertation demonstrated the capabilities of OFC spectroscopy. The achieved results were compared with the best achievements in this field, and further development perspectives were identified. The results of this work were published in three articles in JCR-listed journals and presented at fourteen national and international scientific conferences.

References

1. G. B. Rieker, J. B. Jeffries, and R. K. Hanson, "Calibration-free wavelength-modulation spectroscopy for measurements of gas temperature and concentration in harsh environments," Appl. Opt., AO **48**, 5546–5560 (2009).
2. A. A. Kosterev, Y. A. Bakhirkin, R. F. Curl, and F. K. Tittel, "Quartz-enhanced photoacoustic spectroscopy," Opt. Lett., OL **27**, 1902–1904 (2002).
3. A. Foltynowicz, J. Wang, P. Ehlers, and O. Axner, "Distributed-feedback-laser-based NICE-OHMS in the pressure-broadened regime," Opt. Express, OE **18**, 18580–18591 (2010).
4. D. J. Jones, S. A. Diddams, J. K. Ranka, A. Stentz, R. S. Windeler, J. L. Hall, and S. T. Cundiff, "Carrier-Envelope Phase Control of Femtosecond Mode-Locked Lasers and Direct Optical Frequency Synthesis," Science **288**, 635–639 (2000).
5. S. T. Cundiff and J. Ye, "Colloquium: Femtosecond optical frequency combs," Rev. Mod. Phys. **75**, 325–342 (2003).
6. A. Schliesser, N. Picqué, and T. W. Hänsch, "Mid-infrared frequency combs," Nat. Photonics **6**, 440–449 (2012).
7. D. Strickland and G. Mourou, "Compression of amplified chirped optical pulses," Optics Communications **56**, 219–221 (1985).
8. D. F. Hotz, "Gain Narrowing in a Laser Amplifier," Appl. Opt., AO **4**, 527–530 (1965).
9. P. Sidorenko, W. Fu, and F. Wise, "Nonlinear ultrafast fiber amplifiers beyond the gain-narrowing limit," Optica **6**, 1328–1333 (2019).
10. P. Sidorenko, M. Buttolph, M. Mejooli, C.-Y. Eom, C. B. Schaffer, and F. Wise, "Evaluation of a gain-managed nonlinear fiber amplifier for multiphoton microscopy," Biomed. Opt. Express, BOE **14**, 2324–2332 (2023).
11. F. Yu, W. J. Wadsworth, and J. C. Knight, "Low loss silica hollow core fibers for 3–4 μm spectral region," Opt. Express, OE **20**, 11153–11158 (2012).
12. B. H. Soffer, "Giant Pulse Laser Operation by a Passive, Reversibly Bleachable Absorber," Journal of Applied Physics **35**, 2551 (1964).
13. G. Bret and F. Gires, "Giant-pulse laser and light amplifier using variable transmission coefficient glasses as light switches," Applied Physics Letters **4**, 175–176 (2004).
14. H. R. Telle, G. Steinmeyer, A. E. Dunlop, J. Stenger, D. H. Sutter, and U. Keller, "Carrier-envelope offset phase control: A novel concept for absolute optical frequency measurement and ultrashort pulse generation," Appl Phys B **69**, 327–332 (1999).
15. A. Apolonski, A. Poppe, G. Tempea, Ch. Spielmann, Th. Udem, R. Holzwarth, T. W. Hänsch, and F. Krausz, "Controlling the Phase Evolution of Few-Cycle Light Pulses," Phys. Rev. Lett. **85**, 740–743 (2000).
16. S. A. Diddams, Th. Udem, J. C. Bergquist, E. A. Curtis, R. E. Drullinger, L. Hollberg, W. M. Itano, W. D. Lee, C. W. Oates, K. R. Vogel, and D. J. Wineland, "An Optical Clock Based on a Single Trapped $^{199}Hg^{+}$ Ion," Science **293**, 825–828 (2001).
17. J. Ye, L. S. Ma, and J. L. Hall, "Molecular Iodine Clock," Phys. Rev. Lett. **87**, 270801 (2001).
18. J. Stenger, H. Schnatz, C. Tamm, and H. R. Telle, "Ultraprecise Measurement of Optical Frequency Ratios," Phys. Rev. Lett. **88**, 073601 (2002).
19. K. W. Holman, D. J. Jones, D. D. Hudson, and J. Ye, "Precise frequency transfer through a fiber network by use of 1.5-μm mode-locked sources," Optics Letters **29**, 1554–1556 (2004).
20. S. M. Foreman, K. W. Holman, D. D. Hudson, D. J. Jones, and J. Ye, "Remote transfer of ultrastable frequency references via fiber networks," Review of Scientific Instruments **78**, 021101 (2007).
21. R. Holzwarth, Th. Udem, T. W. Hänsch, J. C. Knight, W. J. Wadsworth, and P. St. J. Russell, "Optical Frequency Synthesizer for Precision Spectroscopy," Phys. Rev. Lett. **85**, 2264–2267 (2000).
22. S. T. Cundiff and A. M. Weiner, "Optical arbitrary waveform generation," Nature Photon **4**, 760–766 (2010).
23. M. Hentschel, R. Kienberger, C. Spielmann, G. A. Reider, N. Milosevic, T. Brabec, P. Corkum, U. Heinzmann, M. Drescher, and F. Krausz, "Attosecond metrology," Nature **414**, 509–513 (2001).

24. T. Steinmetz, T. Wilken, C. Araujo-Hauck, R. Holzwarth, T. W. Hänsch, L. Pasquini, A. Manescau, S. D'Odorico, M. T. Murphy, T. Kentischer, W. Schmidt, and T. Udem, "Laser Frequency Combs for Astronomical Observations," Science **321**, 1335–1337 (2008).
25. J. L. Hall, "Nobel Lecture: Defining and measuring optical frequencies," Rev. Mod. Phys. **78**, 1279–1295 (2006).
26. T. W. Hänsch, "Nobel Lecture: Passion for precision," Rev. Mod. Phys. **78**, 1297–1309 (2006).
27. K. A. Tillman, R. R. J. Maier, D. T. Reid, and E. D. McNaghten, "Mid-infrared absorption spectroscopy of methane using a broadband femtosecond optical parametric oscillator based on aperiodically poled lithium niobate," J. Opt. A: Pure Appl. Opt. **7**, S408 (2005).
28. A. Gambetta, R. Ramponi, and M. Marangoni, "Mid-infrared optical combs from a compact amplified Er-doped fiber oscillator," Opt. Lett., OL **33**, 2671–2673 (2008).
29. A. E. Siegman, *Lasers* (University Science Books, 1986).
30. A. Takada and H. Miyazawa, "30 GHz picosecond pulse generation from actively mode-locked erbium-doped fibre laser," Electronics Letters **26**, 216–217 (1990).
31. M. V. Gorbunkov, Y. Maslova, Y. V. Shabalin, and V. G. Tunkin, "Analysis of Self-Starting Harmonic Mode-Locking in an Electro-Optic-Feedback Laser," IEEE Journal of Quantum Electronics **57**, 1–8 (2021).
32. E. Yoshida and M. Nakazawa, "80~200 GHz erbium doped fibre laser using a rational harmonic mode-locking technique," Electronics Letters **32**, 1370–1372 (1996).
33. G. Zhu and N. K. Dutta, "Eighth-order rational harmonic mode-locked fiber laser with amplitude-equalized output operating at 80 Gbits/s," Opt. Lett., OL **30**, 2212–2214 (2005).
34. G. Soboń, J. Sotor, I. Pasternak, A. Krajewska, W. Strupinski, and K. M. Abramski, "Multilayer graphene-based saturable absorbers with scalable modulation depth for mode-locked Er- and Tm-doped fiber lasers," Opt. Mater. Express, OME **5**, 2884–2894 (2015).
35. X. Peng and Y. Yan, "Graphene saturable absorbers applications in fiber lasers," Journal of the European Optical Society-Rapid Publications **17**, 16 (2021).
36. G. Soboń, A. Dużyńska, M. Świniarski, J. Judek, J. Sotor, and M. Zdrojek, "CNT-based saturable absorbers with scalable modulation depth for Thulium-doped fiber lasers operating at 1.9 μm," Sci Rep **7**, 45491 (2017).
37. F. Ji, L. Xu, and H. Ming, "Passively mode-locked fiber laser using SESAM," in *Optoelectronic Devices and Integration II* (SPIE, 2008), Vol. 6838, pp. 30–34.
38. H. Ahmad, N. Hidayah Mansor, S. Aisyah Reduan, M. Zharif Samion, M. Umar Mustaqim Ithnahaini, and N. Yusoff, "High power passively mode-locked laser with Sb2Te3 deposited tapered fiber in Er/Yb doped fiber laser," Optical Fiber Technology **73**, 103013 (2022).
39. H. Haris, M. Batumalay, T. S. Jin, A. R. Muhammad, A. M. Markom, M. H. Izani, M. M. I. M. Hasnan, and I. Saad, "All-Fiber High-Energy Mode-Locked Ytterbium-Doped Fiber Laser with Bismuth Telluride Nanosheet Saturable Absorber," Crystals **12**, 1507 (2022).
40. L. C. Sinclair, I. Coddington, W. C. Swann, G. B. Rieker, A. Hati, K. Iwakuni, and N. R. Newbury, "Operation of an optically coherent frequency comb outside the metrology lab," Opt. Express, OE **22**, 6996–7006 (2014).
41. K. Iwakuni, H. Inaba, Y. Nakajima, T. Kobayashi, K. Hosaka, A. Onae, and F.-L. Hong, "Narrow linewidth comb realized with a mode-locked fiber laser using an intra-cavity waveguide electro-optic modulator for high-speed control," Opt. Express, OE **20**, 13769–13776 (2012).
42. J. Rauschenberger, T. M. Fortier, D. J. Jones, J. Ye, and S. T. Cundiff, "Control of the frequency comb from a mode-locked Erbium-doped fiber laser," Opt. Express, OE **10**, 1404–1410 (2002).
43. T. M. Fortier, A. Bartels, and S. A. Diddams, "Octave-spanning Ti:sapphire laser with a repetition rate >1 GHz for optical frequency measurements and comparisons," Opt. Lett., OL **31**, 1011–1013 (2006).
44. S. Schilt and T. Südmeyer, "Carrier-Envelope Offset Stabilized Ultrafast Diode-Pumped Solid-State Lasers," Applied Sciences **5**, 787–816 (2015).
45. W. Xia and X. Chen, "Recent developments in fiber-based optical frequency comb and its applications," Meas. Sci. Technol. **27**, 041001 (2016).
46. M. L. Weichman, P. B. Changala, J. Ye, Z. Chen, M. Yan, and N. Picqué, "Broadband molecular spectroscopy with optical frequency combs," Journal of Molecular Spectroscopy **355**, 66–78 (2019).

47. C. Gohle, T. Udem, M. Herrmann, J. Rauschenberger, R. Holzwarth, H. A. Schuessler, F. Krausz, and T. W. Hänsch, "A frequency comb in the extreme ultraviolet," Nature **436**, 234–237 (2005).
48. M. C. Tatham, J. F. Ryan, and C. T. Foxon, "Time-resolved Raman measurements of intersubband relaxation in GaAs quantum wells," Phys. Rev. Lett. **63**, 1637–1640 (1989).
49. J. Faist, G. Villares, G. Scalari, M. Rösch, C. Bonzon, A. Hugi, and M. Beck, "Quantum Cascade Laser Frequency Combs," Nanophotonics **5**, 272–291 (2016).
50. A. Hugi, G. Villares, S. Blaser, H. C. Liu, and J. Faist, "Mid-infrared frequency comb based on a quantum cascade laser," Nature **492**, 229–233 (2012).
51. G. P. Agrawal, "Nonlinear fiber optics: its history and recent progress [Invited]," J. Opt. Soc. Am. B, JOSAB **28**, A1–A10 (2011).
52. J. C. Travers, M. H. Frosz, and J. M. Dudley, "Nonlinear fibre optics overview," in *Supercontinuum Generation in Optical Fibers*, J. M. Dudley and J. R. Taylor, eds. (Cambridge University Press, 2010), pp. 32–51.
53. M. Sinobad, A. DellaTorre, R. Armand, B. Luther-Davies, P. Ma, S. Madden, A. Mitchell, D. J. Moss, J.-M. Hartmann, J.-M. Fedeli, C. Monat, and C. Grillet, "Mid-infrared supercontinuum generation in silicon-germanium all-normal dispersion waveguides," Opt. Lett., OL **45**, 5008–5011 (2020).
54. A. R. Johnson, A. S. Mayer, A. Klenner, K. Luke, E. S. Lamb, M. R. E. Lamont, C. Joshi, Y. Okawachi, F. W. Wise, M. Lipson, U. Keller, and A. L. Gaeta, "Octave-spanning coherent supercontinuum generation in a silicon nitride waveguide," Opt. Lett., OL **40**, 5117–5120 (2015).
55. T. Herr, V. Brasch, J. D. Jost, C. Y. Wang, N. M. Kondratiev, M. L. Gorodetsky, and T. J. Kippenberg, "Temporal solitons in optical microresonators," Nature Photon **8**, 145–152 (2014).
56. L. A. Lugiato and R. Lefever, "Spatial Dissipative Structures in Passive Optical Systems," Phys. Rev. Lett. **58**, 2209–2211 (1987).
57. T. J. Kippenberg, A. L. Gaeta, M. Lipson, and M. L. Gorodetsky, "Dissipative Kerr solitons in optical microresonators," Science **361**, eaan8083 (2018).
58. V. Torres-Company and A. M. Weiner, "Optical frequency comb technology for ultra-broadband radio-frequency photonics," Laser & Photonics Reviews **8**, 368–393 (2014).
59. D. R. Carlson, D. D. Hickstein, W. Zhang, A. J. Metcalf, F. Quinlan, S. A. Diddams, and S. B. Papp, "Ultrafast electro-optic light with subcycle control," Science **361**, 1358–1363 (2018).
60. J. Limpert, F. Roser, T. Schreiber, and A. Tunnermann, "High-power ultrafast fiber laser systems," IEEE Journal of Selected Topics in Quantum Electronics **12**, 233–244 (2006).
61. L. Kuznetsova, F. W. Wise, S. Kane, and J. Squier, "Chirped-pulse amplification near the gain-narrowing limit of Yb-doped fiber using a reflection grism compressor," Appl. Phys. B **88**, 515–518 (2007).
62. W. Zhao, X. Hu, and Y. Wang, "Femtosecond-Pulse Fiber Based Amplification Techniques and Their Applications," IEEE Journal of Selected Topics in Quantum Electronics **20**, 512–524 (2014).
63. Y. Zaouter, D. N. Papadopoulos, M. Hanna, J. Boullet, L. Huang, C. Aguergaray, F. Druon, E. Mottay, P. Georges, and E. Cormier, "Stretcher-free high energy nonlinear amplification of femtosecond pulses in rod-type fibers," Opt. Lett., OL **33**, 107–109 (2008).
64. H.-W. Chen, J. Lim, S.-W. Huang, D. N. Schimpf, F. X. Kärtner, and G. Chang, "Optimization of femtosecond Yb-doped fiber amplifiers for high-quality pulse compression," Opt. Express, OE **20**, 28672–28682 (2012).
65. W. Liu, D. N. Schimpf, T. Eidam, J. Limpert, A. Tünnermann, F. X. Kärtner, and G. Chang, "Pre-chirp managed nonlinear amplification in fibers delivering 100 W, 60 fs pulses," Opt. Lett., OL **40**, 151–154 (2015).
66. H. Song, B. Liu, Y. Li, Y. Song, H. He, L. Chai, M. Hu, and C. Wang, "Practical 24-fs, 1-μJ, 1-MHz Yb-fiber laser amplification system," Opt. Express, OE **25**, 7559–7566 (2017).
67. M. E. Fermann, V. I. Kruglov, B. C. Thomsen, J. M. Dudley, and J. D. Harvey, "Self-Similar Propagation and Amplification of Parabolic Pulses in Optical Fibers," Phys. Rev. Lett. **84**, 6010–6013 (2000).
68. V. I. Kruglov, A. C. Peacock, J. M. Dudley, and J. D. Harvey, "Self-similar propagation of high-power parabolic pulses in optical fiber amplifiers," Opt. Lett., OL **25**, 1753–1755 (2000).
69. Y. Deng, C.-Y. Chien, B. G. Fidric, and J. D. Kafka, "Generation of sub-50 fs pulses from a high-power Yb-doped fiber amplifier," Opt. Lett., OL **34**, 3469–3471 (2009).

70. D. B. Soh, J. Nilsson, and A. B. Grudinin, "Efficient femtosecond pulse generation using a parabolic amplifier combined with a pulse compressor. II. Finite gain-bandwidth effect," J. Opt. Soc. Am. B, JOSAB **23**, 10–19 (2006).
71. D. Tomaszewska-Rolla, R. Lindberg, V. Pasiskevicius, F. Laurell, and G. Soboń, "A comparative study of an Yb-doped fiber gain-managed nonlinear amplifier seeded by femtosecond fiber lasers," Sci Rep **12**, 404 (2022).
72. P. Sidorenko and F. Wise, "Generation of 1 μJ and 40 fs pulses from a large mode area gain-managed nonlinear amplifier," Opt. Lett. **45**, 4084–4087 (2020).
73. W. Ye, C. Li, C. Zheng, N. P. Sanchez, A. K. Gluszek, A. J. Hudzikowski, L. Dong, R. J. Griffin, and F. K. Tittel, "Mid-infrared dual-gas sensor for simultaneous detection of methane and ethane using a single continuous-wave interband cascade laser," Opt. Express, OE **24**, 16973–16985 (2016).
74. Y. Yu, N. P. Sanchez, R. J. Griffin, and F. K. Tittel, "CW EC-QCL-based sensor for simultaneous detection of H_2O, HDO, N_2O and CH_4 using multi-pass absorption spectroscopy," Opt. Express, OE **24**, 10391–10401 (2016).
75. G. Villares, A. Hugi, S. Blaser, and J. Faist, "Dual-comb spectroscopy based on quantum-cascade-laser frequency combs," Nat Commun **5**, 5192 (2014).
76. L. A. Sterczewski, J. Westberg, and G. Wysocki, "Computational coherent averaging for free-running dual-comb spectroscopy," Opt. Express, OE **27**, 23875–23893 (2019).
77. L. A. Sterczewski, M. Bagheri, C. Frez, C. L. Canedy, I. Vurgaftman, M. Kim, C. S. Kim, C. D. Merritt, W. W. Bewley, and J. R. Meyer, "Interband cascade laser frequency combs," J. Phys. Photonics **3**, 042003 (2021).
78. J. Hult, R. S. Watt, and C. F. Kaminski, "High bandwidth absorption spectroscopy with a dispersed supercontinuum source," Opt. Express, OE **15**, 11385–11395 (2007).
79. K. E. Jahromi, Q. Pan, L. Høgstedt, S. M. M. Friis, A. Khodabakhsh, P. M. Moselund, and F. J. M. Harren, "Mid-infrared supercontinuum-based upconversion detection for trace gas sensing," Opt. Express, OE **27**, 24469–24480 (2019).
80. M. Yu, Y. Okawachi, A. G. Griffith, M. Lipson, and A. L. Gaeta, "Mode-locked mid-infrared frequency combs in a silicon microresonator," Optica, OPTICA **3**, 854–860 (2016).
81. "Mid-IR Lasers: Power and pulse capability ramp up for mid-IR lasers," https://www.laserfocusworld.com/lasers-sources/article/16550254/mid-ir-lasers-power-and-pulse-capability-ramp-up-for-mid-ir-lasers.
82. N. Picqué and T. W. Hänsch, "Frequency comb spectroscopy," Nature Photonics **13**, 146–157 (2019).
83. Z. Wang, B. Zhang, J. Liu, Y. Song, and H. Zhang, "Recent developments in mid-infrared fiber lasers: Status and challenges," Optics & Laser Technology **132**, 106497 (2020).
84. T. Ren, C. Wu, Y. Yu, T. Dai, F. Chen, and Q. Pan, "Development Progress of 3–5 μm Mid-Infrared Lasers: OPO, Solid-State and Fiber Laser," Applied Sciences **11**, 11451 (2021).
85. L. Chang, S. Liu, and J. E. Bowers, "Integrated optical frequency comb technologies," Nat. Photon. **16**, 95–108 (2022).
86. Y. Ohishi, "Supercontinuum generation and IR image transportation using soft glass optical fibers: a review [Invited]," Opt. Mater. Express, OME **12**, 3990–4046 (2022).
87. Y. Sun, J. Wu, M. Tan, X. Xu, Y. Li, R. Morandotti, A. Mitchell, and D. J. Moss, "Applications of optical microcombs," Adv. Opt. Photon., AOP **15**, 86–175 (2023).
88. V. Petrov, F. Rotermund, and F. Noack, "Generation of high-power femtosecond light pulses at 1 kHz in the mid-infrared spectral range between 3 and 12 μm by second-order nonlinear processes in optical crystals," J. Opt. A: Pure Appl. Opt. **3**, R1 (2001).
89. C. R. Phillips, J. Jiang, C. Mohr, A. C. Lin, C. Langrock, M. Snure, D. Bliss, M. Zhu, I. Hartl, J. S. Harris, M. E. Fermann, and M. M. Fejer, "Widely tunable midinfrared difference frequency generation in orientation-patterned GaAs pumped with a femtosecond Tm-fiber system," Opt. Lett., OL **37**, 2928–2930 (2012).
90. M. Beutler, I. Rimke, E. Büttner, P. Farinello, A. Agnesi, V. Badikov, D. Badikov, and V. Petrov, "Difference-frequency generation of ultrashort pulses in the mid-IR using Yb-fiber pump systems and $AgGaSe_2$," Opt. Express, OE **23**, 2730–2736 (2015).

91. K. Krzempek, G. Soboń, J. Sotor, and K. M. Abramski, "Fully-integrated dual-wavelength all-fiber source for mode-locked square-shaped mid-IR pulse generation via DFG in PPLN," Opt. Express, OE **23**, 32080–32086 (2015).
92. C. Gaida, M. Gebhardt, T. Heuermann, F. Stutzki, C. Jauregui, J. Antonio-Lopez, A. Schülzgen, R. Amezcua-Correa, A. Tünnermann, I. Pupeza, and J. Limpert, "Watt-scale super-octave mid-infrared intrapulse difference frequency generation," Light Sci Appl **7**, 94 (2018).
93. L. Jin, V. Sonnenschein, M. Yamanaka, H. Tomita, T. Iguchi, A. Sato, K. Nozawa, K. Yoshida, S. Ninomiya, and N. Nishizawa, "3.1–5.2 μm Coherent MIR Frequency Comb Based on Yb-Doped Fiber Laser," IEEE Journal of Selected Topics in Quantum Electronics **24**, 1–7 (2018).
94. R. W. Boyd, *Nonlinear Optics* (Elsevier, 2008).
95. N. Leindecker, A. Marandi, R. L. Byer, and K. L. Vodopyanov, "Broadband degenerate OPO for mid-infrared frequency comb generation," Opt. Express, OE **19**, 6296–6302 (2011).
96. N. Leindecker, A. Marandi, R. L. Byer, K. L. Vodopyanov, J. Jiang, I. Hartl, M. Fermann, and P. G. Schunemann, "Octave-spanning ultrafast OPO with 2.6-6.1μm instantaneous bandwidth pumped by femtosecond Tm-fiber laser," Opt. Express, OE **20**, 7046–7053 (2012).
97. F. Adler, K. C. Cossel, M. J. Thorpe, I. Hartl, M. E. Fermann, and J. Ye, "Phase-stabilized, 1.5 W frequency comb at 2.8–4.8 μm," Opt. Lett., OL **34**, 1330–1332 (2009).
98. A. Khodabakhsh, V. Ramaiah-Badarla, L. Rutkowski, A. C. Johansson, K. F. Lee, J. Jiang, C. Mohr, M. E. Fermann, and A. Foltynowicz, "Fourier transform and Vernier spectroscopy using an optical frequency comb at 3–5.4 μm," Opt. Lett., OL **41**, 2541–2544 (2016).
99. P. Maddaloni, P. Malara, G. Gagliardi, and P. D. Natale, "Mid-infrared fibre-based optical comb," New J. Phys. **8**, 262–262 (2006).
100. H. Timmers, A. Kowligy, A. Lind, F. C. Cruz, N. Nader, M. Silfies, G. Ycas, T. K. Allison, P. G. Schunemann, S. B. Papp, and S. A. Diddams, "Molecular fingerprinting with bright, broadband infrared frequency combs," Optica, OPTICA **5**, 727–732 (2018).
101. N. S. Han, J. Kim, T. H. Yoon, and M. Cho, "Broadband Infrared Spectroscopy of Molecules in Solutions with Two Intrapulse Difference-Frequency-Generated Mid-Infrared Frequency Combs," J Phys Chem B **125**, 307–316 (2021).
102. S. Vasilyev, A. Muraviev, D. Konnov, M. Mirov, V. Smolski, I. Moskalev, S. Mirov, and K. Vodopyanov, "Longwave infrared (6.6–11.4 μm) dual-comb spectroscopy with 240,000 comb-mode-resolved data points at video rate," Opt. Lett., OL **48**, 2273–2276 (2023).
103. J. H. Lee, J. van Howe, C. Xu, and X. Liu, "Soliton Self-Frequency Shift: Experimental Demonstrations and Applications," IEEE Journal of Selected Topics in Quantum Electronics **14**, 713–723 (2008).
104. I. Cristiani, R. Tediosi, L. Tartara, and V. Degiorgio, "Dispersive wave generation by solitons in microstructured optical fibers," Opt. Express, OE **12**, 124–135 (2004).
105. F. Zhu, H. Hundertmark, A. A. Kolomenskii, J. Strohaber, R. Holzwarth, and H. A. Schuessler, "High-power mid-infrared frequency comb source based on a femtosecond Er:fiber oscillator," Opt. Lett., OL **38**, 2360–2362 (2013).
106. S. A. Meek, A. Poisson, G. Guelachvili, T. W. Hänsch, and N. Picqué, "Fourier transform spectroscopy around 3 μm with a broad difference frequency comb," Appl. Phys. B **114**, 573–578 (2014).
107. G. Krauss, D. Fehrenbacher, D. Brida, C. Riek, A. Sell, R. Huber, and A. Leitenstorfer, "All-passive phase locking of a compact Er:fiber laser system," Opt. Lett., OL **36**, 540–542 (2011).
108. C. Erny, K. Moutzouris, J. Biegert, D. Kühlke, F. Adler, A. Leitenstorfer, and U. Keller, "Mid-infrared difference-frequency generation of ultrashort pulses tunable between 3.2 and 4.8 μm from a compact fiber source," Opt. Lett., OL **32**, 1138–1140 (2007).
109. V. S. de Oliveira, A. Ruehl, P. Masłowski, and I. Hartl, "Intensity noise optimization of a mid-infrared frequency comb difference-frequency generation source," Opt. Lett., OL **45**, 1914–1917 (2020).
110. V. Petrov, "Progress in 1-μm Pumped Mid-IR Optical Parametric Oscillators Based on Non-Oxide Nonlinear Crystals," IEEE Journal of Selected Topics in Quantum Electronics **21**, 193–206 (2015).
111. A. Gambetta, N. Coluccelli, M. Cassinerio, D. Gatti, P. Laporta, G. Galzerano, and M. Marangoni, "Milliwatt-level frequency combs in the 8-14 μm range via difference frequency generation from an Er:fiber oscillator," Opt. Lett., OL **38**, 1155–1157 (2013).

112. D. Sánchez, M. Hemmer, M. Baudisch, K. Zawilski, P. Schunemann, H. Hoogland, R. Holzwarth, and J. Biegert, "Broadband mid-IR frequency comb with $CdSiP_2$ and $AgGaS_2$ from an Er,Tm:Ho fiber laser," Opt. Lett., OL **39**, 6883–6886 (2014).
113. J. Sotor, T. Martynkien, P. G. Schunemann, P. Mergo, L. Rutkowski, and G. Soboń, "All-fiber mid-infrared source tunable from 6 to 9 μm based on difference frequency generation in OP-GaP crystal," Opt. Express, OE **26**, 11756–11763 (2018).
114. P. G. Schunemann, K. T. Zawilski, L. A. Pomeranz, D. J. Creeden, and P. A. Budni, "Advances in nonlinear optical crystals for mid-infrared coherent sources," J. Opt. Soc. Am. B, JOSAB **33**, D36–D43 (2016).
115. T. W. Neely, T. A. Johnson, and S. A. Diddams, "High-power broadband laser source tunable from 3.0 μm to 4.4 μm based on a femtosecond Yb:fiber oscillator," Opt. Lett., OL **36**, 4020–4022 (2011).
116. A. Ruehl, A. Gambetta, I. Hartl, M. E. Fermann, K. S. E. Eikema, and M. Marangoni, "Widely-tunable mid-infrared frequency comb source based on difference frequency generation," Opt. Lett., OL **37**, 2232–2234 (2012).
117. G. Soboń, T. Martynkien, P. Mergo, L. Rutkowski, and A. Foltynowicz, "High-power frequency comb source tunable from 2.7 to 4.2 μm based on difference frequency generation pumped by an Yb-doped fiber laser," Opt. Lett., OL **42**, 1748–1751 (2017).
118. K. Krzempek, D. Tomaszewska, A. Foltynowicz, and G. Soboń, "Fiber-based optical frequency comb at 3.3 μm for broadband spectroscopy of hydrocarbons [Invited]," Chin. Opt. Lett. **19**, 081406 (2021).
119. F. C. Cruz, D. L. Maser, T. Johnson, G. Ycas, A. Klose, F. R. Giorgetta, I. Coddington, and S. A. Diddams, "Mid-infrared optical frequency combs based on difference frequency generation for molecular spectroscopy," Opt. Express, OE **23**, 26814–26824 (2015).
120. D. L. Maser, G. Ycas, W. I. Depetri, F. C. Cruz, and S. A. Diddams, "Coherent frequency combs for spectroscopy across the 3–5 μm region," Appl. Phys. B **123**, 142 (2017).
121. D. Churin, K. Kieu, R. A. Norwood, and N. Peyghambarian, "Efficient Frequency Comb Generation in the 9-μm Region Using Compact Fiber Sources," IEEE Photonics Technology Letters **26**, 2271–2274 (2014).
122. K. F. Lee, C. J. Hensley, P. G. Schunemann, and M. E. Fermann, "Midinfrared frequency comb by difference frequency of erbium and thulium fiber lasers in orientation-patterned gallium phosphide," Opt. Express, OE **25**, 17411–17416 (2017).
123. K. Krzempek, D. Tomaszewska, A. Głuszek, T. Martynkien, P. Mergo, J. Sotor, A. Foltynowicz, and G. Soboń, "Stabilized all-fiber source for generation of tunable broadband f_{CEO}-free mid-IR frequency comb in the 7 – 9 μm range," Opt. Express, OE **27**, 37435–37445 (2019).
124. Y. Liu, J. Zhao, Z. Wei, F. X. Kärtner, and G. Chang, "High-power, high-repetition-rate tunable longwave mid-IR sources based on DFG in the OPA regime," Opt. Lett., OL **48**, 1052–1055 (2023).
125. W. Demtröder, *Laser Spectroscopy* (Springer, 1996).
126. M. Šimečková, D. Jacquemart, L. S. Rothman, R. R. Gamache, and A. Goldman, "Einstein *A*-coefficients and statistical weights for molecular absorption transitions in the *HITRAN* database," Journal of Quantitative Spectroscopy and Radiative Transfer **98**, 130–155 (2006).
127. D. J. Griffiths and D. F. Schroeter, *Introduction to Quantum Mechanics*, 3rd edition (Cambridge University Press, 2018).
128. A. Foltynowicz, W. Ma, F. M. Schmidt, and O. Axner, "Doppler-broadened noise-immune cavity-enhanced optical heterodyne molecular spectrometry signals from optically saturated transitions under low pressure conditions," J. Opt. Soc. Am. B, JOSAB **25**, 1156–1165 (2008).
129. J. Tennyson, P. F. Bernath, A. Campargue, A. G. Császár, L. Daumont, R. R. Gamache, J. T. Hodges, D. Lisak, O. V. Naumenko, L. S. Rothman, H. Tran, N. F. Zobov, J. Buldyreva, C. D. Boone, M. D. D. Vizia, L. Gianfrani, J.-M. Hartmann, R. McPheat, D. Weidmann, J. Murray, N. H. Ngo, and O. L. Polyansky, "Recommended isolated-line profile for representing high-resolution spectroscopic transitions (IUPAC Technical Report)," Pure and Applied Chemistry **86**, 1931–1943 (2014).
130. J. A. Silver, "Frequency-modulation spectroscopy for trace species detection: theory and comparison among experimental methods," Appl. Opt., AO **31**, 707–717 (1992).

131. M. Nikodem, D. Weidmann, and G. Wysocki, "Chirped laser dispersion spectroscopy with harmonic detection of molecular spectra," Appl. Phys. B **109**, 477–483 (2012).
132. L. Dong, C. Li, N. P. Sanchez, A. K. Gluszek, R. J. Griffin, and F. K. Tittel, "Compact CH_4 sensor system based on a continuous-wave, low power consumption, room temperature interband cascade laser," Applied Physics Letters **108**, 011106 (2016).
133. Y. Yu, N. P. Sanchez, F. Yi, C. Zheng, W. Ye, H. Wu, R. J. Griffin, and F. K. Tittel, "Dual quantum cascade laser-based sensor for simultaneous NO and NO_2 detection using a wavelength modulation-division multiplexing technique," Appl. Phys. B **123**, 164 (2017).
134. G. Wysocki, R. Lewicki, R. F. Curl, F. K. Tittel, L. Diehl, F. Capasso, M. Troccoli, G. Hofler, D. Bour, S. Corzine, R. Maulini, M. Giovannini, and J. Faist, "Widely tunable mode-hop free external cavity quantum cascade lasers for high resolution spectroscopy and chemical sensing," Appl. Phys. B **92**, 305–311 (2008).
135. A. Marian, M. C. Stowe, J. R. Lawall, D. Felinto, and J. Ye, "United time-frequency spectroscopy for dynamics and global structure," Science **306**, 2063–2068 (2004).
136. M. J. Thorpe, K. D. Moll, R. J. Jones, B. Safdi, and J. Ye, "Broadband cavity ringdown spectroscopy for sensitive and rapid molecular detection," Science **311**, 1595–1599 (2006).
137. S. A. Diddams, L. Hollberg, and V. Mbele, "Molecular fingerprinting with the resolved modes of a femtosecond laser frequency comb," Nature **445**, 627–630 (2007).
138. J. Mandon, G. Guelachvili, and N. Picqué, "Fourier transform spectroscopy with a laser frequency comb," Nature Photon **3**, 99–102 (2009).
139. F. Adler, M. J. Thorpe, K. C. Cossel, and J. Ye, "Cavity-Enhanced Direct Frequency Comb Spectroscopy: Technology and Applications," Annual Review of Analytical Chemistry **3**, 175–205 (2010).
140. B. Bernhardt, A. Ozawa, P. Jacquet, M. Jacquey, Y. Kobayashi, T. Udem, R. Holzwarth, G. Guelachvili, T. W. Hänsch, and N. Picqué, "Cavity-enhanced dual-comb spectroscopy," Nature Photon **4**, 55–57 (2010).
141. P. Maslowski, K. F. Lee, A. C. Johansson, A. Khodabakhsh, G. Kowzan, L. Rutkowski, A. A. Mills, C. Mohr, J. Jiang, M. E. Fermann, and A. Foltynowicz, "Surpassing the path-limited resolution of Fourier-transform spectrometry with frequency combs," Phys. Rev. A **93**, 021802 (2016).
142. F. Adler, P. Masłowski, A. Foltynowicz, K. C. Cossel, T. C. Briles, I. Hartl, and J. Ye, "Mid-infrared Fourier transform spectroscopy with a broadband frequency comb," Opt. Express, OE **18**, 21861–21872 (2010).
143. D. C. Benner, C. P. Rinsland, V. M. Devi, M. A. H. Smith, and D. Atkins, "A multispectrum nonlinear least squares fitting technique," Journal of Quantitative Spectroscopy and Radiative Transfer **53**, 705–721 (1995).
144. A. H. Pfund, "Atmospheric Contamination," Science **90**, 326–327 (1939).
145. J. U. White, "Long Optical Paths of Large Aperture," J. Opt. Soc. Am., JOSA **32**, 285–288 (1942).
146. D. R. Herriott and H. J. Schulte, "Folded optical delay lines," Applied Optics **4**, 883–889 (1965).
147. M. L. Thoma, R. Kaschow, and F. J. Hindelang, "A multiple-reflection cell suited for absorption measurements in shock tubes," Shock Waves **4**, 51–53 (1994).
148. G. Gagliardi and H.-P. Loock, eds., *Cavity-Enhanced Spectroscopy and Sensing*, 2014th edition (Springer, 2013).
149. L. Gianfrani, R. W. Fox, and L. Hollberg, "Cavity-enhanced absorption spectroscopy of molecular oxygen," J. Opt. Soc. Am. B, JOSAB **16**, 2247–2254 (1999).
150. D. Romanini, A. A. Kachanov, N. Sadeghi, and F. Stoeckel, "CW cavity ring down spectroscopy," Chemical Physics Letters **264**, 316–322 (1997).
151. I. Sadiek and G. Friedrichs, "Doppler-limited high-resolution spectrum and VPT2 assisted assignment of the C-H stretch of CH_2Br_2," Spectrochimica Acta Part A: Molecular and Biomolecular Spectroscopy **181**, 180–191 (2017).
152. P. W. Milonni and J. H. Eberly, *Laser Physics* (John Wiley & Sons, 2010).
153. R. F. Cregan, B. J. Mangan, J. C. Knight, T. A. Birks, P. S. Russell, P. J. Roberts, and D. C. Allan, "Single-Mode Photonic Band Gap Guidance of Light in Air," Science **285**, 1537–1539 (1999).
154. Y. Y. Wang, N. V. Wheeler, F. Couny, P. J. Roberts, and F. Benabid, "Low loss broadband transmission in hypocycloid-core Kagome hollow-core photonic crystal fiber," Opt. Lett., OL **36**, 669–671 (2011).

155. W. Belardi and J. C. Knight, "Hollow antiresonant fibers with low bending loss," Opt. Express, OE **22**, 10091–10096 (2014).
156. P. Jaworski, "A Review of Antiresonant Hollow-Core Fiber-Assisted Spectroscopy of Gases," Sensors **21**, 5640 (2021).
157. F. Benabid, "Hollow-core photonic bandgap fibre: new light guidance for new science and technology," Philosophical Transactions of the Royal Society A: Mathematical, Physical and Engineering Sciences **364**, 3439–3462 (2006).
158. P. Jaworski, P. Kozioł, K. Krzempek, D. Wu, F. Yu, P. Bojęś, G. Dudzik, M. Liao, K. Abramski, and J. Knight, "Antiresonant Hollow-Core Fiber-Based Dual Gas Sensor for Detection of Methane and Carbon Dioxide in the Near- and Mid-Infrared Regions," Sensors **20**, 3813 (2020).
159. W. Belardi and P. J. Sazio, "Borosilicate Based Hollow-Core Optical Fibers," Fibers **7**, 73 (2019).
160. A. Ventura, J. G. Hayashi, J. Cimek, G. Jasion, P. Janicek, F. B. Slimen, N. White, Q. Fu, L. Xu, H. Sakr, N. V. Wheeler, D. J. Richardson, and F. Poletti, "Extruded tellurite antiresonant hollow core fiber for Mid-IR operation," Opt. Express, OE **28**, 16542–16553 (2020).
161. N. M. Litchinitser, A. K. Abeeluck, C. Headley, and B. J. Eggleton, "Antiresonant reflecting photonic crystal optical waveguides," Opt. Lett., OL **27**, 1592–1594 (2002).
162. L. Vincetti and V. Setti, "Waveguiding mechanism in tube lattice fibers," Opt. Express, OE **18**, 23133–23146 (2010).
163. R. M. Carter, F. Yu, W. J. Wadsworth, J. D. Shephard, T. Birks, J. C. Knight, and D. P. Hand, "Measurement of resonant bend loss in anti-resonant hollow core optical fiber," Opt. Express, OE **25**, 20612–20621 (2017).
164. D. Tomaszewska-Rolla, P. Jaworski, D. Wu, F. Yu, A. Foltynowicz, K. Krzempek, and G. Soboń, "Mid-infrared optical frequency comb spectroscopy using an all-silica antiresonant hollow-core fiber," Opt. Express, OE **32**, 10679–10689 (2024).
165. M. Nikodem, G. Gomółka, M. Klimczak, D. Pysz, and R. Buczyński, "Laser absorption spectroscopy at 2 μm inside revolver-type anti-resonant hollow core fiber," Opt. Express, OE **27**, 14998–15006 (2019).
166. C. Yao, L. Xiao, S. Gao, Y. Wang, P. Wang, R. Kan, W. Jin, and W. Ren, "Sub-ppm CO detection in a sub-meter-long hollow-core negative curvature fiber using absorption spectroscopy at 2.3 μm," Sensors and Actuators B: Chemical **303**, 127238 (2020).
167. M. Nikodem, G. Gomółka, M. Klimczak, D. Pysz, and R. Buczyński, "Demonstration of mid-infrared gas sensing using an anti-resonant hollow core fiber and a quantum cascade laser," Opt. Express, OE **27**, 36350–36357 (2019).
168. C. Yao, M. Hu, A. Ventura, J. G. Hayashi, F. Poletti, and W. Ren, "Tellurite Hollow-Core Antiresonant Fiber-Coupled Quantum Cascade Laser Absorption Spectroscopy," Journal of Lightwave Technology **39**, 5662–5668 (2021).
169. C. Yao, S. Gao, Y. Wang, P. Wang, W. Jin, and W. Ren, "MIR-Pump NIR-Probe Fiber-Optic Photothermal Spectroscopy With Background-Free First Harmonic Detection," IEEE Sensors Journal **20**, 12709–12715 (2020).
170. K. Krzempek, P. Jaworski, P. Kozioł, and W. Belardi, "Antiresonant hollow core fiber-assisted photothermal spectroscopy of nitric oxide at 5.26 μm with parts-per-billion sensitivity," Sensors and Actuators B: Chemical **345**, 130374 (2021).
171. Y. Zhao, Y. Qi, H. L. Ho, S. Gao, Y. Wang, and W. Jin, "Photoacoustic Brillouin spectroscopy of gas-filled anti-resonant hollow-core optical fibers," Optica, OPTICA **8**, 532–538 (2021).
172. P. Jaworski, K. Krzempek, G. Dudzik, P. J. Sazio, and W. Belardi, "Nitrous oxide detection at 5.26 μm with a compound glass antiresonant hollow-core optical fiber," Opt. Lett., OL **45**, 1326–1329 (2020).
173. M. Hu, A. Ventura, J. Grigoleto Hayashi, F. Poletti, and W. Ren, "Mid-infrared absorption spectroscopy of ethylene at 10.5 μm using a chalcogenide hollow-core antiresonant fiber," Optics & Laser Technology **158**, 108932 (2023).
174. Ł. Kornaszewski, N. Gayraud, J. M. Stone, W. N. MacPherson, A. K. George, J. C. Knight, D. P. Hand, and D. T. Reid, "Mid-infrared methane detection in a photonic bandgap fiber using a broadband optical parametric oscillator," Opt. Express, OE **15**, 11219–11224 (2007).
175. A. Foltynowicz, T. Ban, P. Masłowski, F. Adler, and J. Ye, "Quantum-Noise-Limited Optical Frequency Comb Spectroscopy," Phys. Rev. Lett. **107**, 233002 (2011).

176. I. Coddington, W. C. Swann, and N. R. Newbury, "Coherent Multiheterodyne Spectroscopy Using Stabilized Optical Frequency Combs," Phys. Rev. Lett. **100**, 013902 (2008).
177. Z. Zhang, T. Gardiner, and D. T. Reid, "Mid-infrared dual-comb spectroscopy with an optical parametric oscillator," Opt. Lett., OL **38**, 3148–3150 (2013).
178. M. Shirasaki, "Large angular dispersion by a virtually imaged phased array and its application to a wavelength demultiplexer," Opt. Lett., OL **21**, 366–368 (1996).
179. L. Nugent-Glandorf, T. Neely, F. Adler, A. J. Fleisher, K. C. Cossel, B. Bjork, T. Dinneen, J. Ye, and S. A. Diddams, "Mid-infrared virtually imaged phased array spectrometer for rapid and broadband trace gas detection," Opt. Lett., OL **37**, 3285–3287 (2012).
180. A. J. Fleisher, B. J. Bjork, T. Q. Bui, K. C. Cossel, M. Okumura, and J. Ye, "Mid-Infrared Time-Resolved Frequency Comb Spectroscopy of Transient Free Radicals," J. Phys. Chem. Lett. **5**, 2241–2246 (2014).
181. C. Gohle, B. Stein, A. Schliesser, T. Udem, and T. W. Hänsch, "Frequency Comb Vernier Spectroscopy for Broadband, High-Resolution, High-Sensitivity Absorption and Dispersion Spectra," Phys. Rev. Lett. **99**, 263902 (2007).
182. L. Rutkowski and J. Morville, "Broadband cavity-enhanced molecular spectra from Vernier filtering of a complete frequency comb," Opt. Lett., OL **39**, 6664–6667 (2014).
183. A. Khodabakhsh, L. Rutkowski, J. Morville, and A. Foltynowicz, "Mid-infrared continuous-filtering Vernier spectroscopy using a doubly resonant optical parametric oscillator," Appl. Phys. B **123**, 210 (2017).
184. M. Siciliani de Cumis, R. Eramo, N. Coluccelli, M. Cassinerio, G. Galzerano, P. Laporta, P. De Natale, and P. Cancio Pastor, "Tracing part-per-billion line shifts with direct-frequency-comb Vernier spectroscopy," Phys. Rev. A **91**, 012505 (2015).
185. E. V. Loewenstein, "The History and Current Status of Fourier Transform Spectroscopy," Appl. Opt., AO **5**, 845–854 (1966).
186. P. R. Griffiths, "The Early Days of Commercial FT-IR Spectrometry: A Personal Perspective," Appl Spectrosc **71**, 329–340 (2017).
187. S. P. Davis, M. C. Abrams, and J. W. Brault, *Fourier Transform Spectrometry* (Academic Press, 2001).
188. P. R. Griffiths, J. A. D. Haseth, and J. D. Winefordner, *Fourier Transform Infrared Spectrometry*, 2nd edition (Wiley-Interscience, 2007).
189. E. Treacy, "Optical pulse compression with diffraction gratings," IEEE Journal of Quantum Electronics **5**, 454–458 (1969).
190. A. S. Mayer, W. Grosinger, J. Fellinger, G. Winkler, L. W. Perner, S. Droste, S. H. Salman, C. Li, C. M. Heyl, I. Hartl, and O. H. Heckl, "Flexible all-PM NALM Yb:fiber laser design for frequency comb applications: operation regimes and their noise properties," Opt. Express, OE **28**, 18946–18968 (2020).
191. B. Ortaç, M. Plötner, J. Limpert, and A. Tünnermann, "Self-starting passively mode-locked chirped-pulse fiber laser," Opt. Express, OE **15**, 16794–16799 (2007).
192. G. H. Jang, J. H. Kim, and T. H. Yoon, "Highly-stable Yb-doped fiber laser mode-locked in a regime of SESAM two-photon absorption," in *CLEO:2011 - Laser Applications to Photonic Applications (2011), Paper JWA24* (Optical Society of America, 2011), p. JWA24.
193. M. Weber, J. Lynch, D. Blackburn, and D. Cronin, "Dependence of the stimulated emission cross section of Yb^{3+} on host glass composition," IEEE J. Quantum Electron. **19**, 1600–1608 (1983).
194. H. Takebe, T. Murata, and K. Morinaga, "Compositional dependence of absorption and fluorescence of Yb^{3+} in oxide glasses," J. Am. Ceram. Soc **79**, 681–687 (1996).
195. R. Paschotta, J. Nilsson, A. C. Tropper, and D. C. Hanna, "Ytterbium-doped fiber amplifiers," IEEE Journal of Quantum Electronics **33**, 1049–1056 (1997).
196. R. Lindberg, P. Zeil, M. Malmström, F. Laurell, and V. Pasiskevicius, "Accurate modeling of high-repetition rate ultrashort pulse amplification in optical fibers," Sci. Rep. **6**, 34742 (2016).
197. J. Hult, "A Fourth-Order Runge–Kutta in the Interaction Picture Method for Simulating Supercontinuum Generation in Optical Fibers," Journal of Lightwave Technology **25**, 3770–3775 (2007).
198. A. M. Heidt, "Efficient Adaptive Step Size Method for the Simulation of Supercontinuum Generation in Optical Fibers," J. Lightwave Technol., JLT **27**, 3984–3991 (2009).

199. D. E. McCumber, "Einstein Relations Connecting Broadband Emission and Absorption Spectra," Phys. Rev. **136**, A954–A957 (1964).
200. B. Ren, C. Li, T. Wang, K. Guo, J. Wu, R. Su, P. Ma, and P. Zhou, "Generation of ultrafast laser with 11 MW peak power from a gain-managed nonlinear tapered fiber amplifier," Optics & Laser Technology **160**, 109081 (2023).
201. P. C. D. Hobbs, "Ultrasensitive laser measurements without tears," Appl. Opt., AO **36**, 903–920 (1997).
202. J. Ye, L.-S. Ma, and J. L. Hall, "Ultrasensitive detections in atomic and molecular physics: demonstration in molecular overtone spectroscopy," J. Opt. Soc. Am. B, JOSAB **15**, 6–15 (1998).
203. N. R. Newbury, I. Coddington, and W. Swann, "Sensitivity of coherent dual-comb spectroscopy," Opt. Express, OE **18**, 7929–7945 (2010).
204. N. Coluccelli, M. Cassinerio, A. Gambetta, P. Laporta, and G. Galzerano, "High-power frequency comb in the range of 2–2.15 μm based on a holmium fiber amplifier seeded by wavelength-shifted Raman solitons from an erbium-fiber laser," Opt. Lett., OL **39**, 1661–1664 (2014).
205. A. S. Mayer, C. R. Phillips, C. Langrock, A. Klenner, A. R. Johnson, K. Luke, Y. Okawachi, M. Lipson, A. L. Gaeta, M. M. Fejer, and U. Keller, "Offset-Free Gigahertz Midinfrared Frequency Comb Based on Optical Parametric Amplification in a Periodically Poled Lithium Niobate Waveguide," Phys. Rev. Appl. **6**, 054009 (2016).
206. M. Huber, W. Schweinberger, F. Stutzki, J. Limpert, I. Pupeza, and O. Pronin, "Active intensity noise suppression for a broadband mid-infrared laser source," Opt. Express, OE **25**, 22499–22509 (2017).
207. C. Gaida, T. Heuermann, M. Gebhardt, E. Shestaev, T. P. Butler, D. Gerz, N. Lilienfein, P. Sulzer, M. Fischer, R. Holzwarth, A. Leitenstorfer, I. Pupeza, and J. Limpert, "High-power frequency comb at 2 μm wavelength emitted by a Tm-doped fiber laser system," Opt. Lett., OL **43**, 5178–5181 (2018).
208. O. Szewczyk, P. Pala, K. Tarnowski, J. Olszewski, F. S. Vieira, C. Lu, A. Foltynowicz, P. Mergo, J. Sotor, G. Soboń, and T. Martynkien, "Dual-Wavelength Pumped Highly Birefringent Microstructured Silica Fiber for Widely Tunable Soliton Self-Frequency Shift," J. Lightwave Technol., JLT **39**, 3260–3268 (2021).
209. S. A. Dekker, A. C. Judge, R. Pant, I. Gris-Sánchez, J. C. Knight, C. M. de Sterke, and B. J. Eggleton, "Highly-efficient, octave spanning soliton self-frequency shift using a specialized photonic crystal fiber with low OH loss," Opt. Express, OE **19**, 17766–17773 (2011).
210. G. Soboń, T. Martynkien, D. Tomaszewska, K. Tarnowski, P. Mergo, and J. Sotor, "All-in-fiber amplification and compression of coherent frequency-shifted solitons tunable in the 1800-2000 nm range," Photon. Res., PRJ **6**, 368–372 (2018).
211. K. Krzempek, G. Soboń, and K. M. Abramski, "DFG-based mid-IR generation using a compact dual-wavelength all-fiber amplifier for laser spectroscopy applications," Opt. Express, OE **21**, 20023–20031 (2013).
212. D. Stoliarov, E. Manuylovich, A. Koviarov, D. Galiakhmetova, and E. Rafailov, "Gain-managed nonlinear amplification of ultra-long mode-locked fiber laser," Opt. Express, OE **31**, 43427–43437 (2023).
213. Y. Xing, R. Chen, L. Zhang, Y. Chen, S. Zhang, X. Diao, Y. Liu, Y. Shi, Z. Wei, and G. Chang, "SLAM medical imaging enabled by a pre-chirp and gain jointly managed Yb-fiber laser," Biomed. Opt. Express, BOE **15**, 911–923 (2024).
214. D. M. B. Lesko, H. Timmers, S. Xing, A. Kowligy, A. J. Lind, and S. A. Diddams, "A six-octave optical frequency comb from a scalable few-cycle erbium fibre laser," Nat. Photonics **15**, 281–286 (2021).
215. R. K. Cole, A. S. Makowiecki, N. Hoghooghi, and G. B. Rieker, "Baseline-free Quantitative Absorption Spectroscopy Based on Cepstral Analysis," Opt. Express **27**, 37920–37939 (2019).
216. I. E. Gordon, L. S. Rothman, C. Hill, R. V. Kochanov, Y. Tan, P. F. Bernath, M. Birk, V. Boudon, A. Campargue, K. V. Chance, B. J. Drouin, J.-M. Flaud, R. R. Gamache, J. T. Hodges, D. Jacquemart, V. I. Perevalov, A. Perrin, K. P. Shine, M.-A. H. Smith, J. Tennyson, G. C. Toon, H. Tran, V. G. Tyuterev, A. Barbe, A. G. Császár, V. M. Devi, T. Furtenbacher, J. J. Harrison, J.-M. Hartmann, A. Jolly, T. J. Johnson, T. Karman, I. Kleiner, A. A. Kyuberis, J. Loos, O. M. Lyulin, S. T. Massie, S. N. Mikhailenko, N. Moazzen-Ahmadi, H. S. P. Müller, O. V. Naumenko, A. V.

Nikitin, O. L. Polyansky, M. Rey, M. Rotger, S. W. Sharpe, K. Sung, E. Starikova, S. A. Tashkun, J. V. Auwera, G. Wagner, J. Wilzewski, P. Wcisło, S. Yu, and E. J. Zak, "The HITRAN2016 molecular spectroscopic database," Journal of Quantitative Spectroscopy and Radiative Transfer **203**, 3–69 (2017).
217. A. Foltynowicz, P. Masłowski, T. Ban, F. Adler, K. C. Cossel, T. C. Briles, and J. Ye, "Optical frequency comb spectroscopy," Faraday Discuss. **150**, 23–31 (2011).
218. "Thorlabs, Inc. - Your Source for Fiber Optics, Laser Diodes, Optical Instrumentation and Polarization Measurement & Control," https://www.thorlabs.com.
219. P. Jaworski, K. Krzempek, P. Kozioł, D. Wu, F. Yu, P. Bojęś, G. Dudzik, M. Liao, J. Knight, and K. Abramski, "Sub parts-per-billion detection of ethane in a 30-meters long mid-IR Antiresonant Hollow-Core Fiber," Optics & Laser Technology **147**, 107638 (2022).
220. T. Wildi, T. Voumard, V. Brasch, G. Yilmaz, and T. Herr, "Photo-acoustic dual-frequency comb spectroscopy," Nat Commun **11**, 4164 (2020).
221. W. A. Challener, A. M. Kasten, F. Yu, G. Puc, and B. J. Mangan, "Dynamics of Trace Methane Diffusion/Flow Into Hollow Core Fiber Using Laser Absorption Spectroscopy," IEEE Sensors Journal **21**, 6287–6292 (2021).
222. I. E. Gordon, L. S. Rothman, R. J. Hargreaves, R. Hashemi, E. V. Karlovets, F. M. Skinner, E. K. Conway, C. Hill, R. V. Kochanov, Y. Tan, P. Wcisło, A. A. Finenko, K. Nelson, P. F. Bernath, M. Birk, V. Boudon, A. Campargue, K. V. Chance, A. Coustenis, B. J. Drouin, J. –M. Flaud, R. R. Gamache, J. T. Hodges, D. Jacquemart, E. J. Mlawer, A. V. Nikitin, V. I. Perevalov, M. Rotger, J. Tennyson, G. C. Toon, H. Tran, V. G. Tyuterev, E. M. Adkins, A. Baker, A. Barbe, E. Canè, A. G. Császár, A. Dudaryonok, O. Egorov, A. J. Fleisher, H. Fleurbaey, A. Foltynowicz, T. Furtenbacher, J. J. Harrison, J. –M. Hartmann, V. –M. Horneman, X. Huang, T. Karman, J. Karns, S. Kassi, I. Kleiner, V. Kofman, F. Kwabia–Tchana, N. N. Lavrentieva, T. J. Lee, D. A. Long, A. A. Lukashevskaya, O. M. Lyulin, V. Yu. Makhnev, W. Matt, S. T. Massie, M. Melosso, S. N. Mikhailenko, D. Mondelain, H. S. P. Müller, O. V. Naumenko, A. Perrin, O. L. Polyansky, E. Raddaoui, P. L. Raston, Z. D. Reed, M. Rey, C. Richard, R. Tóbiás, I. Sadiek, D. W. Schwenke, E. Starikova, K. Sung, F. Tamassia, S. A. Tashkun, J. Vander Auwera, I. A. Vasilenko, A. A. Vigasin, G. L. Villanueva, B. Vispoel, G. Wagner, A. Yachmenev, and S. N. Yurchenko, "The HITRAN2020 molecular spectroscopic database," Journal of Quantitative Spectroscopy and Radiative Transfer **277**, 107949 (2022).
223. S. W. Sharpe, T. J. Johnson, R. L. Sams, P. M. Chu, G. C. Rhoderick, and P. A. Johnson, "Gas-phase databases for quantitative infrared spectroscopy," Appl Spectrosc **58**, 1452–1461 (2004).
224. M. Michieletto, J. K. Lyngsø, C. Jakobsen, J. Lægsgaard, O. Bang, and T. T. Alkeskjold, "Hollow-core fibers for high power pulse delivery," Opt. Express, OE **24**, 7103–7119 (2016).
225. B. Siwicki, R. M. Carter, J. D. Shephard, F. Yu, J. C. Knight, and D. P. Hand, "Negative-Curvature Anti-Resonant Fiber Coupling Tolerances," Journal of Lightwave Technology **37**, 5548–5554 (2019).
226. V. Spagnolo, P. Patimisco, S. Borri, G. Scamarcio, B. E. Bernacki, and J. Kriesel, "Part-per-trillion level SF_6 detection using a quartz enhanced photoacoustic spectroscopy-based sensor with single-mode fiber-coupled quantum cascade laser excitation," Opt. Lett., OL **37**, 4461–4463 (2012).
227. J. Peltola, T. Hieta, and M. Vainio, "Parts-per-trillion-level detection of nitrogen dioxide by cantilever-enhanced photo-acoustic spectroscopy," Opt. Lett., OL **40**, 2933–2936 (2015).
228. I. Sadiek, T. Mikkonen, M. Vainio, J. Toivonen, and A. Foltynowicz, "Optical frequency comb photoacoustic spectroscopy," Phys. Chem. Chem. Phys. **20**, 27849–27855 (2018).
229. J. Karhu, T. Tomberg, F. S. Vieira, G. Genoud, V. Hänninen, M. Vainio, M. Metsälä, T. Hieta, S. Bell, and L. Halonen, "Broadband photoacoustic spectroscopy of $^{14}CH_4$ with a high-power mid-infrared optical frequency comb," Opt. Lett., OL **44**, 1142–1145 (2019).
230. S. Larnimaa, M. Roiz, and M. Vainio, "Photoacoustic phase-controlled Fourier-transform infrared spectroscopy," Opt. Continuum, OPTCON **2**, 564–578 (2023).
231. J. T. Friedlein, E. Baumann, K. A. Briggman, G. M. Colacion, F. R. Giorgetta, A. M. Goldfain, D. I. Herman, E. V. Hoenig, J. Hwang, N. R. Newbury, E. F. Perez, C. S. Yung, I. Coddington, and K. C. Cossel, "Dual-comb photoacoustic spectroscopy," Nat Commun **11**, 3152 (2020).
232. X. Ren, M. Yan, Z. Wen, H. Ma, R. Li, K. Huang, and H. Zeng, "Dual-comb quartz-enhanced photoacoustic spectroscopy," Photoacoustics **28**, 100403 (2022).

233. Z. Wang, Q. Nie, H. Sun, Q. Wang, S. Borri, P. De Natale, and W. Ren, "Cavity-enhanced photoacoustic dual-comb spectroscopy," Light Sci Appl **13**, 11 (2024).
234. M. Hu and W. Ren, "Wavelength-modulation dispersion spectroscopy of NO with heterodyne phase-sensitive detection," Opt. Lett., OL **47**, 2899–2902 (2022).
235. Q. Wang, Z. Wang, H. Zhang, S. Jiang, Y. Wang, W. Jin, and W. Ren, "Dual-comb photothermal spectroscopy," Nat Commun **13**, 2181 (2022).

List of achievements

Directly related to the dissertation

List of publications

1. D. Tomaszewska-Rolla, P. Jaworski, D. Wu, F. Yu, A. Foltynowicz, K. Krzempek, G. Soboń, "Mid-infrared optical frequency comb spectroscopy using an all-silica antiresonant hollow-core fiber," Opt. Express 32, 10679-10689 (2024).
2. D. Tomaszewska-Rolla, R. Lindberg, V. Pasiskevicius, F. Laurell, G. Soboń, "A comparative study of an Yb-doped fiber gain-managed nonlinear amplifier seeded by femtosecond fiber lasers," Sci Rep 12, 404 (2022).
3. K. Krzempek, D. Tomaszewska, A. Foltynowicz, G. Soboń, "Fiber-based optical frequency comb at 3.3 μm for broadband spectroscopy of hydrocarbons [Invited]," Chin. Opt. Lett. 19, 081406 (2021).

Conference papers

1. D. Tomaszewska-Rolla, P. Jaworski, D. Wu, F. Yu, A. Foltynowicz, G. Soboń, K. Krzempek, "Mid-IR Optical Frequency Comb Fourier Transform Spectroscopy Using an Antiresonant Hollow-Core Fiber," 2023 Conference on Lasers and Electro-Optics Europe & European Quantum Electronics Conference (CLEO/Europe-EQEC), pp. 1-1, (2023).
2. D. Tomaszewska, R. Lindberg, V. Pasiskevicius, F. Laurell, G. Soboń, "Amplification of a 1.03 μm optical frequency comb in the gain-managed nonlinear regime – measurements and simulations," 2021 Conference on Lasers and Electro-Optics Europe & European Quantum Electronics Conference (CLEO/Europe-EQEC), pp. 1-1 (2021).
3. D. Tomaszewska, G. Soboń, "Research on amplification of ultrashort laser pulses at 1.03 μm in gain-managed nonlinearity regime," 9th EPS-QEOD Europhoton Conference on Solid-State, Fibre and Waveguide Coherent Light Sources (EUROPHOTON 2020), EPJ Web Conf. vol. 243, 07002, s. 1-1 (2020).

Conference contributions

1. D. Tomaszewska-Rolla, P. Jaworski, D. Wu, F. Yu, A. Foltynowicz, K. Krzempek, G. Soboń, "Mid-IR optical frequency comb spectroscopy using an all-silica antiresonant hollow-core fiber," Closing conference for the National Laboratory of Photonics and Quantum Technologies (NLPQT) Project, Warsaw, Poland, 2023, poster.
2. D. Tomaszewska-Rolla, P. Jaworski, D. Wu, F. Yu, A. Foltynowicz, K. Krzempek, G. Soboń, "Detekcja węglowodorów w średniej podczerwieni przy użyciu optycznego grzebienia częstotliwości oraz światłowodu antyrezonansowego z rdzeniem powietrznym," Polska Konferencja Optyczna 2023, Toruń, Poland, 2023, talk.

3. D. Tomaszewska-Rolla, P. Jaworski, D. Wu, F. Yu, A. Foltynowicz, G. Soboń, K. Krzempek, "Mid-IR Optical Frequency Comb Fourier Transform Spectroscopy Using an Antiresonant Hollow-Core Fiber," CLEO/Europe-EQEC 2023, Munich, Germany, 2023, talk.
4. D. Tomaszewska-Rolla, P. Jaworski, K. Krzempek, G. Soboń, "Pomiary spektroskopowe gazów za pomocą optycznego grzebienia częstotliwości i światłowodu antyrezonansowego," XIII Sympozjum Techniki Laserowej 2022, Karpacz, Poland, 2023, talk.
5. D. Tomaszewska-Rolla, G. Soboń, "Mid-infrared optical frequency comb covering the 3.5-5 μm range for laser spectroscopy," OPTO2022, Warsaw, Poland, 2022, talk.
6. D. Tomaszewska-Rolla, G. Soboń, "Optical frequency comb covering the 3.5-5 μm range for Fourier transform spectroscopy," 5th International workshop on opportunities and challenges in mid-infrared laser-based gas sensing, Wrocław, Poland, 2022, poster.
7. D. Tomaszewska-Rolla, G. Soboń, "Optyczny grzebień częstotliwości w zakresie średniej podczerwieni do zastosowań w spektroskopii laserowej," Polska Konferencja Optyczna 2022, Płock, Poland, 2022, talk.
8. D. Tomaszewska-Rolla, G. Soboń, "Optical frequency comb in mid-infrared for laser spectroscopy application," New Developments in High Resolution Molecular Spectroscopy and Outreach to Modern Applications, Les Houches, France, 2022, poster.
9. D. Tomaszewska, R. Lindberg, V. Pasiskevicius, F. Laurell, G. Soboń, "Investigation of the influence of fiber laser repetition rate on the amplification in the gain-managed nonlinear regime," OPTO2021, Gdańsk, Poland (online), 2021, talk.
10. D. Tomaszewska, R. Lindberg, V. Pasiskevicius, F. Laurell, G. Soboń, "Amplification of a 1.03 μm optical frequency comb in the gain-managed nonlinear regime – measurements and simulations," CLEO/Europe EQEC 2021, Munich, Germany (online), 2021, talk.
11. D. Tomaszewska, G. Soboń, "Wzmacnianie ultrakrótkich impulsów laserowych o długości fali 1,03 μm w reżimie zarządzania wzmocnieniem," V Ogólnopolska Studencka Fizyczno-Optyczna Konferencja FOKA 2020, Wrocław, Poland (online), 2020, talk.
12. D. Tomaszewska, G. Soboń, "Research on amplification of ultrashort laser pulses at 1.03 μm in gain-managed nonlinearity regime," 9TH EPS-QEOD EUROPHOTON, Prague, Czech Republic (online), 2020, talk.
13. D. Tomaszewska, G. Soboń, "Amplification of ultrashort laser pulses at 1.03 μm in gain-managed nonlinearity regime," ELI Summer School 2020, Szeged, Hungary (online), 2020, poster.
14. D. Tomaszewska, G. Soboń, "Amplification of ultrashort laser pulses in gain-managed nonlinearity regime," OPTO2020, Gdańsk, Poland (online), 2020, talk.

Other achievements

List of publications

1. A. Hjältén, M. Germann, K. Krzempek, A. Hudzikowski, A. Głuszek, D. Tomaszewska, G. Soboń, A. Foltynowicz, "Optical frequency comb Fourier transform spectroscopy of $^{14}N_2{}^{16}O$ at 7.8 μm," Journal of Quantitative Spectroscopy and Radiative Transfer, Volume 271, 107734 (2021).
2. M. Pawliszewska, D. Tomaszewska, G. Soboń, A. Dużyńska, M. Zdrojek, J. Sotor, "Broadband Metallic Carbon Nanotube Saturable Absorber for Ultrashort Pulse Generation in the 1500-2100 nm Spectral Range," Applied Sciences 11, 3121 (2021).
3. K. Krzempek, D. Tomaszewska, A. Głuszek, T. Martynkien, P. Mergo, J. Sotor, A. Foltynowicz, G. Soboń, "Stabilized all-fiber source for generation of tunable broadband f_{CEO}-free mid-IR frequency comb in the 7 – 9 μm range," Opt. Express 27, 37435-37445 (2019).
4. G. Soboń, T. Martynkien, D. Tomaszewska, K. Tarnowski, P. Mergo, J. Sotor, "All-in-fiber amplification and compression of coherent frequency-shifted solitons tunable in the 1800-2000 nm range," Photon. Res. 6, 368-372 (2018).
5. D. Tomaszewska, P. Jaworski, M. Nikodem, "Frequency-multiplexed gas sensing using chirped laser molecular spectroscopy," Opto-Electronics Review 26, 103–107 (2018).
6. K. Krzempek, D. Tomaszewska, K. M. Abramski, "Dissipative soliton resonance mode-locked all-polarization-maintaining double clad Er:Yb fiber laser, " Opt. Express 25, 24853-24860 (2017).

Conference papers

1. K. Krzempek, D. Tomaszewska-Rolla, A. Głuszek, A. Hudzikowski, M. Krakowski, A. Hjältén, M. Germann, A. Foltynowicz, G. Soboń, "Compact fiber-based mid-infrared frequency comb sources," Optica High-brightness Sources and Light-driven Interactions Congress 2022, Technical Digest Series, Optica Publishing Group, paper MW6C.1 (2022).
2. A. Hjältén, M. Germann, C. Lu, F. Senna Vieira, A. Foltynowicz, I. Sadiek, M. Stuhr, K. Krzempek, A. Hudzikowski, A. Głuszek, D. Tomaszewska, G. Soboń, "High-resolution comb-based Fourier transform spectroscopy in the 3.3 μm and 7.8 μm range," 2021 International Symposium on Molecular Spectroscopy, TB05, (2021).
3. M. Germann, A. Hjältén, K. Krzempek, A. Hudzikowski, A. Głuszek, D. Tomaszewska, G. Soboń, A. Foltynowicz, "Frequency Comb Fourier Transform Spectroscopy at 8 μm Using a Compact Difference Frequency Generation Source," 2021 Conference on Lasers and Electro-Optics Europe & European Quantum Electronics Conference (CLEO/Europe-EQEC), pp. 1-1 (2021).
4. A. Hjältén, M. Germann, I. Sadiek, C. Lu, F. S. Vieira, K. Krzempek, A. Hudzikowski, A. Głuszek, D. Tomaszewska, M. Stuhr, G. Soboń, A. Foltynowicz, "Fourier Transform Spectroscopy Using Difference Frequency Generation Comb Sources at 3.3 μm and

7.8 μm," OSA Optical Sensors and Sensing Congress 2021 (AIS, FTS, HISE, SENSORS, ES), OSA Technical Digest, Optica Publishing Group, paper JTu4D.3 (2021).

5. A. Hjältén, M. Germann, K. Krzempek, A. Hudzikowski, A. Głuszek, D. Tomaszewska, G. Soboń, A. Foltynowicz, "Precision Measurements of $^{14}N_2{}^{16}O$ Using a Comb-Based Fourier Transform Spectrometer at 7.8 μm," Conference on Lasers and Electro-Optics, OSA Technical Digest, Optica Publishing Group, paper SM1C.4 (2021).
6. K. Krzempek, D. Tomaszewska, A. Głuszek, A. Hudzikowski, T. Martynkien, P. Mergo, J. Sotor, A. Foltynowicz, G. Soboń, "Mid-infrared frequency comb covering the 6.5 – 9 μm range with active output power stabilization," OSA High-brightness Sources and Light-driven Interactions Congress 2020 (EUVXRAY, HILAS, MICS), OSA Technical Digest, Optica Publishing Group, paper MW3C.3 (2020).
7. K. Krzempek, D. Tomaszewska, A. Gluszek, A. Hudzikowski, T. Martynkien, P. Mergo, J. Sotor, A. Foltynowicz, G. Soboń, "Compact 6.5 – 9 pm Frequency Comb Source for Fourier Transform Spectroscopy," Optical Sensors and Sensing Congress, OSA Technical Digest, Optica Publishing Group, paper EM1C.2 (2020).
8. K. Krzempek, A. Głuszek, D. Tomaszewska, T. Martynkien, P. Mergo, J. Sotor, G. Soboń, "All-Fiber Source for Generation of Tunable Broadband f_{CEO}-Free Mid-IR Pulses for Laser Spectroscopy Applications," 2019 Conference on Lasers and Electro-Optics Europe & European Quantum Electronics Conference (CLEO/Europe-EQEC), pp. 1-1 (2019).
9. D. Charczun, G. Kowzan, A. Nishiyama, M. Debus, P. Huke, D. Tomaszewska, G. Soboń, A. Cygan, D. Lisak, R. S. Trawiński, P. Masłowski, "Fourier-Transform Frequency Comb Cavity Mode Spectroscopy at Hz Level for Trace Gas Measurements," in Advanced Photonics 2018 (BGPP, IPR, NP, NOMA, Sensors, Networks, SPPCom, SOF), OSA Technical Digest, Optica Publishing Group, paper SeTu4E.7 (2018).
10. D. Charczun, G. Kowzan, A. Nishiyama, M. Debus, P. Huke, D. Tomaszewska, G. Soboń, A. Cygan, R. S. Trawiński, D. Lisak, P. Masłowski, "Fourier-Transform Complex Refractive Index Spectroscopy at Hz-level Precision with an Optical Frequency Comb," 2018 International Symposium on Molecular Spectroscopy, TG09 (2018).

Conference contributions

1. D. Tomaszewska, K. Krzempek, D. Stachowiak, A. Głuszek, Z. Łaszczych, G. Soboń, "Fiber-based mid-infrared frequency combs for laser spectroscopy and environmental monitoring," ELI Summer School 2019, Dolni Brezany, Czech Republic, 2019, poster.
2. D. Tomaszewska, O. Drożdżowska, G. Soboń, "Generation of femtosecond pulses in Thulium-doped laser source based on chirped pulse amplification," Siegman International Summer School on Lasers 2019, Rochester, USA, 2019, poster.
3. D. Tomaszewska, T. Martynkien, K. Tarnowski, P. Mergo, J. Sotor, G. Soboń, "Generation and amplification of coherent frequency-shifted solitons tunable in the 1800-2000 nm regime," OPTO2018, Gdańsk, Poland, 2018, talk.

4. D. Tomaszewska, G. Soboń, "Światłowodowy laser tulowy z przestrajalną dyspersją chromatyczną rezonatora," II Ogólnopolska Studencka Fizyczno-Optyczna Konferencja FOKA, Szklarska Poręba, Poland, 2018, talk.

Received scientific projects

- "Nonlinear conversion of optical frequency comb to the mid-infrared range for laser spectroscopy applications" financed by The Polish Ministry of Education and Science (MEiN).

Participation in scientific projects

- "Fiber-based mid-infrared frequency combs for laser spectroscopy and environmental monitoring" financed by the Foundation for Polish Science.
- "National Laboratory for Photonics and Quantum Technologies" financed by the European Regional Development Fund.

Scientific schools and training

- KL FAMO School on Time Metrology in Experiments, Toruń, Poland, 2022.
- New Developments in High Resolution Molecular Spectroscopy and Outreach to Modern Applications, Les Houches, France, 2022.
- ELI Summer School 2020, online, 2020.
- All-Stars Virtual Siegman School, online, 2020.
- ELI Summer School 2019, Dolni Brezany, Czech Republic, 2019.
- Siegman International Summer School on Lasers 2019, Rochester, USA, 2019.
- International Training School on Fiber lasers and Optical Fiber Technology, Prague, Czech Republic, 2016.

Research stays

- 18.09-16.10.2021, Umeå University, Department of Physics, Umeå, Sweden. Supervision: prof. Aleksandra Foltynowicz.
- 07.02-14.03.2020, Umeå University, Department of Physics, Umeå, Sweden. Supervision: prof. Aleksandra Foltynowicz.
- 21.08-17.09.2017, Nicolaus Copernicus University, Department of Atomic, Molecular and Optical Physics, Toruń, Poland. Supervision: dr hab. Piotr Masłowski, prof. UMK.
- 17.07-13.08.2017, Zespół Spektroskopii Laserowej, Łukasiewicz Research Network - PORT Polish Center for Technology Development, Wrocław, Poland. Supervision: dr hab. inż Michał Nikodem, prof. PWr.

Awards

- Scholarship START for young scientists from the Foundation for Polish Science (2023).
- Scholarship for achievements in the field of engineering and technical sciences under the Student Scholarship Programme (2023).
- Audience award for the best presentation at the OPTO2022 conference, for the presentation "Mid-infrared optical frequency comb covering the 3.5-5 μm range for laser spectroscopy" (2022).
- Scholarship from the Own Fund of the Wrocław University of Science and Technology (2022).
- Prize of the Dean of the Department of Electronics, Photonics, and Microsystems of the Wroclaw University of Science and Technology for scientific achievements (2021, 2022).
- Third place in the best presentation competition at the OPTO2021 conference for the presentation "Investigation of the influence of fiber laser repetition rate on the amplification in the gain-managed nonlinear regime" (2021).
- Prize of the Rector of the Wroclaw University of Science and Technology for scientific achievements (2020).
- Main prize in the PhD students category at the V Ogólnopolska Studencka Fizyczno-Optyczna Konferencji FOKA 2020 for the presentation " Wzmacnianie ultrakrótkich impulsów laserowych o długości 1,03 μm w reżimie zarządzania wzmocnieniem" (2020).
- Second place in the best presentation competition at the OPTO2020 conference for the presentation "Amplification of ultrashort laser pulses in gain-managed nonlinearity regime" (2020).